Insight into the Design of Aerosol Spray Systems for Cell Therapies for Retinal Diseases using Computational Modelling and Experimental Assessment

By

Miriam Nweze

A thesis submitted for the degree of

DOCTOR OF PHILOSOPHY

Department of Mechanical Engineering

University College London

Torrington Place,

London WC1E 7JE

August 2019

Declaration

I, Miriam Nweze, confirm that the work presented in this thesis is my own. Where information has been derived from other sources, I confirm that this has been indicated in the thesis.

Acknowledgements

“Trust in the Lord with all your heart and lean not on your own understanding.”

Proverbs 3:5

I started this journey with so much excitement, without knowing how each stage will turn out; I am grateful to God for how far He has brought me, sustained me and strengthened me. I am extremely grateful for all the people God has brought into my life to help me accomplish this great achievement. I started this chapter of my life with You and I finish it with You.

Firstly, standing ovation to my primary supervisor Professor Rebecca Shipley (Becky); an inspirational woman from whom I have learned so much, not only academically, but also on life skills such as time management, leadership, and being optimistic and confident about my work. Becky, you truly stood out in ways I cannot explain; your humility and simplicity have inspired me to keep going and to remain strong in everything that I do. I would also like to thank my supervisors Professors Tim Baker and Astrid Limb. Thank you for your immense support and guidance since my first day at UCL. You challenged my work for better and inspired me to constantly aim higher in every area of my life, my career aspirations and academic journey. Your support has not been in vain and I cannot thank you enough!

Secondly, I am also very grateful to everyone in the Müller Group for their technical help; everything I have learned about cell culturing, I have learned from you. You have welcomed me with open arms part into the team, making it a fun and productive environment. I would like to extend my gratitude also to the Tissue Modelling Group; this work would not have been possible without you.

Completing this PhD would not have been possible without the outstanding level of support and love from my parents, my sisters and my nephew; thank you all very much for believing I could do this and constantly taking pride in my achievements. Everything I do and every stage of my success is dedicated to you. My pastors Prophet Stanley and Pastor Patience Osebre-Osei, thanks for your continuous prayers and encouragement. Special thanks also to Prophet Dr. Evans Oppong. Finally, to all my friends and loved ones that continue to support my dreams and believe I can achieve I set in my mind to do. Especially Dr Chika Nweke, Dr Anjana Kothandaraman and Dr Joana Mendonca Da Sliva; we connected through this journey and built and long-lasting friendship; we took this journey together and we did it! Thank you for the great memories that I will cherish for the rest of my life and being there during tough times.

“Whether you think you can or can’t, you are right”.

Henry Ford

Abstract

Retinal degenerative diseases affect numerous people worldwide and in the UK; they lead to dysfunction of retinal cells and retinal dysfunction, in turn leading to vision loss and in some cases blindness. Existing treatments aim to alleviate current risk factors leading to retinal degeneration, such as increased high pressure. However, these procedures do not restore lost cell, vision nor retinal function, and therefore may still lead to blindness.

Developing cell-based therapies to replace lost cells provides one option for retinal tissue repair in order to restore retinal function. These therapies involve delivering stem cells to encourage neural cell-like functions within the retinal tissue. Despite progress in developing stem-cells compatible with the retinal layers, there is also a need to developing a minimal invasive technique for cell delivery, without damaging the neighbouring optical structure. After evaluating several methods of cell delivery, this thesis explores the need for developing aerosol spraying systems for stem-cell delivery into the human eye.

Mathematical modelling is used as a tool to define spraying parameters which, alongside experimental work, may accelerate the design of aerosol spraying systems to treat retinal degenerative disease such as glaucoma. Firstly, an organic biomaterial is developed and used as scaffold to spray and protect cells from aerodynamic forces and stresses associated with aerosolization. The rheological properties of this biomaterial are incorporated within a computational model to predict cell-spraying into a human eye. Boundary and initial conditions mimic the experimental spraying conditions, and the parameterised model is used to explore the link between operator-defined conditions (namely volume flow rate of the cell-laden hydrogel, external pressure needed for aerosolization and angle of the spraying) and spraying outputs (surface area of the retina covered, droplets speed, wall shear stress on the retinal surface).

Data from both computational and experimental analyses were gathered. Computational modelling is used to explore the impact of spraying parameters (pressure and volume flow rate at the injector nozzle, outer cone angle for the spray) on key outputs of high priority, namely the spatial distribution of the delivered hydrogel on the retinal wall, the surface area of the retina covered and droplet speed. Droplets speed at the retinal wall appeared to increase with increasing pressure conditions and were observed at a constant volume flow rate. Experimental assessments were used to validate the computational data and determine cell viability under set environmental conditions (external pressure and volume flow rate of cell-laden hydrogel) through *in-vitro* testing.

This thesis defines indicative spraying parameters for delivering therapeutic cells to the human retina, based on a combination of computational modelling and experimental studies. Mathematical modelling provides the potential to transfer these findings to other organ systems, aligning with broader effects to develop cell delivery systems to treat organ disease and repair.

Impact statement

Millions of people worldwide suffer from vision impairment and sight loss; mostly affecting the aging population in the UK and currently imposing expenditure of over £6 billion per year to the UK economy (including unpaid care provisions, direct and indirect costs). Most individuals exposed to sight loss are women; with people from black and ethnic minority communities having greater exposure to associated risk factors. Sight loss is strongly linked to other medical conditions and lifestyle factors, such as diabetes and obesity. If preventable measures are not implemented early enough, the number of people with sight loss is set to double to nearly four million by 2050.

Chronic eye diseases are the main cause of vision loss among adults. Among these, retinal degenerative diseases affect millions of people globally, causing permanent loss of cells and organ dysfunction. Although current treatments for retinal diseases alleviate associated symptoms and risk factors, they fail to replace damaged tissues and lost cells. Despite recent progress in developing stem cell therapies for retinal diseases, methods for delivery are still a subject of intense research. Aerosol technology is a promising technique with the advantage of spraying cells evenly and directly across the retinal surface, to promote cell attachment and survival. This technique was initially introduced as treatment for cutaneous wounds; spraying devices currently available in the market, are designed for large organs, thus making it difficult to tune for smaller geometries such as the human eye. Cell-based therapies provide a diverse range of treatment options and spraying of cells directly to the affected area is one delivery mechanism that has been shown to promote cell proliferation and cell viability and accelerate the healing process. The requirements of cell spraying are specific to the individual, for example due to geometric variability from person-to-person. It is essential to understand the link between cell spraying outputs (such as droplet speed and their spatial

distribution at the retinal wall, thickness of cell-laden hydrogel also at the retinal wall) and inputs (air pressure at the injector, nozzle dimensions, volume flow rate of cell suspension). Optimization of cell spraying parameters (such as volume flow rate, air pressure and surface area covered), is costly to define experimentally, thus creating the need for an alternative rapid and cost-effective technique. Here we use computational modelling as a tool to simulate delivery of stem cells onto the inner retinal surface and define spraying parameters for aerosol systems. Data produced from this multidisciplinary approach informs operating parameters for potential cell-based therapies for retinal degenerative diseases such as glaucoma. Computational modelling also offers a platform whereby animal studies could be minimised and reduced. By deriving organ-specific spraying parameters, this approach could further be extended to other organs around the body and facilitate future development of cell-based therapies.

This research provides strong evidence that delivery of stem cells onto the retinal surface can be controlled using parameters of the spraying process. The mathematical models provide guidance on how these parameters should be chosen, and these are subsequently tested experimentally. The novel approach introduced in this research opens the door for further computational approaches to inform treatments for restoring function of the damaged retina.

Publications

Journal papers

Nweze, M, Baker, T., Limb, A.G. and Shipley R.J. Insight into the Design of Spray Systems for Cell Therapies for Retinal Disease using Computational Modelling. *Mathematical Biosciences and Engineering.*2020.17(3): 2741-2759

Conference presentations

Nweze, M, Baker, T., Limb, A.G. and Shipley R.J. Computational modelling as a tool to accelerate designs of spray systems for cell-based therapies to treat retinal diseases. April 2018. Hawaii, USA. (Oral/ Poster Presentation).

Nweze, M, Baker, T., Limb, A.G. and Shipley R.J. Defining parameters for spraying cells for glaucoma treatment using mathematical modelling. Tissue and Cell Engineering Society, July 2017. Manchester, UK. (Poster Presentation).

Nweze, M, Baker, T., Limb, A.G. and Shipley R.J. Mathematical modelling as a tool to inform the design of spray systems for cell-based therapies. FIRM Symposium. September 2016. Girona, Spain. (Oral Presentation).

Nweze, M, Baker, T., Limb, A.G. and Shipley R.J. Mathematical modelling as a tool to inform the design of spray systems for cell-based therapies. Tissue and Cell Engineering Society, July 2016. London, UK. (Poster Presentation).

Contents

Acknowledgments…….. 3
Abstract…….4
Impact statement…….5
Publications..……...7
Thesis layout……12
1. Introduction 22
1.1. Anatomy of the eye 23
1.2. Retinal Diseases and Glaucoma 30
1.3. Therapeutic Stem Cells for Retinal Diseases 33
1.3.1. Embryonic stem cells 36
1.3.2. Adult tissue-derived stem cells 37
1.3.2.1. Mesenchymal stem cells 37
1.3.2.2. Induced pluripotent stem cells 38
1.3.2.3. Müller glia stem cells 39
1.4. Summary and Perspectives 41
2. Methods of Delivering Therapeutic Cells to the Retina 43
2.1. Requirements of spraying systems 44
2.2. Cell Delivery 48
2.3. Cell spraying 49
2.4. Theory of aerosolization 52
2.5. Atomizers 54
2.5.1. Pressure atomizers 56
2.6. Basic processes of atomization 59
2.7. The evolution of spray-based systems for application in industry and medicine 65
2.7.1. Dual syringe and dual cannula delivery head 68
2.7.2. Pistol grips 71
2.7.3. Dual channel pump sprays 72
2.7.4. Gas driven applicators 72
2.7.5. Baxter Healthcare Easyspray System™ 74
2.8. Microsurgery in the retina 77
2.9. Experimental protocol derived from animal study as benchmark to develop future procedure stem cell delivery 79
2.9.1. Modelling the multiphase flow 83

2.10. Summary 86
2.11. Research Objectives 87
3. Experimental Characterisation of Material Properties of Hydrogel Scaffolds 90
3.1. Biomaterials in ophthalmology 91
3.2. Fibrin glue 96
3.2.1. Fibrin-derived hydrogel material properties 98
3.3. Results: Rheological Parameters of Fibrin-Based Hydrogels 101
3.4. Discussion 104
4. Computational Modelling of the Delivery of a Cell-Laden Biomaterial to the Retina 106
4.1. Computational modelling 109
4.2. Reconstruction of the 3D model 109
4.3. The Mathematical model 109
4.4. Eulerian Approach vs Lagrangian Approach 113
4.5. Dispersed phase – droplets 115
4.6. Derivation of Navier-Stokes Equations for Flow of a Single-Phase Fluid 118
4.6.1. Mass conservation 118
4.6.2. The momentum equation 119
4.6.3. Non-Dimensionalisation of Navier-Stokes equation 121
4.7. Discretisation 124
4.8. Results 136
4.8.1. Convergence study 136
4.8.2. Simulation predictions 139
4.8.3. Droplets' speed and wall shear stress on the retinal surface 140
4.9. Spatial distribution of cellular thickness distribution at the retinal wall 144
4.10. Covered surface area of the retina 151
4.11. Droplets dimension 153
4.12. Discussion 157
5. Experimental Assessment of Spraying Parameters 162
5.1. Cell culture 163
5.2. Cell Spraying 163
5.3. Results 165
5.3.1. Surface area covered 165
5.3.2. Cell viability 168
5.4. Discussion 174
6. Conclusion and Future Recommendations 176
6.1. Review of objectives 177
6.2. Overall aim 178

6.3. Summary of research achievements 179
6.4. Limitations 180
6.5. Research bottlenecks 181
6.5.1. Measuring droplets size 184
6.6. Conclusion 189

List of Figures

Figure 1.1. Hand-drawn of the human eye, showing key anatomical features. See Figure 1.2 for structure of highlighted quadrant. 25
Figure 1.2 Schematic diagram showing important features around the limbus, where incisions are made during eye surgery for retinal diseases such as glaucoma (1). 26
Figure 1.3 Figure of the retinal layer, modified from Koeppen and Statton (2008) (7). The light is perceived through the layers, to reach photoreceptor rods and cones. 28
Figure 1.4 Potential sources of stem cells to treat glaucoma. Derivation of stem cell for optic nerve regeneration are categorised from tissue level to cell level. The stem cell type that will be the focus of this thesis is clearly differentiated from the other stem cell types identified from the literature (yellow and blue respectively. 35
Figure 2.1 Schematic diagrams for the two types of spray pattern produced from simplex atomizers, of which circumferential patterns is dependent on the nozzle design. (a) Hollow cone: produced when most of the droplets are concentrated at the outer cone edge of the conical spray patter and (b) Solid cone: droplets are mostly uniformly distributed throughout volume of the cone pattern (65). 58
Figure 2.2 Stages of spray development as injection pressure is increased; modified from Lefebvre (2017)(65). 58
Figure 2.3 Basic type of globules formation derived by (65).Lenticular deformation: the droplet is flattened and forms an oblate ellipsoid; this is indicated with a solid line as an elliptic shape. The subsequent deformation depends on the magnitude of internal forces that cause the deformation. Cigar shaped deformation: the initial droplet elongates into a long ligament, in turn breaking into smaller drops. Bulgy deformation: the drop surface turn into a bulge, that in turn creates smaller daughter droplets from parent droplets (65). 61
Figure 2.4 Drop formation mechanism (65).(a) Drop formation without air influence, showing a radially symmetrical wave following interactions between the liquid surface tension forces and disturbances in the liquid. (b) Drop formation with friction and aerodynamic forces cannot be neglected as jet velocity increases. (c) Breakup caused by air frictions as aerodynamic forces increase (65). 64
Figure 2.5 Spray applicators developed and respective key features with respective clinical application recorded in the literature. Some of the features developed are not limited to dual syringe (a), single hand operation, closely representing the Baxter Easyspray system used in this thesis (b), manually operative valve (c), application for large areas (d), vials with different cross-sectional area (e), ease of manipulation at various orientations (f), dual cannula delivery head (g), syringes with different orifice size (h), pistol grip (j), fluid components stored in parallel (k), introduced housing for gas supply (l), multiple lumen body attachment (m) and components delivery through separate channels (n). 67
Figure 2.6 (a) Baxter Easyspray set components and (b) different needles used for different clinical applications (95,96). 76
Figure 2.7 Two dimensional schematic diagram for the Easyspray System shown in Figure 2.6, comprising of the dual syringe system, showing secondary inlet for external air pressure and needle through which the cell-laden hydrogel will be sprayed through. 76
Figure 2.8 Schematic diagram comparing sizes of lens and vitreous of (a) a small rodent with a mean axial length of 6.9 mm, (b) a human eye with mean axial length of 23.9 mm and (c) a feline eye with mean axial length of 20.9 mm. It is clearly

illustrated the small rodent eye has a large lens and smaller volume of vitreous humour. The human eye on the other hand, as a larger volume of vitreous humour and a smaller lens, which surgical access to the vitreous cavity more challenging (5). 81
Figure 2.9 Incisions made on the cat's sclera, shown through the blue lines and the red line (5). 82
Figure 2.10 Human eye illustrating the vitrectomy procedure carried out. The cannula and the vitrector is used to extract the vitreous humour (100)..... 82
Figure 2.11 Anatomy of the human eye with a typical average diameter of 25 mm, showing the location of the vitreous fluid, covering ¾ of the human eye's volume (101). 84
Figure 2.12 Computational and experimental objectives for this research. 87
Figure 3.1 Thrombin and fibrinogen are diluted into PBS and mixed to produce hydrogels at a range of concentrations which then underwent rheological testing. Fibrinogen concentration was kept constant at 0.50 mg/ mL, whilst thrombin was diluted from 0.30 U/mL to 0.04 U/mL. 100
Figure 3.2 Fibrin derived hydrogel sample applied on the rheometer metal plate with a diameter of 40 mm for mechanical testing, using the Discovery Hybrid Rheometer-3 (TA Instruments). 100
Figure 3.3 Viscosity of fibrin-derived hydrogels with a fixed fibrinogen concentration (0.50 mg/ mL) with a range of thrombin concentrations, as a function of time, as determined via rheological testing (error bars represent standard deviation based on n= 3 repeats).the total volume for each mixture is mantained contstant at 420 µL. 103
Figure 3.4 Dynamic viscosity as a function of time for fibrin-based hydrogels with constant fibrinogen concentration (0.50 mg/ mL) and a range of thrombin concentrations (results show mean viscosity with error bars representing the standard deviation based on n=3 repeats). Total volume for each hydrogel mixture is fixed at 420 µL. In general, higher thrombin concentrations yielded hydrogels with a higher viscosity. 103
Figure 4.2 Schematic representation of the simulation geometry, showing the injector nozzle, optic nerve and retina locations. For the simulations presented here, the diameter of the eye (measured to the sclera) is fixed at 25 mm, the diameter to the retina is approximately 24 mm, and the injector has an inner diameter of 0.6 mm, positioned with its outlet at (x_1, y_1, z_1) mm. The position of the nozzle defines the distance s, which is the distance between the nozzle position and the sclera. The geometry between points A and B represents the geometry modelled in the 3D mathematical. 112
Figure 4.1 Fixed control volume V in a lab frame, where the streamlines are used to visualise the fluid flow. 118
Figure 4.3 Geometry of the eye with assigned mesh, showing refinement of the edge element size from 0.6 mm (a) to 0.8 mm (b)..... 127
Figure 4.4 3D model with defined boundaries (wall and pressure inlet). 127
Figure 4.5 A sketch of the transition of fluid to external spray, also showing the three stages of the LISA model (105). 132
Figure 4.6 Order of physics models selected in Simcenter STAR-CCM+. 135
Figure 4.7 Distribution of thickness of the sprayed cell-laden hydrogel at the retinal wall (referred to as fluid film thickness) using various edge element size, varied between 2.0 to 0.3 mm. The film thickness was obtained upon spraying the cellular suspension onto the inner retina at a spraying duration of 1s at a pressure of 25 kPa and outer cone angle of 50°. The illustrations show an increase of the total

thickness of the cell-laden hydrogel at the retinal wall with reduced edge element size. 138
Figure 4.8 Mean and variability in droplet speed on the retinal surface for varying injector pressure (volume flow rate and outer cone angle held fixed at 400 µL/s, 50° respectively; error bars +/- 2 standard deviations from the mean). 142
Figure 4.9 (a)The retinal surface is sprayed with volume flow rate of 250 μLs^{-1} at a pressure of 25 kPa The region of the retinal wall covered with the hydrogel, referred as threshold, is used to calculate the average wall shear stress (WSS) magnitude at the retinal wall. (b) The cellular scaffold is sprayed at a volume flow rate of 400 µL/s at a pressure of 100 kPa at the injector. We present WSS magnitude values covering different surface area at the retinal wall, expressed through outer cone angles 5° to 100° (n=3 repeats, R^2=0.80, $p < 3.13x\ 10^{-6}$). 143
Figure 4.10 Logarithmic scale of fluid film thickness distribution on the retina, with varying volume flow rate between 150 to 275 µLs-1, at a constant pressure condition of 10kPa at the injector and an outer cone angle of 50°. 147
Figure 4.11 The maximum film thickness at the retina surface (y-axis) has an exponential relationship with the volume flow rate (x-axis), for each given pressure value and at an outer cone angle of 50°. Data points show the mean, and error bars +/-1 standard deviation from the mean when averaging across the spatial domain. Lines show fitted exponential relationship based on defined relationships in Table 4.4 with R^2 values for each regression line (ranging between 0.91 and .98) summarised in Table 4.3. 148
Figure 4.12Coefficents A and B relationship defined as y = 0.014 -0.035x (R^2=0.99). This relationship can be used to predict future empirical equations for other pressure conditions which could be investigated in future research. 149
Figure 4.13 A histogram of film thicknesses by CFD elements. Here we present film thickness distribution at the retina l wall, with outer cone spraying angle of 50◦, volume flow rate of 200 µL/s and external pressure of 25 kPa applied at the injector. 150
Figure 4.14 The 3D eye model with a diameter of 25 mm; and a demonstration of how the droplets' spatial and temporal distribution are tracked in time, at an outer cone angle of 30°, with the z-axis representing the direction of the trajectory of the sprayed droplets. 152
Figure 4.15 Relationship between surface area covered and outer cone angle, varying between 5° to 100°, using volume flow rate of 250 µL/s at 25 kPa and 400 µL/s at 100 kPa. Data points indicate average values for 3 repeats and and error bars +/- 1 standard deviation of the mean. 152
Figure 4.16. The cellular scaffold is delivered at 200µL/s, with a pressure of 25 kPa at the injector. Droplet size distribution at the retina wall using the Rosin-Rammler cumulative distribution function, with a diameter peak value of about 325 µm and an outer cone angle of 50°. 155
Figure 4.17 The cellular scaffold is delivered at 200µL/s, with a pressure of 70 kPa at the injector. Droplet size distribution at the retina wall using the Rosin-Rammler cumulative distribution function, with a diameter peak value of about 180 µm and an outer cone angle of 50°. 156
Figure 4.18 The cellular scaffold is delivered at 200µL/s, with a pressure of 100 kPa at the injector, with reduced parcel number. Droplet size distribution at the retina wall using the Rosin-Rammler cumulative distribution function, with a diameter peak value of about 170 µm and an outer cone angle of 50°. 156

Figure 5.1 (A) Column graph showing surface area covered (mm^2, y-axis), which was assessed experimentally post-aerosolization(error bars +/- 1 standard deviations from the mean). Spraying was conducted at three pressure conditions (50, 70 and 100 kPa) using the Baxter Healthcare spraying system. Each fluid is sprayed at a volume flow rate of 400 µL/s for on a petri dish covered with filtered sheet. The covered surface is calculated using ImageJ software. The data indicates average values for the surface area covered and the error bars representing standard deviation averaged over 3 repeats, and later summarised to closely look at the surface area sensitivity of surface area covered at different pressure conditions with the cell-laden hydrogel (B). 167
Figure 5.2 Viability of Müller stem cells sprayed with the Baxter Healthcare Easyspray system at pressure of 100 kPa using trypan blue staining using a Leica TCS-SP2 confocal microscope at 20x magnification. Images were processed through Leica AF Lite Confocal Software and ImageJ for further analyses. After being cultured, cells are mixed with the fibrin-derived hydrogel (with a thrombin concentration of 0.08U/mL) and sprayed at a volume flow rate of 400 µL/s on a 6-well plate and applying an external pressure of 100 kPa and the second inlet of the spraying device. The sprayed cell laden-hydrogel is then coated with 50 µL trypan blue, diluted into 200 µL of PBS. The red arrows indicate the dead cells and the green arrows the live cells (scale of 50 µm). The experiment was repeated three times. 170
Figure 5.3 Viability of Müller stem cells sprayed with the Baxter Healthcare Easyspray system at pressure of 70 kPa using trypan blue staining using a Leica TCS-SP2 confocal microscope at 20x magnification. Images were processed through Leica AF Lite Confocal Software and ImageJ for further analyses. After being cultured, cells are collected using fibrin-derived hydrogel (with a thrombin concentration of 0.08U/mL) and sprayed at a volume flow rate of 400 µL/s on a 6-well plate and applying an external pressure of 70 kPa and the second inlet of the spraying device. The sprayed cell laden-hydrogel is then coated with 50 µL trypan blue, diluted into 200 µL of PBS. The red arrows indicate the dead ells and the green arrows the live cells. Images were taken at 20x magnification. The experiment was repeated three times. 171
Figure 5.4 Viability of Müller stem cells sprayed with the Baxter Healthcare Easyspray system at pressure of 50 kPa using trypan blue staining using a Leica TCS-SP2 confocal microscope at 20x magnification. Images were processed through Leica AF Lite Confocal Software and ImageJ for further analyses. After being cultured, cells are collected using fibrin-derived hydrogel (with a thrombin concentration of 0.08U/mL) and sprayed at a volume flow rate of 400 µL/s on a 6-well plate and applying an external pressure of 50 kPa and the second inlet of the spraying device. The sprayed cell laden-hydrogel is then coated with 50 µL trypan blue, diluted into 200 µL of PBS. The red arrows indicate the dead ells and the green arrows the live cells. Images were taken at 20x magnification. The experiment was repeated three times. 172
Figure 5.5 The mean cell viability of the sprayed Müller stem cell lines MIO-M1 (5 million cells) with the pressure at the injector (x-axis) sprayed at a volume flow rate of 400 µL/s on a 6-well plate with the fibrin-derived hydrogel, with constant fibrinogen concentration (0.5 mg/mL). Data points show the mean cell viability, with error bars representing the standard deviation based on n=3 repeats ($p<0.38$). .. 173
Figure 6.1Suggested future work planogram. Future studies will be conduct both mathematical modelling and experimental assessment. The experimental assessment will involve measuring droplet size of cell-laden hydrogel with a droplet

sizer and measuring outer cone angle from spraying using high speed cameras. The parameters developed in this study will be implemented experimentally. Data gathered from the experimental data will be used and validated with dataset from computational modelling from this thesis. There will be an additional segment including aerosolization on 3D models of human eye and animal eyes, followed by in-vitro testing with animal models. Finally output parameters will also be evaluated. Operating relationships predicted from this thesis will be used to establish hypothesis on this future work..... 183
Figure 6.2 The illustrations show a 2D representation and overall set up of the Malvern Spraytec Instrument (a). The Spraytec and spray orientation (grey cone angle) are also illustrated (b). The optical head is adjusted in a controlled manner, as such that the laser measures the droplet size. 187
Figure 6.3 Malvern Spraytec setup, showing Baxter spraying system position on a clamp stand. The equipment will be spraying into 3D printer eye models prior to using animal eye models. This setup will be used to determine droplet dimensions and for measuring outer cone angle during each spraying event. 188

List of Tables

Table 2.1 Comparison of different types of atomizers, with their characteristics and examples of applications, which will be taken into account when selecting a suitable atomization type for this thesis (Information extracted from Lefebvre (2017) (65). . 55
Table 3.1 Biomaterial Characteristics identified during a range of clinical applications (107). This table summarises the use of biomaterials in various of clinical settings, along with their respective outcomes met during the stated applications..... 94
Table 4.1 Table of supported meshes in Simcenter STAR- CCM+..... 128
Table 4.2 List of parameters used for the computational model. 128
Figure 4.11 The maximum film thickness at the retina surface (y-axis) has an exponential relationship with the volume flow rate (x-axis), for each given pressure value and at an outer cone angle of 50°. Data points show the mean, and error bars +/-1 standard deviation from the mean when averaging across the spatial domain. Lines show fitted exponential relationship based on defined relationships in Table 4.4 with R^2 values for each regression line (ranging between 0.91 and .98) summarised in Table 4.3..... 148
Table 4.4 Exponential relationships linking maximum film thickness (mm, y) with volume flow rate (µL/s, x), at different inlet pressures, as summarised in Figure 4.11. R^2 values quantify the variation of maximum film thickness at the retina wall, accounted by the variation in volume flow rate..... 148

List of abbreviation and notations

2D	Two dimensional
3D	Three dimensional
AMD	Age-related macular degeneration
ATP	Adenosine triphosphate
CFD	Computational fluid dynamics
CNS	Central nervous system
DMEM	Dulbecco’s Modified Eagle Medium
ECM	Extracellular matrix
ESCs	Embryonic stem cells
FG	Fibrin glue
HA	Hyaluronic acid
hES	Human embryonic stem cells
IOP	Intraocular pressure
iPSCs	Induced pluripotent stem cells
kPa	Kilopascal
LISA	Linear instability sheet atomization
MGCs	Muller glia cells
mg	Milligram
mL	Millilitre
µL	Microliter
mm	Millimetre
mmHg	Millimetre mercury
MSCs	Mesenchymal stem cells
Pa	Pascal
PBS	Phosphate- buffered saline
PEG	Poly (ethylene-glycol)
PLGA	Poly (lactic-co glycolic acid)
PLLA	Poly (L-lactic acid)
POAG	Primary open angle glaucoma
RGCs	Retinal ganglion cells

s	Seconds
t	Time
K^+	Potassium
PEDF	Pigment epithelium-derived factor
TGF-β	Transforming growth factor beta 1
VEGF	Vascular endothelial growth factor

Thesis Layout

Following this section, this thesis is structured as follows:

- Chapter 1: A literature review to understand the anatomy and physiology of the eye, followed by an overview of the most common degenerative retinal diseases leading to visual impairment or complete blindness. Glaucoma is one of the most common ones; incidence and prevalence of the disease are briefly discussed, followed by current treatment options and potential sources of stem cells for prospective cell-based therapies.

- Chapter 2: Several methods of cell delivery are identified from the literature and discussed with their advantages and disadvantages. Cell spraying is identified as the most suitable technique. Thus, associated aerosolization theories and nozzle designs are analysed and the evolution of spray systems developed over the years is reviewed (with the aim to outline important features for future spray systems). The proposed experimental protocol used as benchmark for computational and experimental analyses is also introduced.

- Chapter 3: To computationally replicate the experimental protocol introduced in Chapter 2, a suitable organic hydrogel is suggested through a selection process of biomaterials used in ophthalmology and medicine. Mechanical testing of the chosen hydrogel is presented to characterise rheological parameters for the computational model in Chapter 4.

- Chapter 4: A computational model of the spraying process is presented, based on multiphase mixture theory. Mechanical properties of the hydrogel (viscosity and density) determined in Chapter 3 are inputs into the computational framework. The model is simulated on a hemispherical geometry with realistic human eye dimensions. Boundary conditions are imposed to mimic spraying and environmental conditions. Sensitivity

analysis for film thickness at the retinal wall (as a key output) are performed to determine operating equations for the spraying process.

- Chapter 5: Key relationships proposed in Chapter 4 are validated in an experimental setup, using a commercially available dual spraying system and well-plates used for *in vitro* experiment and analyses. The impact of varying injector volume flow rates and pressures on the viability and surface area of delivered cells are evaluated. The validation process consists of carrying out cell viability test, by exploring selected volume flow rates and pressure conditions implemented in the computational modelling.

- Chapter 6: Conclusions of this interdisciplinary research and opportunities for future work are discussed. The benefits associated with the application of computational modelling in tissue engineering, specifically degenerative retinal diseases are presented, followed by future recommendations.

1. Introduction

Chronic eye diseases lead to permanent loss of cells, retinal dysfunction and damage to other vital underlying tissues in the eye; in turn leading to vision loss and in some cases blindness. Current palliative treatments aimed to supress associated risk factors (for example, reducing high intraocular pressure in some cases) fail to restore loss of permanent cells, tissue damage and retinal dysfunction potentially leading to optic nerve deterioration. As such, despite performed treatments, vision loss and blindness may still occur. This highlights the need for replacing damaged cells by introducing cell therapies, involving stem-cell delivery onto the damaged tissue to promote cell viability and proliferation. However, delivery of these cells remains a challenge and there is evidence supporting the use of cell aerosolization as a promising clinical method for effective cell delivery. With the need for developing cell-based therapies for retinal treatments, this thesis aims to use mathematical modelling as an insight for developing aerosol spraying parameters, to design prospective spray systems for cell delivery into the eye.

In order to provide a general understanding of the underlying structure and function of the human eye, this Chapter begins with a review of the relevant anatomy and physiology. Next, retinal disease such as glaucoma are briefly discussed, together with their effects on the eye anatomy. Current treatments for retinal diseases are presented, as well as limitations and opportunities for developing cell-based therapy delivery strategies in this thesis.

1.1. Anatomy of the eye

The eye is the organ of photoreception, which is the mechanism through which light energy information is transmitted to the brain through specialised nerve cells known as rods and cones in the retina. When information is transmitted, these signals travel through the optic nerve onto the brain, where they are then processed and translated as vision. The geometry of the eye can be approximated to that of a sphere with a volume of approximately 6.5 mL in

humans (1). Its axial length varies from person to person, with a mean value of 24 mm. Small adult eyes have a horizontal length of less than 20 mm, also known as hyperopic or hypermetropic, whilst large eyes ranging between 26 to 29 mm are defined as myopic (2).

The eye is filled with a liquid known as intraocular fluid; the intraocular fluid is enclosed by three layers of tissue (as shown in Figure 1.1). The outer layer is the sclera, a fibrous tough white tissue. At the front of the eye, there's an opaque outer layer called cornea, which is a specialised transparent tissue that allows light rays into the eye. The middle layer has three continuous structures: the ciliary body, iris and the choroid. The ciliary body is a ring of tissue surrounding the lens and is responsible for the aqueous humour formation. The iris is the coloured circular component of the eye. Although the eye is assumed to be a single sphere, it is formed by two spheres; a small one located anteriorly where the cornea is, and a large one located posteriorly, where the sclera is situated.

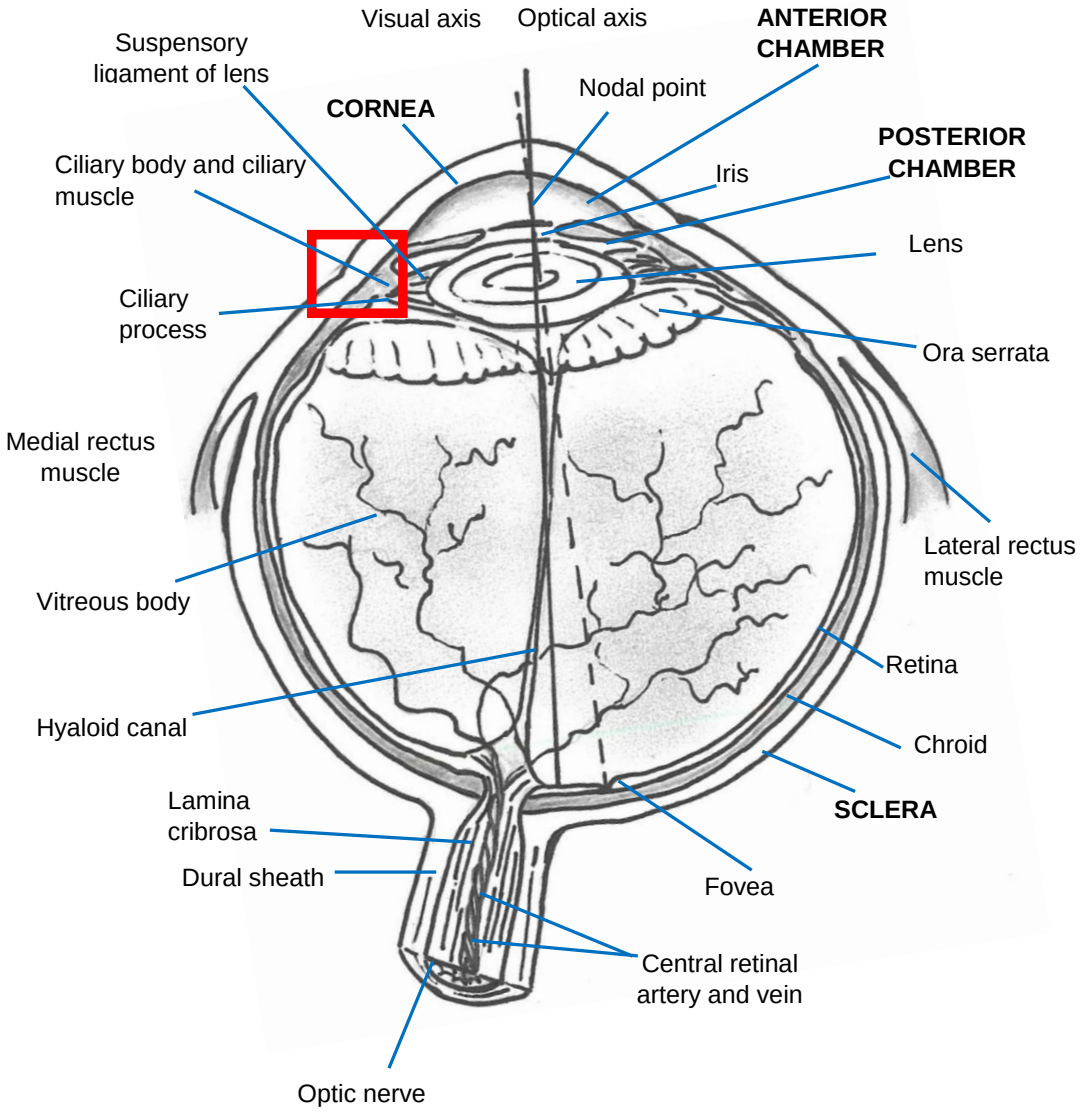

Figure 1.1. Hand-drawn of the human eye, showing key anatomical features. See Figure 1.2 for structure of highlighted quadrant.

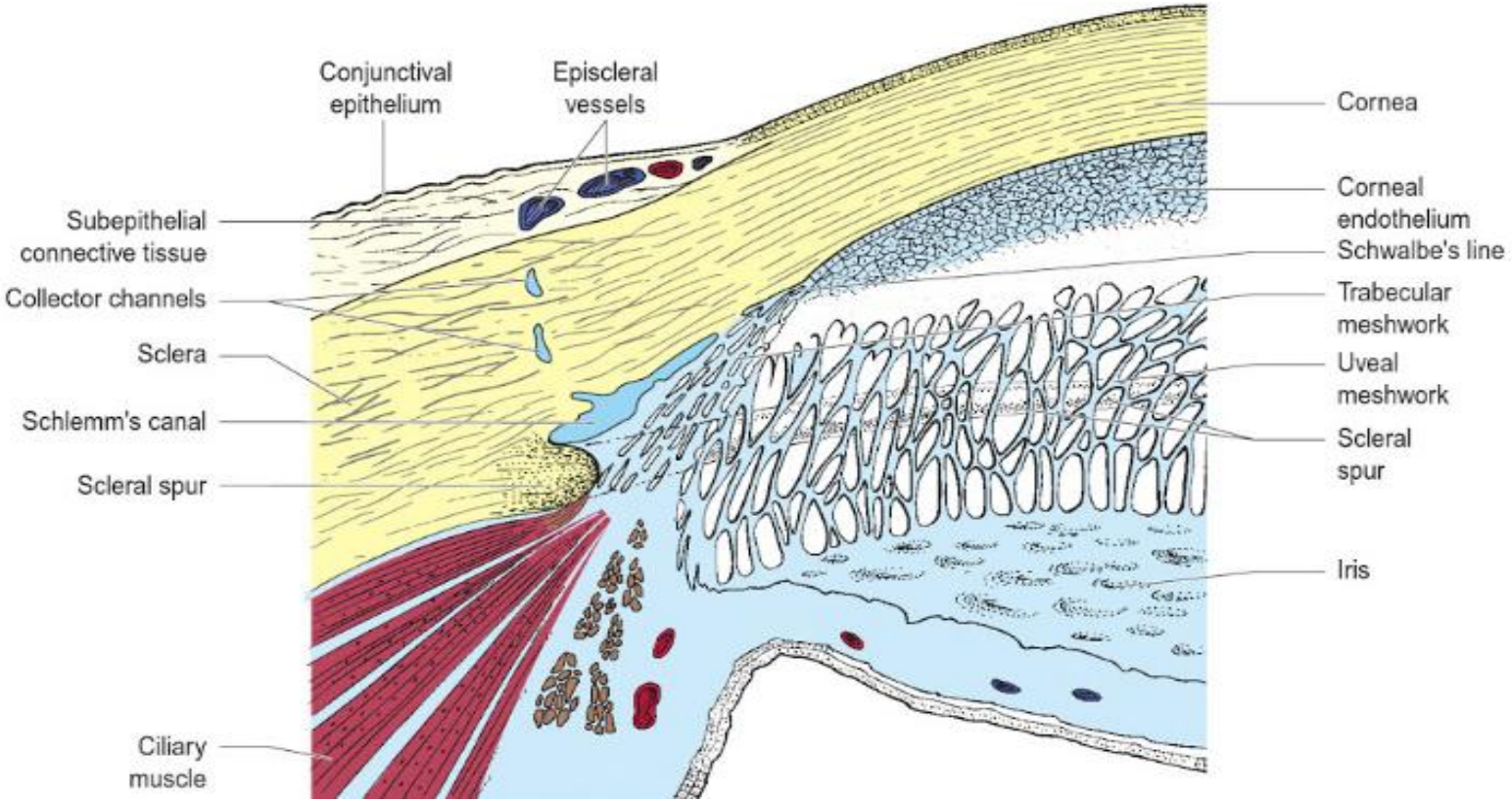

Figure 1.2 Schematic diagram showing important features around the limbus, where incisions are made during eye surgery for retinal diseases such as glaucoma (1).

The cornea makes a sixth of the eye, and the sclera forms the remaining five sixths. The eye comprises of both ectoderm and the mesenchyme. The ectoderm, which is derived from the neural tube, forms the retina, nerve fibres of the optic nerve and smooth muscle of the iris (3). The ectoderm surface on the side of the head gives rise to the corneal and conjunctival epithelium, the lens, the lacrimal and tarsal glands. The mesenchyme, on the other hand, forms the sclera, the corneal stroma, the choroid the iris, the ciliary musculature, part of the vitreous fluid and cells lining the anterior chamber. The choroid has a rich capillary bed acting as the main source of blood for the photoreceptors of the retina. Despite its location, the retina forms part of the central nervous system (CNS). The retina is continuously exposed to physical stresses, which may lead to tearing of the retinal tissue.

There are five types of neurons found in the retina: photoreceptors, bipolar cells, amacrine cells, ganglion cells, and horizontal cells. All these cells are neatly arranged further into three major regions: the outer nuclear layer, the inner nuclear layer and the retinal ganglion cell (RGC) layer (see Figure 1.3). The retina ganglion cells (RGCs) are situated in the RGC layer, through which the photoreceptors transmit electrical impulses of converted light through the optic nerve into the visual centres of the brain. Numerous studies have focused on the application of stem cells therapies as a promising treatment for glaucoma (4–6). A vital organ attached to the eye is the optic nerve.

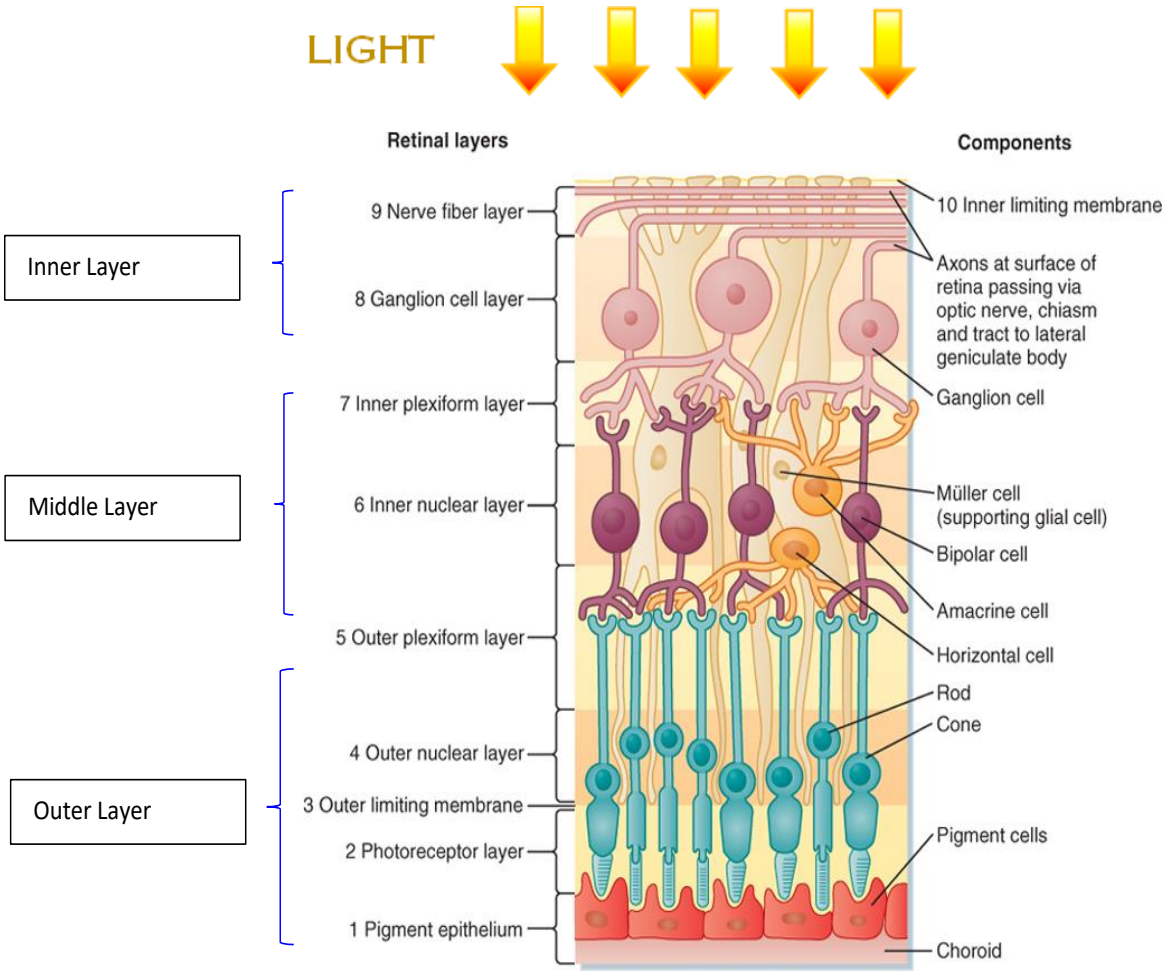

Figure 1.3 Figure of the retinal layer, modified from Koeppen and Statton (2008) (7). *The light is perceived through the layers, to reach photoreceptor rods and cones.*

The optic nerve is a white matter tract, which is surrounded by meninges, situated within the blood-brain barrier. The glia cells found in the optic nerve are the same as those in the brain and spinal cord. As such, the optic nerve is part of the CNS; pathological processes affecting CNS also affect the optic nerve, and vice versa. The CNS is a very soft and complex tissue in the body, with organised layers of neurons and glia cells. Although glia cells cannot provide structural support to neurons, they are responsive to mechanical signals and able to withstand tensile strength (8). The optic nerve head is the primary sight of damage during retinal diseases such as glaucoma. When the cable of the human optic nerve is damaged, it does not possess the ability to regenerate or heal itself, at which stage irreversible blindness takes place. In these circumstances, blindness is defined as irreversible, as the RGCs do not possess natural self-healing abilities; therefore, the damaged underlying cells cannot be replaced or restored. RGCs are non-uniformly distributed across the vertebrate's retina, which also has a non-uniform distribution of cone photoreceptors and regions rich in ganglion cells (9). There are approximately 1 million RGCs in the human retina (9); although the specific number varies from one person to another.

One of the functions of the eye is to continuously produce aqueous humour, a fluid responsible for nourishing neighbouring tissues by delivering oxygen and nutrients, and removing metabolic waste through the ciliary circulation (10). The aqueous humour leaves the eye through the open angle region between the iris and the cornea. Here, the fluid is drained through the spongy meshwork drain. When the aqueous humour does not drain properly or is overproduced, the fluid cannot evacuate at its normal rate, thus increasing the intraocular pressure (IOP) and damaging the optic nerve and the nerve fibres from the retina. As a result, one's vision capabilities are obstructed as the electrical impulses fail to be transmitted from the eye to the brain, leading to visual impairment and sight loss. This now leads the narrative to discuss retinal diseases.

1.2. Retinal Diseases and Glaucoma

According to the World Health Organisation, about 253 million people around the world live with vision impairment (11); among these, 36 million are registered as blind and 217 million suffer from a form of visual impairment. Vision loss is a major medical, social and economic issue (12). The prevalence of blindness and sight loss in the UK are known to impose substantial costs on public funds, health and private expenditure (13). Retinal degeneration is associated with loss of specialised nerve cells in the retina such as RGCs and photoreceptors. Retinal degenerative diseases such as retinitis pigmentosa, diabetic retinopathy, age-related macular degeneration (AMD) and glaucoma, are the main causes of blindness and cause major disability and impact on quality of life. Here we focus on glaucoma, although the approach developed in this thesis could be generalised to any retinal disease for which cell therapies were appropriate.

Glaucoma is defined as a group of progressive, chronic, neurodegenerative diseases and is the second most common cause of blindness affecting over 70 million people worldwide (14,15). Glaucoma is estimated to affect 0.9% of the UK population (16) of which about 2% are over the age of 40 (17,18). With increasing life expectancy, glaucoma is becoming more prevalent. The disease affects the retina through loss of RGCs and their axons, which are extensions of the CNS.

The loss of RGCs causes structural changes to the glia, connective tissues and vasculature, causing changes in the retinal nerve fibre layer (19) and thinning of the neuroretina rim of the optic nerve. These lead to enlargement of the optic-nerve cup, also known as optic- nerve cupping (20). During glaucoma, the remaining neuroretinal rim structure retains its normal pink colour; which is different from other neuropathies where the optic tissue loses its colour and nerve cupping does not take place (21). Individuals diagnosed

with glaucoma experience loss of peripheral vision, and if untreated, it may lead to complete vision loss (22). During glaucoma, the mechanical compression of the microvasculature affects the perfusion of the optic nerve head, in turn causing ischemia (reduced oxygen levels). This results in oxidative stress and production of free radicals.

There are known risk factors associated with glaucoma, which increase an individual's chance of developing the disease. The risk of developing glaucoma may be influenced by the patient's race (prevalent among those with African ancestry) (23), age, family history of glaucoma, central corneal thickness and the presence of certain systemic diseases such as hypertension, diabetes and cardiac disease (24). Racial differences are not only present in the prevalence and incidence of this disease, but also differences in anatomical features critical in detecting glaucoma, such as cup to disc ratio and disc size. Nevertheless, across ethnic groups, individuals at risk include those aged over 60, family members of diagnosed patients, diabetics and people who are severely near-sighted (myopic population). The prevalence and incidence of glaucoma increases with age, and it is therefore considered the most important risk factor in glaucoma. For example individuals over the age of 55 are seven times more likely to develop the disease (25). People aged between 70 and 79 years are three times more at risk of developing glaucoma compared to persons aged between 40 and 49 years old (26); perhaps due to changes within cells around the body, leading to mitochondria degeneration and increased exposure to soft tissue damage from toxic materials.

There are four main types of glaucoma: primary open angle glaucoma (POAG), angle closure, normal tension and secondary glaucoma. POAG is the most common type of glaucoma and prevalent in different ethnic groups. It can occur without elevated IOP. POAG is the leading cause of blindness among black people. Associated risk factors of POAG are family history of POAG, older age, ethnicity, elevated IOP, myopia and low diastolic perfusion pressure

(22). IOP increases in POAG as the aqueous humour moves too slowly blocking the drainage canal. In angle closure glaucoma the canal is either too narrow or closed completely. During normal tension glaucoma the IOP is low, but the optic nerve still gets damaged. Secondary glaucoma develops consequently to, or as complication from other conditions such as diabetes, eye surgery or tumours.

Elevated intraocular pressure (IOP) is identified as a major risk factor associated with glaucoma (22); however, not every individual with increased IOP develops glaucoma. When the IOP rises, it damages the optic nerve and the nerve fibres from the retina. As a result, the electrical impulses fail to be transmitted from the eye to the brain. Nevertheless, despite the discussed risk factors influencing the occurrence of glaucoma such as age, race, gender and IOP, there are several other factors influencing the development of the disease, as its origin is still not fully understood. The unknown causes of glaucoma hinder the ability to predict population requiring early treatments to prevent vision loss. Glaucoma is asymptomatic and generally painless (14), making it difficult for the disease to be diagnosed at its early stage. Despite several experimental and clinical studies, the development and progression of glaucoma is still unclear (27). As such, many patients remain undiagnosed until they reach the advance stage.

Treatments for retinal diseases usually depend on the disease itself; they can either be introduced at early stage of the disease or at a later stage (28). For example, current treatments for glaucoma are aimed are reducing the IOP through surgery or pharmaceuticals, by evacuating the accumulated aqueous humour through the trabecular meshwork (see Figure 1.2) (15). However, these methods do not restore the lost peripheral vision, nor lost cells following apoptosis. Further, reducing the IOP does not always prevent progression of the disease and evacuating the accumulated liquid does not guarantee IOP reduction. In this thesis, stem cell therapy is preferred as alternative treatment as it has the potential of replacing RGCs, trabecular meshwork cells (5,29)

and hopefully restoring vision loss, which conventional surgery for glaucoma currently fails to address. These cells can be delivered onto the retina via subretinal or intravitreal methods; subretinal delivery is more skill demanding and more invasive compared to the intravitreal route, which is easier, less invasive and requires using small needles. Given the importance of sourcing stem cells for retinal therapies, next we discuss potential stem cell sources for neural retinal cells replacement.

1.3. Therapeutic Stem Cells for Retinal Diseases

Stem cells are a special type of immature cell with the ability to self-renew and differentiate into different types of adult cells. They undergo asymmetric cell division, which generates other stem cells. Stem cell transplantation therapies have been of significant interest over the last decade, due to their outstanding potential for treating a range of currently incurable diseases such as osteoarthritis, multiple sclerosis, retinal degeneration and hopefully glaucoma. The goal of cell transplantation in glaucoma is to replace lost RGCs to achieve functional vision restoration. As such, there must be an outlined clinical protocol, which will consider an appropriate source of stem cells, method of delivery, host environment and intended outcome from transplantation. To-date, long-term restoration of visual function is yet to be achieved in humans using stem cell therapies.

Various sources of stem cells have been used experimentally for retinal transplantation (see Figure 1.4). Several studies have shown various sources of stem cells that could be used for cell-based therapies, as summarised in Figure 1.4. These include stem cells from embryonic tissue and adult tissue, as discussed next. An ideal cell-based therapy for glaucoma will replace the lost retinal cells, and the transplanted cells will incorporate into the structured retinal layer. The ideal stem cells candidate for retinal transplantation will be from sources that are readily available. The cells should easily expand in

culture, be safe for implantation, and limit the requirement to control the host immune response. Next the three potential stem cell sources (embryonic or foetal tissue, adult tissue and reprogrammed cells) are discussed alongside their potential as a therapeutic stem cell for retinal disease.

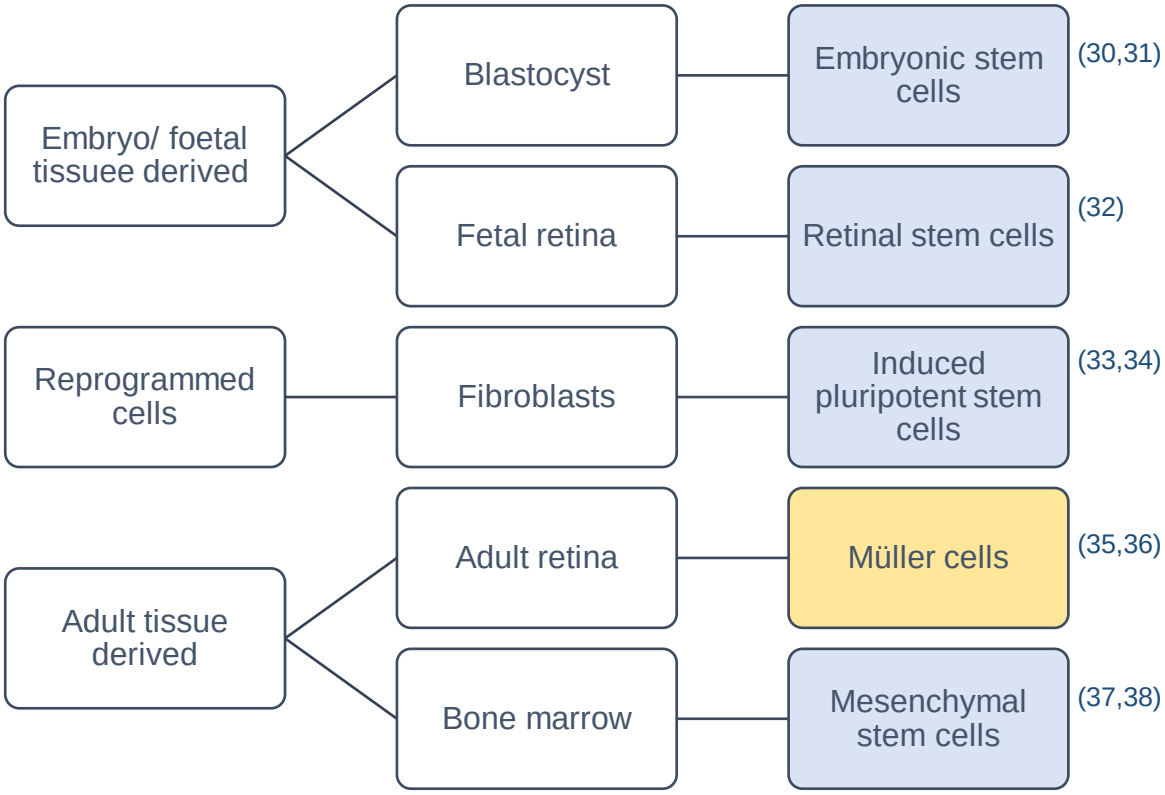

Figure 1.4 Potential sources of stem cells to treat glaucoma. Derivation of stem cell for optic nerve regeneration are categorised from tissue level to cell level. The stem cell type that will be the focus of this thesis is clearly differentiated from the other stem cell types identified from the literature (yellow and blue respectively.

1.3.1. Embryonic stem cells

Embryonic stem cells (ESCs) are pluripotent cells that can differentiate into any type of cell, such as neurons, retinal pigmented epithelium and RGC-type cells through controlled exposure to various growth and differentiation factors (39,40). The discovery of ESCs appeared to have revolutionised research into the application of stem-replacement therapies (41). ESCs can be derived from the inner cell mass of blastocyst-stage embryos and from the foetal tissue. In animal studies, they have demonstrated their ability of replicate into retinal progenitors and their potential for retinal transplantation (42). When human ESCs have been implanted in animal models, they have also shown successful integration into the retina structure (20,42,43). Although ESCs could be beneficial for development of cell therapies for retinal regeneration, further research is still required to determine whether ESCs could be induced to regenerate a damaged optic nerve and restore vision lost by glaucoma in humans. Furthermore, owing to the existing ethical constraints, the use of ESCs can be restricted and need appropriate regulations for their use. Although ESCs are considered a promising source of cells for treating retinal diseases such as glaucoma, protocols for appropriate neural differentiation and up-scaling to are still under investigation.

Retinal stem cells can also be derived from the foetal retina, as a single foetal eye holds many stem cells. These cells, known as retinal progenitors, have been transplanted into the eye of experimental animals such as rats, monkeys, rabbits and pigs, and they have showed successful differentiation into photoreceptors and RGCs survival in chickens (29). Many investigations have used ESCs derived from animals such as monkeys and rats. For example, Meyer et al (30) showed that implanted mice ESCs widely dispersed across the host mouse retinal layers, although not in a uniform distribution and assumed neuro-like morphology. Transplanted ESCs spread across most regions of the retina and after 6 weeks of transplantation, most cells attached to the inner retina surface and a few migrated into the inner retinal surface;

after 16 weeks of transplantation the cells undertook neuron-like characteristics. Promising results have also emerged when using human ESCs (29), which are stable and have proliferative capacity. Due to their proliferation capacity, ESCs are considered ideal candidate for human cell-based therapies. However, there are still concerns regarding their uncontrolled proliferation after transplantation *in-vivo*, which may lead to teratoma formation (44).

1.3.2. Adult tissue-derived stem cells

Adult tissue-derived stem cells are another therapeutic option, without some of the ethical issues associated with ESCs. There are various sources of adult stem cells that have been investigated for regeneration or replacement of retinal neurons. These include mesenchymal stem cells, induced pluripotent stem cells and Müller glial stem cells, as discussed below.

1.3.2.1. Mesenchymal stem cells

Mesenchymal stem cells (MSCs) are frequently sourced from bone marrow, blood, dental and adipose tissues. They have been shown to secrete neurotrophic factors, which promote neural cells' survival (45). MSCs can also differentiate *in-vitro* into different cell types (including neurons and glia) and can be easily isolated and enable autogenic transplantation. MSCs have been applied to treat retinal degenerative disease such as glaucoma and diabetic retinopathy in animals. Animal studies have shown that MSCs transplantation in the glaucomatous rat eye, can delay degeneration of retinal cells (46). They have also shown to stimulate axon regenerative response, however lack of graft survival interfered with upscaling of this procedure. This suggests that this cell type has the advantage of supporting retinal neuron survival when transplanted into tissues and organs connected to the CNS. As such, further

neuroprotective treatments could be developed to reduce RGCs death caused by glaucoma (47).

Many have observed their ability to differentiate into retinal neurons (29). Owing to the MSCs ability to secrete various cytokines, there is evidence supporting the use of MSCs for cell-based neuroprotective strategies, rather than neuron replacement, which will have potential benefits to treat retinal diseases, hopefully including glaucoma (48). However, despite these advantages, the clinical significance for MSCs to impose neuroprotective effects in glaucoma needs to be confirmed and validated with further research and relevant and controlled clinical trials.

1.3.2.2. Induced pluripotent stem cells

Induced pluripotent stem cells *(*iPSCs) were developed to bridge some of the disadvantages related to ESCs and have been considered a valuable source of cells for autologous transplantation (49). iPSCs can be derived from animal and human adult tissue cells by reprogramming adults fibroblasts using factors such as Oct3/4, Sox2, c-Myc and Klf4 (29). Subsequently they can be differentiated into various cell types (50). Deriving patient-specific iPSCs has opened a new clinical opportunity in medicine (41). The reprogrammed cells then exhibit growth properties and morphology of ESCs. Although iPSCs may help overcome limitations such as ethics and host tissue's immune response by using patient specific somatic cells (51), customised cell therapies are much more expensive and time-consuming. iPSCs studies associated with their scalability, adaptability and capacity to yield specific retinal cell types are still ongoing. Current barriers preventing clinical pursuit of iPSCs for retinal damage repair involve existing safety concerns that could introducing subsequent teratoma formation (29). As iPSCs are reprogrammed from adult cells, it is imperative for researchers to further characterize the full bioactive profile for these cells and potential alterations they could introduce in host

human tissues, such as gene mutation and structural variations in the genome that could impact patients' health (52,53). Yet, there still exist other impeding factors for iPSCs to be used for retinal damage repair; namely practicality on their clinical reproduction and economical methods to evaluate their pluripotent potentials (29).

1.3.2.3. Müller glia stem cells

In the retina there are three types of glial cells, neuron-supporting microglial cells, astrocytes and radial glial Müller cells (MGCs). Microglial cells are immune cells found in the inner retinal layer; they are responsible for defence against invading microorganisms and inflammatory processes, and for tissue repair. Retinal astrocytes are close to the superficial vascular region and the vitreo-retinal border. MGCs are the principal glial cell of the vertebrate's retina [34] and are specialised radial glial cells extending through the retina. These cells make an anatomical link between retinal neurons and the anatomical region where molecule exchange takes place. MGCs have different ion channels, enzymes and receptors, which play a vital role in supporting neurons and the functions they perform in the retina. They are essential in creating and maintaining the neuroretina architecture, support neurons survival and regulate information processing.

MGCs are the main glial cells of the retina and they can be obtained from cadaveric donors. The retina is continuously exposed to physical stresses, which may lead to tearing of the retinal tissue. Although retinal neurons are vulnerable to injuries and lack of blood supplies, MGCs are less susceptible to injuries such as ischemia, anoxia or hypoglycaemia(54). Glia cells cannot provide structural support for neurons; however, they are responsive to mechanical signals and able to withstand tensile stress (8).

In a healthy human retina, MGCs have several functions based on different physiological processes. For example, for the metabolic support and nutrition of neurons, MGCs deliver lactate and store glycogen and glycogenolysis (55). They are also involved in potassium (K^+) and water homeostasis, which is achieved through carbon dioxide buffering, by removing K^+ ions and dehydration of the inner retina (56,57). By removal of free radicals, the retinal tissue is protected against oxidative stress. MGCs act as transmitters for neuronal signalling and release neuroactive substance by storing and releasing ATP, D-serine and glutamate. Through the synthesis of VEGF, PEDF and TGF-β, MGCs release vasoactive substances (58). They are also involved in retinal development by acting as scaffold orientation for immature radial glia cells. Other functions of MGCs in a healthy retina include stabilising retinal blood flow (59), contributing towards maintenance and formation of the blood-retinal barrier (60) and maintain pH level and ion homeostasis of the retinal tissue.

Research in multiple species such as chickens, rats, mammals, rats and humans suggested that MGCs can proliferate and differentiate into several types of neurons. Research suggests that the MGCs are likely to make the retina more resistant to deformation from dynamic shear forces and tension to which the retina is continuously exposed (8,61). In zebrafish, MGCs are source of retinal neurons, with the ability to fully regenerate the retina after tissue damage (62).However, MGCs in mammals lack these properties; hence the need for cell transplantation in humans. These cells have also been identified in the adult human eye; although currently there is no evidence that human MGCs regenerate the human retina, MGCs can be isolated and successfully differentiated *in-vitro* to derive RGC precursors (63). Upon transplantation, these RGCs have shown successful attachment onto the rodent inner retina to induce partial recovery of RGC function. This could suggest that MGCs constitute a potential tool to treat sight loss in glaucoma (63). However, it is yet to be established whether MGCs can regenerate the retina (64), as testing on the human eye model is yet to be performed. Although there is currently no evidence suggesting MGCs regenerate the retina *in-vivo*, they can be isolated

and grown in culture when *in-vitro.* A study has shown that cell lines with characteristics similar to that of MGCs can be derived from the adult human retina (6).

1.4. Summary and Perspectives

In summary, the eye is a very important organ, of which metabolism plays an important role in transferring information to the brain through the retina, which acts as a cable. The retina is therefore a very important underlying structure due to its location and being part of the central nervous system. Retinal degeneration could lead to loss of neural cells, in turn leading to vision loss and is some cases blindness. As such, evidence highlights the need for replacing these lost cells through novel cell-based therapies, to treat retinal degenerative diseases such as glaucoma. Developing stem cell therapies for damaged retinal tissue has progressed over the recent years, as they have potential to replace lost and damaged cells by secreting neurotrophic factors (29). Transplantation of neural stem cells has significant potential in the restoration of retinal function and repair of retinal injury. It has been reviewed that currently there are several sources of stem cells and stem cell types that have been investigated in the literature for retinal transplantation.

ESCs have the ability of replicating in any type of cell and have demonstrated promising results and potential for clinical advancements, by integrating within mice's retina layers and surface attachment 6 weeks after transplantation. However, there are existing limitations associated with their uncontrolled growth post-transplantation *in-vivo*, that could result in teratoma. Adult tissue-derived stem cells are sought as alternatives to ESCs, specifically as they bridge ethical barriers. These include the use of MSCs, iPSCs and MGCs. MSCs can also differentiate into any type of cells including neural cells and secrete neuro-trophic factors. However, there is the need for further research and clinical trials to validate their success post-administration for glaucoma

treatments. iPSCs are developed by reprogramming human adult tissue and there is a great deal of research for their use in retinal repair. Nevertheless, there still barriers interfering with their progress into clinical trials that requires further characterization of their reaction with host tissues; namely potential gene mutation, structural genome variation that can endanger patients, teratoma formation, practicality for clinical reproduction, cost effective methods to evaluate their pluripotent potentials for retinal repair. MGCs, which provide metabolic and structural support to the retinal neurons, are produced from human donors and have a track record of research in multiple species, hence highlight their potential of differentiation in any type of neuronal. This thesis will therefore pursue using MGCs later in Chapter 5 to assist with experimental assessments.

It is therefore hoped that stem cell transplantation will reverse neurodegenerative diseases processes, following use of endogenous host tissue. As such, their use as vehicle to diffuse bioactive factors could potentially introduce retinal function restoration. The ideal stem cell therapy for retinal diseases such as glaucoma would be readily available, easy to culture and provide long-term safety to recipients. As such, there currently remains a question on practicality in delivering these cells into the human eye. Next, we present different strategies for stem cell delivery.

2. Methods of Delivering Therapeutic Cells to the Retina

This Chapter provides a comprehensive review of different methods of cell delivery to the retina. We focus on cell delivery via a biomaterial scaffold, and via a bolus injection or aerosolised spraying. Of these, aerosol-based spraying offers a significant opportunity with outstanding questions around control of the delivery that are the focus of this thesis. Aerosol-based spraying techniques have been developed for use in industrial applications, household products and agriculture, and have started to be used for biological applications. First of all, general requirements of spraying systems are reviewed, followed by potential requirements for spraying systems for ophthalmic applications. Different cell delivery approaches are discussed, with a focus on the unmet potential of spray-based systems. The underpinning theories and nozzle designs developed over decades for aerosolized spraying are discussed, finally narrowing down to a medical aerosol spraying equipment currently commercially available for several clinical applications and used for the experimental part of the research presented in this thesis.

2.1. Requirements of spraying systems

Lefebvre and McDonell (2017) (65) defines a criteria for ideal atomizer system for any application, together with wide reports from the literature. The general characteristics are defined as follows:

1. The ability to provide good atomization over a wide range of volume flow rates; a sprayed fluid needs to be effectively delivered onto a region of interest and the ability to cover various large areas. This is to be controlled through nozzle design and magnitude of external pressure supply (65);
2. Rapid response to changes in flow rates of liquids;
3. Low power requirements;
4. Flexible design for scaling capabilities;
5. Low cost, easy maintenance and light weight;

These characteristics can be replicates for ophthalmic application, based on the need for the cellular suspension to be uniformly distributed over the large retinal surface. It is believed that uniform distributions for cellular scaffold over the retinal area will promote cell viability and proliferation, as uniform distribution as equally favoured cell delivery for other laboratory application (66,67) . A major feature to maintain for prospective cell-based therapies is the homogeneous cell delivery over large areas of the inner retina in the human eye, which is an important requirement in scaling up such protocol for cell-based therapies in humans. Spraying parameters such as external air pressure, nozzle dimension and volume flow rate for the cellular scaffold have been identified as paramount through analyses of literature findings. We therefore identify three distinct categories; fixed parameters need for spraying, geometrical parameters and output parameters from the computational model. They are outlined below and occasionally referred to in forthcoming Chapters as required.

2.1.1. Fixed parameters required from spraying

The fixed parameters required for spraying and that will be defined during this thesis are the following:

- *Hydrogel concentration;* this is suggested once various mixtures of fibrin derived hydrogels are mixed and analysed (68). The material properties of the hydrogel will be characterised and used to predict the behaviour of the cellular scaffold.
- *Delivery period*; standard spraying protocols involve delivery over a period of about 1-2 seconds, which is substantial for the cell delivery.

2.1.2. Controllable parameters for spraying events

Although the following parameters are fixed during each sprayed event, they are also defined as controllable because they can be manipulated to widely observed behaviour of the desired outputs through the computational model.

- *Volume flow rate of cellular* suspension ; the vitreous in humans occupies a volume of 3.9—5mL (69). The volumetric flow rates currently used in the literature and recent animal studies (between 1 and 2 L/min) (70), can damage the human retina due to anatomical differences to rodent eyes (70). It is suggested the human intraocular flow is between 2.5 and 3 μL/min (69). However, the cellular suspension delivered is not required to fill the entire human intraocular flow, but only a portion of it; this will be address later in the thesis.
- *External air pressure*: supplied externally and applied at the injector nozzle to create aerosolization effects during each spraying event. Pressure values were derived from literature using the commercially available Baxter spraying system.

2.1.3. Geometrical parameters

These are geometrical parameters that will be later defined in the mathematical model of the human eye and are kept fixed throughout the simulations:

- *Injector nozzle;* with regards to nozzle dimensions, a 25G cannula (with an outer diameter of 0.5 mm), is frequently used for retina surgery (5). However, the viscous nature of fibrin-based hydrogels (71) will cause clogging of the fluid. The use of the 20G cannula (0.6 mm in diameter), promoted ease of manipulation and successful surgical procedure for the feline eye model (5). It is therefore hoped, that introducing a nozzle injector

with the same dimension as a 20G cannula in the 3D computational model, will be equally successful when spraying onto the retina.

- *3D model dimensions;* to support the 3D model of the spray system, a scaled model of the human eye will be used. This will help estimate true values of the parameters investigated, such as film thickness over the covered surface area, air pressure to be supplied at the injector and volume flow rate at which the cellular scaffold will be delivered (see Chapter 4).

- *IOP conditions;* the pressure within the domain is set to glaucomatous pressure (22 mmHg). The same environment should also be observed in the computational model when simulating cell spraying.

  The injection/ incision; must be carried out from a scleral area that is not occupied by the retina, with the aim of covering as much surface area as possible during aerosolization (approximately ¾ of the total surface area of a human eye).

2.1.4. Required outputs to be achieved by the computational modelling approach

The required output parameters to be extracted from the computational modelling are the following and strongly dependent on the specified on the controllable parameters:

- *Surface area coverage;* let's assume the eye is a complete sphere. In adult humans, the retina covers about 72% of the sphere (72). We predict the sprayed cellular scaffold should cover roughly ¾ of the inner surface area. We will use mathematical modelling to control the surface area to cover.

- *Cell-laden hydrogel distribution*: a homogeneous distribution of both cell and gel is required to promote cell migration and viability; and promote MGCs proliferation.

- *Cell population:* by estimating the surface area covered during a spraying event, it is hoped clinicians could further use mathematical modelling as tool to estimate population of cells needed per spraying event.

With a series of spraying parameters needed to be controlled for successful cell delivery and survival, we now proceed to discuss desired cell delivery methods with the potential to promote cell viability and proliferation in a fast and controlled manner.

2.2. Cell Delivery

Retinal tissue engineering shows potential in treating retinal degeneration using hydrogel scaffold-based delivery methods. Hydrogels have been used for decades for a wide number of medical applications such as neurosurgery, gastrointestinal surgery, orthopaedic, cardiovascular and cosmetic surgery (73,74). The goal of a cellular scaffold is to provide cellular support, promoting cell viability and cell proliferation once delivered into the body, and encouraging natural repair mechanisms so that the tissue regenerates healthily (75,76).

Retinal stem cells have been experimentally transplanted using cellular scaffolds made of biomaterials or by bolus injection. The first method involved embedding gelatine with embryonic retinal sheets into the host retina tissue (77). Although retinal sheets are known as excellent models for transplantation in rats, there is a shortage of human tissue for transplantation into rats, as retinal sheets cannot be cultured and expanded *in-vitro* (77). In these experiments, the transplanted tissue fails to integrate with the host tissue, at which stage the surgical procedure leads to the formation of a double layer of retina with no connection to the brain.

With the presented number of limitations associated with the retinal sheet transplantation, further research is required. Several studies have used bolus injection as an alternative, which involves delivering a known volume of cells through a needle. The literature has shown that stem cell injection in the sub-retinal space can bridge any integration problems within the host tissue, which were previously encountered using the retinal sheet transplant technique (77). The protocol of direct injection is considered technically demanding and time consuming. With the bolus injection cell survival post implantation needs to be overcome, as generally less than 1% of injected cells are viable only after 2-4 weeks of being injected (77). Biomaterials such as poly (L-lactic acid) (PLLA) and poly (lactic-co glycolic acid) (PLGA) have been used as cellular scaffold for retinal cell delivery through injection.

However, significant adverse reactions have been observed after implantation of such scaffolds. If cells could be delivered into the eye using suitable biodegradable materials that can be sprayed directly onto the retina surface, as well as viability of the cells. Further, cell injection can lead to poor cell survival owing to shearing forces during the injection (67). As a result, incorporating biodegradable biomaterials into the bolus appears to be an efficient method to promote cell survival and differentiation, as the biomaterial scaffold protects the cells from shearing forces, and provides a natural substrate for integration with the host tissue. The biomaterial substrate can be chosen based on natural proteins at the implantation site, for example fibrin, to further promote cell attachment and survival. Next cell-spraying methods are discussed, whereas biomaterials substrates are the focus in Chapter 3.

2.3. Cell spraying

Cell-spraying is potentially a rapid and innovative method for cell delivery into the eye compared to the existing delivery methods. This method was firstly tested to deliver epidermal cells *in-vitro* on cell culture plates, using a pump

aerosol nozzle (66,78). Direct cell-spraying proved to be successful in consistently delivering a uniform distribution of the cellular suspension, promote cell proliferation a few days after spraying and stabilize cells when delivered with fibrin gel (78). As a result, cell spraying was later adopted for clinical settings such as the liver and heart, as well as animal eyes (66,70) (with high cells viability rates of up to 90%) (67,79). However, a standardised protocol for cell-spraying into the eye needs to be established and should be applicable to individual patient anatomy and geometry. Since then, various researchers adopted different experimental techniques varying from in-house built experimental setups to commercially available spray systems (79), and we go on to describe their strengths and weaknesses next.

Aerosol technology is a promising system that has the advantage of spraying cells through evenly distributed coatings (67). By using the aerosol technology, cells are uploaded within an apparatus together with a polymer hydrogel and sprayed directly onto the region of interest. Studies carried out so far used polymer hydrogels such as fibrinogen to form the cellular suspension. Commercially available spraying applicators have integrated pressure regulators to manipulate the volume of cell delivered and promote aerosol formation. However, there are still related limitations with cell viability and ease of cell delivery (67). Studies in the literature have shown that higher pressures would increase shear and elongation stresses on the cells, therefore reducing their survival rate (67). Nevertheless, the impact on the anatomical structure following cell spraying strongly depends on the spraying distance, the pressure applied at the injector and the anatomical surface area needing treatment. Air pressure, nozzle dimensions and the volume flow rate of the cellular suspension are parameters that need to be closely monitored to produce the desired spray without causing damage to tissue. Currently there is no consensus on the quantitative interdependencies of these spraying variables and outputs.

Air pressure has influence on the cellular suspension's velocity, cell survival and differentiation. A number of studies have used air pressure values either derived from the literature, instructed from commercially available applicators or by carrying out *in-vitro* and/ or animal testing (66,67,70). It is now hoped that such data will be used as a platform to implement cell-spraying to more anatomically relevant human structures, specifically smaller organs such as the eye. To the best of our knowledge, a standardised method on how to derive organ-specific parameters by reducing costs, number of experiments and time is yet to be developed. Therefore, further investigations are needed to achieve this. Through this thesis we intend to develop a technique that would help determine parameters such as external pressure and volume flow rates for specific clinical applications.

On this basis, there exist outstanding questions to develop cutting-edge spray systems that would allow application in different parts of the body, whilst promoting cell viability and survival leading to a successful tissue regeneration. We strongly believe these application-specific parameters could be addressed through computational approaches that would replicate realistic surgical problems, and ultimately develop subject-specific mathematical models. Mathematical modelling can be used as a tool to accelerate the design of spray systems to promote the application of cell-based therapies in different medical settings. This will be discussed further in later chapters. This could be achieved by creating a virtual platform for a specific clinical application, defining key parameters (such as air pressure values and volume flow rates previously used in the literature) and predicting how the cellular suspension would behave on the damaged tissue. These key parameters will be validated by replicating the settings from the mathematical modelling through a series of experiments. In this thesis, we propose such a multidisciplinary approach for spraying cells onto the retina.

Spray systems have been developed and applied successfully in other industries such as agricultural application, consumer products, medical

treatment of respiratory diseases, fuel injection systems and other combustion applications (80). Implementing mathematical modelling and related theories in cell-based therapies, is an opportunity to capitalise on such technology within medical applications. Several spray systems have been developed over decades. Those that reached approval for clinical applications, are limited to a small number of medical settings, thus introducing the need of an improved design with ease of manipulation of key parameters and applicable to a wider number of degenerated organs. This approach will be examined to look at delivery of therapeutic stem cells to the retina.

Next, in order to better understand the aerosolization process during a spraying event, the theory of aerosolization is presented, followed by the evolution of spray systems and their applications in medical settings.

2.4. Theory of aerosolization

Converting liquids into sprays is of importance in several applications and fields such as agriculture, meteorology and medicine (65). Over the years, several spray devices have been designed as atomizers or nozzles; sprays can be produced in different ways. During the atomization process, a liquid may be dispersed though the liquid's kinetic energy, exposure to high velocity air or gas, or by mechanical energy applied through an external device. The process of atomization is a random process, which is characterised by a wide range of droplets size.

Droplet size distribution as function of time, density of the fluid and droplets velocity are all affected by the properties of the gas, the liquid that the gas is dispersed into, and the internal geometry of the atomizer. The simplest spraying event takes place from a circular orifice, where the main velocity is in the axial direction, inducing a laminar flow. Turbulence in the liquid, cavitation in the nozzle and aerodynamic interactions with the surrounding air are all

contributing factors to an atomization process. Further in the downstream region, drop sizes are larger and the relative velocity is lower. To achieve the desired liquid-gas mixture, many applications are subject to conical or flat patterns.

During the process of atomization, a liquid sheet is formed through the kinetic energy of the liquid. Flat sheets are produced when liquid is forced through a small orifice through pressure or centrifugal forces; depending on the type of atomizer. The initial hydrodynamic instability of a liquid sheet is characterised by hydrodynamic disturbance; the liquid sheet breaks and expands away from the nozzle, forming threads and ligaments that vary in diameters. The large drops are subsequently divided into smaller drops, thus producing a range of drop sizes and mean diameter. The latter depends on the thickness of the fluid sheet, its relative velocity to the surrounding air, the viscosity of the liquid and the surface tension. There are also hydrodynamic forces which cause wavy-sheet disintegration within a liquid sheet. High liquid velocities are a consequence of high injection pressures, causing sheet disintegration closer to the nozzle exit.

With a typical spray including a wide range of droplet diameter, there is currently no complete theory able to fully describe the hydrodynamics and aerodynamic processes involved in sheet disintegration under normal atomization conditions. As such, empirical theories can predict mean drop sizes and drop size distribution. However, for practical applications on cell therapies it has not been determined whether one parameter has an advantage over the other. Hence, the best spraying distribution on the region of interest may depend on any given application. We now proceed in discussing atomizers and rational justifying the type of atomizer used for this thesis.

2.5. Atomizers

The function of an atomizer is to produce a spray, through a high relative velocity between the liquid to be atomized and the surrounding air. Some liquids may be discharged at high or low relative velocities. There are different types of atomization techniques (see Table 2.1) used in industry such as rotary, air-assist and airblast, ultrasonic, electrostatic and pressure atomizers. Rotary atomizers provide uniform spraying distribution and a 360° spray pattern, which is not suitable given that cell-based therapy for retinal degenerative disease will only require coverage of the retinal structure (approximately ¾ of the total surface area of the eye). Air assist atomizers can provide good atomization patter, prevent clogging and atomize highly viscous fluids; however as an external air supply is required, additional equipment will be needed which could make the overall spraying equipment too bulky to be handled manually and it is therefore better suited for industrial applications. Similarly, air-blast develop good atomization and they are simple and cheap to manufacture and can spray at low velocity; however, at expenses of generating a coarser spraying pattern. Ultrasonic atomizers cannot handle high flow rates; although there some medical sprays adopt this type of atomizers; they are more expensive to purchase. Electrostatic atomizers provide fine atomization however are mostly used on highly viscous fluids such as paints.

With pressure atomizers (which are widely used), a liquid is sprayed through a small aperture under high pressure conditions, and the pressure energy is converted into kinetic energy to develop relative velocity between the sprayed liquid and surrounding air. With pressure atomizers, external pressure and cone angle can be easily controlled computationally. They are also widely available; we know briefly discuss them.

Table 2.1 Comparison of different types of atomizers, with their characteristics and examples of applications, which will be taken into account when selecting a suitable atomization type for this thesis (Information extracted from Lefebvre (2017) (65)*.*

Type	Description	Advantages	Disadvantages	Examples of applications
Pressure atomizer	Plain orifice	– Simple, cheap – Rugged	– narrow spray angle – solid spray cone	Diesel engines; jet engine; afterburns; ramjets
	Simplex	– Simple, cheap – Widespread (up to 180°)	– high supply pressure needed – cone angle varying with pressure differential and ambient gas density	Gas turbines; industrial furnaces
	Duplex	– Same as simplex – Good atomization with various flow rates	– Spray angle narrows as liquid flow rate increases	Gas turbine combustors
	Dual orifice	– Good atomization – Relative constant spray angles	– atomization poor in transition range – complex design – vulnerability of small passages to blockage	Aircrafts and industrial gas turbines
	Spill return	– Simple construction – Good atomization overflow range – Large holes preventing risk of blockage	– spray angle varying with flow rates – higher power required with other pressure nozzles	Different types of combustor Potential for slurries and fuels of low thermal stability
	Fan spray	– Good atomizer – Narrow elliptic pattern	– High pressure needed	High-pressure coatings; annular combustors
Rotary	Spinning disk	– Nearly uniform atomization with high speeds – Independent control of atomization and flow rate	– Produce 360° spray pattern	Spray drying Crop spraying
	Rotary cup	– Handles slurries	– May need air-blast around periphery	Spray drying
Air assist	Internal mixing	– Good atomization – Prevents clogging with large passages – Atomizes highly viscous fluids	– Liquid can back up in air line – Requires additional device – External high-pressure air needed	Industrial furnaces; industrial gas turbines
	External mixing	– Same as internal – Construction prevents liquid backflow	– External source of air needed	Industrial furnaces; industrial gas turbines
Air-blast	Plain jet	– Simple, cheap – Good atomization	– Does not permit high liquid/air ratios – Narrow spry angle – Atomization performance inferior to pre-filming	Industrial gas turbines
	Pre-filming	– Good atomization – Widespread angle	– Poor atomization at low air velocities	Industrial and aircraft gas turbines
Ultrasonic		– Very fine atomizer – Sprays low velocity	– Cannot handle high flow rates	Medical sprays; humidification; spray drying; acid etching combustion
Electrostatic		– Very fine atomization	– cannot handle high flow rates	Paint spraying; printing

2.5.1. Pressure atomizers

As previously mentioned, pressure atomizers convert pressure to kinetic energy, to generate a high relative velocity between the liquid and surrounding air. These include plain orifice, complex nozzles and variable nozzle geometries. Plain orifices have a simple circular design, which is used to eject the liquid. The finest atomization is achieved at smaller orifice size; for liquids with low viscosity, the liquid passes through a small circular orifice. If an external air pressure is applied at the same outlet where the liquid is discharged exceeds 150 kPa above the atmospheric pressure, a high jet velocity is formed disintegrating the liquid into droplets, thus increasing the turbulence in the liquid and aerodynamic drag forces. The outer cone angle of sprays produced by plan-orifice atomizers is between 5° and 15° (presumably mainly determined on the desired output of the spraying process), which is mainly affected by the viscosity and surface tension of the sprayed liquid. The size of the cone angle is also known to be slightly affected by the ratio between the diameter and length/diameter of the atomizer.

Examples of plain orifice atomizers include diesel injectors, which provide a pulsed intermittent supply of fuel to the combustion space and is widely researched in the literature. Commercial software such as ANSYS (Canonsburg, PA), Siemcenter STAR-CCM+ (PLM. Plano, TX) are used for predicting atomizers behaviour. However, there remains challenging in predicting the spray itself. As such, commercial software provides empirical correlations to describe atomization process. Simulations have been used to predict fuel spray penetration and trajectory within a combustion chamber, in turn assisting with engine design and comparisons with existing experimental data.

The main disadvantage of plain orifice is the narrow spray cone angles it exhibits, which will fail to cover a large surface area for most practical

applications. On the other hand, pressure swirl atomizers (also known as simplex) can generate wider cone during a spraying event. The centrifugal force creates a swirl motion on the liquid, hence spreading into a conical sheet as the liquid leaves the nozzle. The sprayed cone can be hollow or solid. In the solid cone angle, there is a uniform distribution of the droplets, whereas the hollow cone spray, most of the droplets are delivered at the outer edge of the conical spray pattern. The spray structures are illustrated in Figure 2.1. The disadvantage of solid cone nozzle is the coarse atomization at the centre of the spray, where the droplets are bigger compared to those at the periphery. Hollow cone, on the other hand provides better atomization, and several industrial processes prefer its radial liquid distribution compared to the solid cone (65).

In the pressure swirl (simplex), the sprayed liquid spreads to form a hollow conical spray, with spray angle varying between 30° to 180° depending on the application. The finest atomization is achieved at high pressures and wide spray angle. Depending on the application, a solid cone angle may be preferred and can be achieved by introducing an axial jet or ay alike device, to spray drops in the centre of the hollow conical spray. When a liquid is sprayed it goes through several stages before reaching atomization as shown in Figure 2.2. The liquid dribbles from the orifice as a thin distorted pencil. A cone forms into a closed bubble, also known as onion stage, then erupting into a hollow tulip- shaped, forming large drops and into smaller ones as the inject pressure is increased.

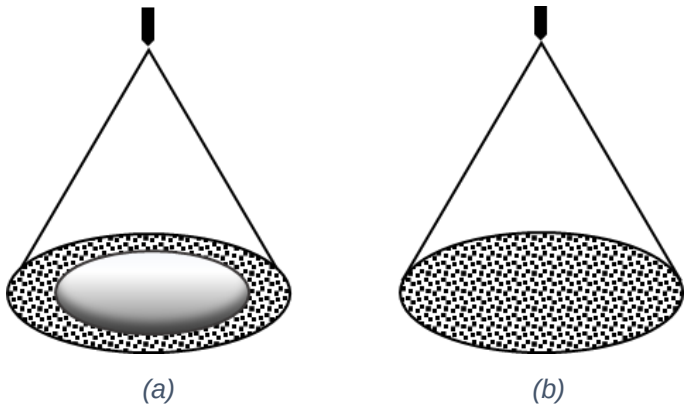

Figure 2.1 Schematic diagrams for the two types of spray pattern produced from simplex atomizers, of which circumferential patterns is dependent on the nozzle design. (a) Hollow cone: produced when most of the droplets are concentrated at the outer cone edge of the conical spray patter and (b) Solid cone: droplets are mostly uniformly distributed throughout volume of the cone pattern (65).

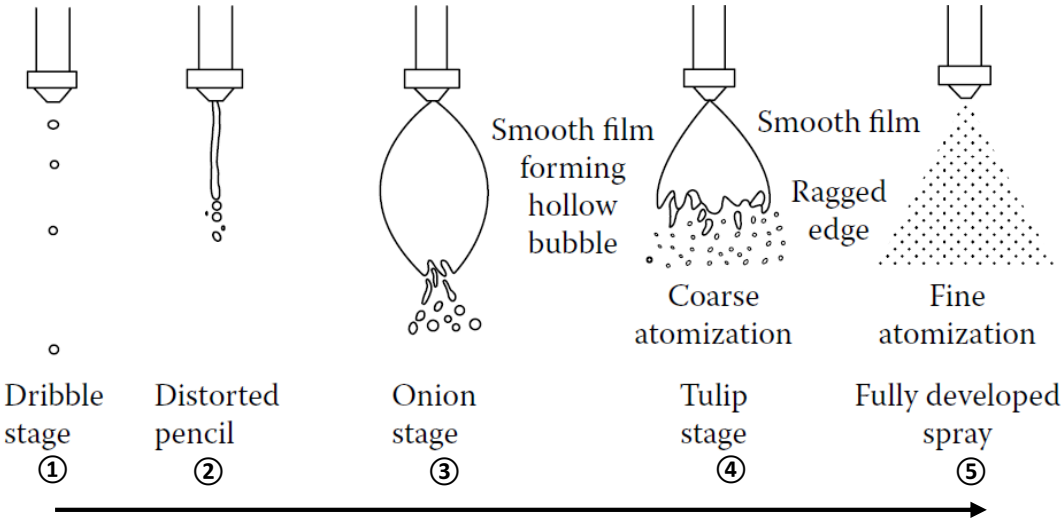

Figure 2.2 Stages of spray development as injection pressure is increased; modified from Lefebvre (2017)(65).

2.6. Basic processes of atomization

Atomization takes place following the interaction between internal and external forces of a liquid, resulting in the bulk liquid being converted into small drops. The most elementary form of atomization is the quasi-static case; this occurs when there is a slow liquid discharge from the nozzle diameter, at which stage gravity exceeds tension forces acting on the liquid and droplets form. As a result of the small discharge, the mass of a drop m_D is defined by gravitational forces g and tension forces σ, as the fluid is emitted from a circular tube with diameter d_o as:

$$m_D = \frac{\pi d_o \sigma}{g}. \tag{2.1}$$

Assuming the drops are spherical, the corresponding size of the droplets' diameter is defined by

$$D = \sqrt[3]{\left(\frac{6 d_o \sigma}{\rho_L g}\right)}. \tag{2.2}$$

It is also theoretically stated that gravitational forces are significant during formation of large droplets and can be negligible during formation of small drops. Atomization involves several interactions between a liquid and the surrounding environment (air), thus leading to droplets formation which are subject to aerodynamic pressures. The pressure distribution acting the droplets, attempt to stabilise the internal forces with the external forces through surface tension between the liquid and the liquid viscosity. During equilibrium, the internal pressure balances the external aerodynamic pressures and the surrounding tensions pressure, as such that

$$p_I = p_A + p_\sigma = constant. \tag{2.3}$$

Assuming a drop has a shape of a complete sphere, then

$$p_\sigma = \frac{4\sigma}{D}. \tag{2.4}$$

Based on the defined relationship above, a droplet maintains stability when a change to its surface pressure is balanced with a corresponding change in surface tension. However, if the aerodynamic forces are greater than the surface tension pressures, the external pressure may deform the drop and lead to further reduction of surface tension pressures. High speed photography has been able to show how droplets split when subject to aerodynamic forces, which depends on the surrounding flow pattern. Research has identified three basic kinds of deformation; lenticular, cigar-shaped and bulgy (see Figure 2.3). During lenticular deformation, the drop is flattened forming an oblate ellipsoid; the deformation is dependent on the magnitude of the internal forces causing the deformation. This type of deformation occurs when drops are subject to aerodynamic pressures or viscous stresses, which are produced by rotating and parallel flows. The ellipsoid then gets stretched into a flatter geometry, thus giving rise to smaller droplets. The cigar-shaped deformation can also break into a long cylindrical thread, in turn releasing smaller drops. Bulges are created from parent drops to form smaller ones, following irregular patterns. As a result, the choice of deformation cannot be externally controlled, as it is subject to the gas and liquid's viscosity, density and the flow pattern around a droplet.

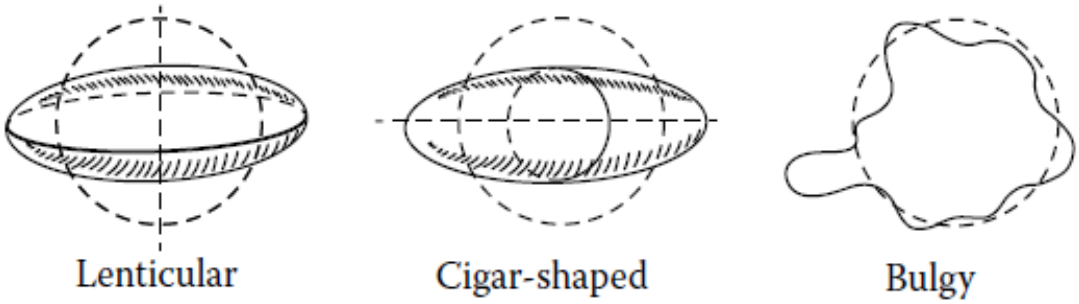

Figure 2.3 Basic type of globules formation derived by (65).*Lenticular deformation: the droplet is flattened and forms an oblate ellipsoid; this is indicated with a solid line as an elliptic shape. The subsequent deformation depends on the magnitude of internal forces that cause the deformation. Cigar shaped deformation: the initial droplet elongates into a long ligament, in turn breaking into smaller drops. Bulgy deformation: the drop surface turn into a bulge, that in turn creates smaller daughter droplets from parent droplets (65).*

To summarise, droplets breakup in a stream is characterised by dynamic pressure, surface tension and viscous forces. For liquids with low viscosity, droplets breakup is characterised primarily by ratio between inertial forces and surface tension forces. These two terms for a dimensionless number known as the Weber number (We); which is defined as the ratio of dynamic pressure to pressure as a result of surface tension. The larger the We, the greater the ratio between the external pressure forces and the deforming surface tension forces. The initial condition for breakup is determined by equating aerodynamic drag to the surface tension force, which is

$$C_D \frac{\pi D^2}{4} 0.5 \rho_A U_R^2 = \pi D \sigma. \tag{2.5}$$

Where, it compares inertial with viscous forces. This equation (2.6.5) can be rearranged, it defines the dimensionless Weber number as

$$\frac{\rho_A U_R^2 D}{\sigma} = \frac{Inertia}{Surface\ tension}; \tag{2.6}$$

Where $\rho_A U_R^2$ is the dynamic pressure and $\frac{\sigma}{D}$ the pressure as a result of surface tension. Several experimental methods have been implemented to investigate aerosolization of large droplets. It has been theoretically and experimentally proven that the breakup method of aerosolization is characterised by exposure to steady acceleration or sudden exposure to a gas stream of high velocity. With exposure to steady acceleration, droplets rapidly flatten, whilst at high velocity stream the liquid forms an almost circular rim with fragments of bubbles at the centre.

When a liquid is released from a nozzle as a continuous jet, it disintegrates into filament and drops, which interact with the surrounding air. This process in known as primary atomization. When drops are formed, and they exceed their critical diameter size, their disintegration goes into a further atomization stage, known as secondary atomization. This stage is directly related to the

breakup model. There different linear models describe liquid disruption during atomization, however all producing similar results (65,81). Each theory had different focus; from jet geometry and jet disintegration, to jet instability and drops behaviour when subject to low velocities. The latter is derived from Rayleigh's analysis, which simplifies the liquid as a long inviscid column and neglects influences from the gas phase (81). The literature (65) identifies four methods of drop formation:

1. The Rayleigh mechanism, which consist of drop formation without air friction. The symmetrical waves are formed following interactions between primary disturbances in the liquid and surface tension forces. This method outlines a linear relationship between the jet length before breakup and the jet velocity (Figure 2.4a). According to Weber's theory, there is a linear relationship between the length of the jet before the breakup and the jet velocity.
2. Drop formation through influence with air, the jet velocity increases, and the aerodynamic forces cannot be neglected (see Figure 2.4b).
3. This regime develops a sinuous jet oscillation and reduce the influences of surface tension (see Figure 2.4c).
4. Chaotic and irregular liquid break at the nozzle, causing full jet discretization.

Spray based systems have been in existence for almost a century. A review on their evolution is presented in section 2.7.

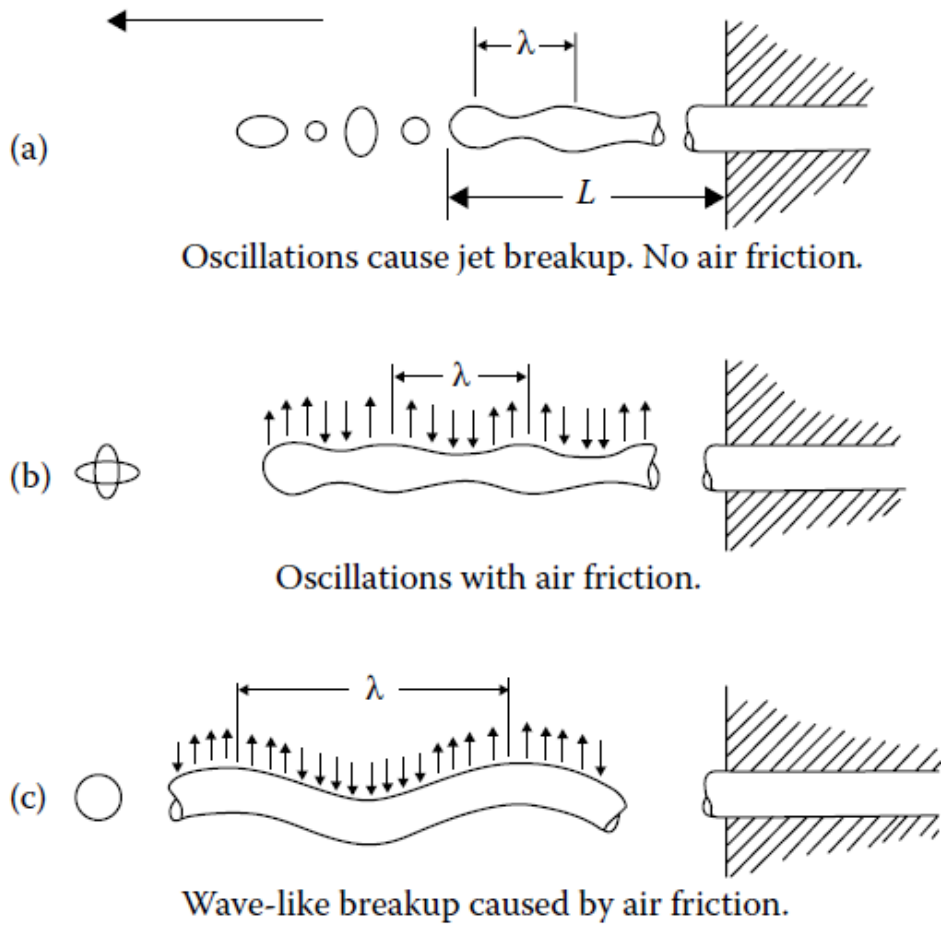

Figure 2.4 Drop formation mechanism (65).*(a) Drop formation without air influence, showing a radially symmetrical wave following interactions between the liquid surface tension forces and disturbances in the liquid. (b) Drop formation with friction and aerodynamic forces cannot be neglected as jet velocity increases. (c) Breakup caused by air frictions as aerodynamic forces increase* (65).

2.7. The evolution of spray-based systems for application in industry and medicine

The spray applicators identified in this review are extracted from the patent literature and summarised in Figure 2.5. This section is grouped according to the principles by which the designs operate. The design concepts were developed for several applications such as gastrointestinal bleeding, cutaneous application, insulin injection, dental procedures and for male and female genital tracts. The overlap with spraying concepts for household and industrial applications are also discussed when appropriate. The following chart summarises the spray applicators developed, their key features and clinical applications where they have been implemented.

Concepts' sketch	Year of release and main features	Clinical application (where relevant)
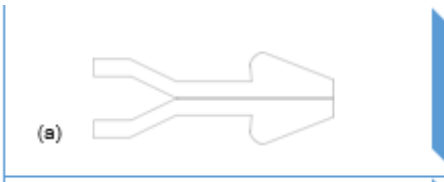 (a)	1938 • Duplex arrangement • Mixing chamber • Dual syringe • Bifurcated tubes • Three outlet walls	Medicinal administration to male and female genital tracts (82)
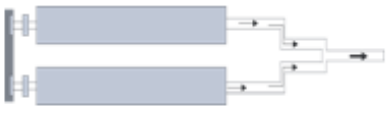 (b)	1982 • One-way syringe bodies and plungers • Single hand operation • Easily changed and sterillized equipment • Standardised needle	Ophthalmic (70)
 (c)	1986 • Sequential or simultaneous injection • Standardised so that syringes with two barrels, each with a plunger • manually operative rotary three point valve (controlling outflow movement)	
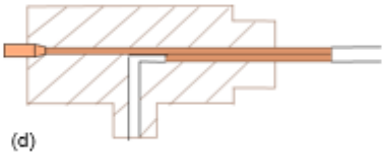 (d)	1986 • For large areas of applications only • multilumen catheter introduced	
 (e)	1988 • Different cross-sectional area vial chambers • Floating piston inbetween the chambers to separate components	
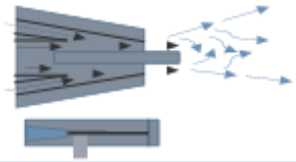 (f)	1989 • Easy to grip • Can be manipulated at various orientations • Needles packaged as part of apparatus assembly • Syringe bodies held in parallel through clamp	
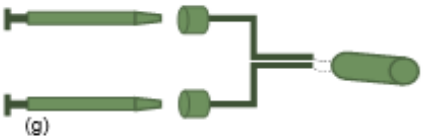 (g)	1990 • Dual cannula delivery head • Lock fitting from manifold component	
 (h)	1994 • Syringes with different orifice size (to be used for two different components of biomaterial)	

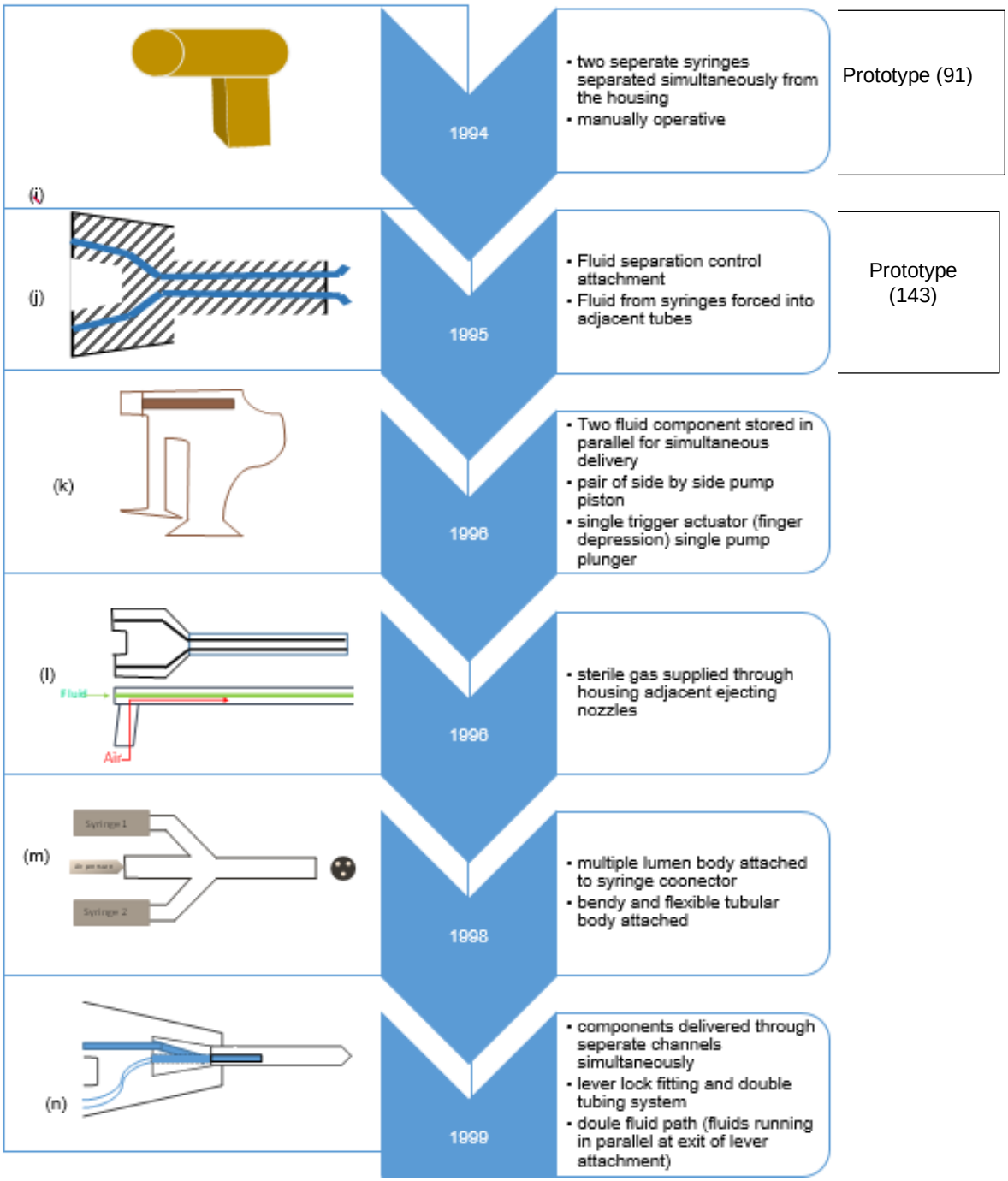

Figure 2.5 Spray applicators developed and respective key features with respective clinical application recorded in the literature. Some of the features developed are not limited to dual syringe (a), single hand operation, closely representing the Baxter Easyspray system used in this thesis (b), manually operative valve (c), application for large areas (d), vials with different cross-sectional area (e), ease of manipulation at various orientations (f), dual cannula delivery head (g), syringes with different orifice size (h), pistol grip (j), fluid components stored in parallel (k), introduced housing for gas supply (l), multiple lumen body attachment (m) and components delivery through separate channels (n).

The evolution of spray systems summarised in Figure 2.5, will be referred to throughout the next section. The main design features are the dual syringe concept, a cannula head, pistol grips (in some rare cases) and the introduction of external air pressure. The dual syringe and dual cannula head concepts were introduced to facilitate multiple fluid delivery and simultaneous mixing. The occasional pistol grip approach and the introduction of external air pressure to facilitate fluid delivery will be discussed below.

2.7.1. Dual syringe and dual cannula delivery head

The very first dual-syringe (Figure 2.5a), relates to an apparatus used for delivering biological compounds within human natural cavities , such as male and female genital tracts (82). The apparatus consists of two cylinders acting as reservoir for the two different fluids to be mixed, and a connecting chamber where the mixing takes place just before delivery within the cavity. Plungers were introduced in subsequent designs to facilitate the single hand operation of the one-way syringe bodies (Figure 2.5b). The dual syringe concept has been used to date by various commercially available devices such as the Easyspray System (Baxter Healthcare), which will be discussed later.

A similar design is maintained for a single hand apparatus for simultaneous application of hydrogel components, yet benefitting from the dual syringe mechanism (83). It differed from previous designs where the vials had different cross-sectional areas and were connected through a collecting point, where the mixing takes place (Figure 2.5b). This design helped to overcome premature hardening, which was encountered in previous designs, when delivering highly viscous substances (84). Premature hardening does not work in favour of cell delivery, as it would act as a barrier to cell proliferation.

However, this apparatus could not be gripped comfortably in a variety of orientations, therefore making manipulation difficult. In addition, the needle became blocked and had to be replaced from time to time, whilst surgical procedures were being carried out. Thus, to control the volume of fluid delivered, a second inlet to pump a sterile gas such as compressed air was introduced. This enabled reliable mixing taking place before reaching the area of application. The method appeared to be more economical, as it helped controlling the volume of the fluid to be applied.

Another design concept was motivated by sequential and parallel delivery, inspired by insulin administration for diabetic patients (Figure 2.5c) (85). The novelty of this patent lays on the manually operated three position rotatory valve, introduced to control the filling of the syringe and outflow movement of the liquid. Increasing the pressure of the medicinal gas affected the atomisation phase of the fluid at the tip of the mixing needle or at the mouth of the catheter lumen (86). The benefit of this arrangement was that the apparatus could also be used for small areas of application. Although this could be the ideal concept as the spraying would be applied on different organs, to the best of our knowledge, there are no recorded information from the literature with regards to spraying parameters being met through this specific apparatus.

An additional component was introduced to prevent clogging (Figure 2.5d); however it only appeared suitable for application on large areas and not for microsurgeries (87) . Packaging of needles for assembling the apparatus was also introduced. The syringe bodies were held in parallel through a clamp, specifically designed to help the surgeon use the apparatus in various orientations and facilitate a single handle application (Figure 2.5f). To prevent blockages, the tip of each syringe was attached to an adapter head, in turn connected to separate needles. The needles were then bent so that they had elongated sections parallel to each other, to promote simultaneous delivery

and potentially avoid premature hardening. Despite this feature, to the best of our knowledge, the design is yet to be applied to any real clinical application.

Another unique feature was the plastic connector having two semi-cylindrical channels (Figure 2.5f), which were used to hold the syringes in place. This facilitated gripping the device in between the fingers, and eased operation for spraying in different orientations. In this way, the hydrogel components are kept parallel to each other, until reaching the site of application. By using a unique needle design to prevent clogging, this invention was followed by using a dual cannula delivery head.

The dual cannula delivery head appeared to be an important feature to facilitate simultaneous multiple fluid delivery (Figure 2.5g). The multichannel head is a requisite incorporated in the dual cannula for a dual syringe applicator system (80). Several multichannel head designs were developed; some with (Figure 2.5l) and some without air channels (Figure 2.5i). The delivery head with the air channels support the spraying of the hydrogel onto the injured area. The air channel was positioned in parallel with the delivery channels of hydrogel components (Figure 2.5m), hence facilitating fluid delivery and covering a larger surface area. In a design introduced by Zimmermann (88), the gas channel was divided with a separating web into a multichannel. When the hydrogel was sprayed, a spray cone was created, promoting uniform mixing of the hydrogel components and accurate spraying dependent on spraying distance and pressure applied (88).

A dual cannula delivery head design provided the advantage of lock fitting from the manifold component, through the syringes to the hollow needle, to promote simultaneous delivery of hydrogel components (89) and avoid careless separation of the parts during a surgical procedure (Figure 2.5n). The simultaneous and separate delivery of the a biopolymer was introduce to prevent blockage, but showed little success (90). With simultaneous delivery,

certain designs lacked the appropriate fitting of the delivery tubes and they appeared to be difficult to manipulate with one hand. Another method of delivery using a similar design introduced an offset position of the syringes with a plunger holding them in place to prevent any longitudinal movement.

A new method of delivery was introduced as a better alternative to prevent mixing taking place within the system that allows rapid and complete mixing of the solution. This arrangement was introduced to facilitate dispensing more viscous fluid components such as fibrin glue. This method involved delivering the components separately whilst supporting the atomisation process. In this way, there was no blockage within the nozzle or the needle. This design was beneficial by acknowledging that the nozzle size will affect the spraying pattern generated. A connecting head with different orifice sizes was attached to the tip of the syringes (Figure 2.5 h).

2.7.2. Pistol grips

Pistol grips are employed to store sets of fluids that would be mixed prior to use, such as adhesives and glue. The pistol grip design by Holm (91), was described as a dispensing device for at least two fluids stored in a piston-like housing where a spring-like trigger was used (Figure 2.5i). An advantage of this device was the low manufacturing costs involved, thus promoting an affordable delivery system. This innovation promoted an improved homogeneous spraying that allowed control over the volume of fluid delivered in one application. Another advantage was that the thumb pressure was not adopted in most of the dual syringe applicators and dual channel delivery head systems. Subsequently, pistol grips and gun-type designs were developed to assist with fibrin glue delivery. As such device required the syringes to be operated at the same time, the disadvantage of this design was the greater frictional force arising from the applicator's gun-type trigger, making the design difficult to operate with one hand and not suitable for medical applications

involving small anatomical structures. However, this design is yet to be applied to medical application as it is more suitable for industrial and household products. This is due to associated increase in manufacturing time and cost, and unsuitable size for clinical settings. A variation of Holm's patent (91) introduced the use of compressed gas to create an atomisation spray. Similarly, to previous designs, the use of two syringes was still required to act as reservoirs.

2.7.3. Dual channel pump sprays

Additional applicators were later developed, aimed towards household products such as cleaning agents and starches, which allowed the storage and delivery of multiple fluids (80). A similar concept was later adopted where the design consisted of the vials being placed directly in the applicator (Figure 2.5k), without the use of needles for manual transfer (92). Although, dual channel pumps were further developed for several products to promote low manufacturing costs and control the volume of the fluid sprayed, there are still disadvantages associated with the complexity of the applicator, which would be difficult to use with fluids of high viscosity. There are also high costs associated with supply chains set up to fabricate the number of small parts involved in assembling a spray device. Such sprays are assembled by robotic factories, therefore would demand very high costs to manufacture similar products.

2.7.4. Gas driven applicators

An advantage of adopting gas driven applicators, is their ability to provide a homogeneous fluid distribution, by spraying cells on a layer-by-layer basis to accelerate healing (66). The benefits identified in these spraying designs developed over the years, lead to the development of the spray system from Baxter Healthcare, which has been used in several animal studies (67,70) and

will be used as a starting point in this thesis for a potential cell-based therapy to treat retinal diseases such as glaucoma. Details will be discussed later in Chapter.

Some spray designs were developed based on mathematical approaches that reduce the amount of pressure required, by releasing compressed gas through narrow orifices. A unique design consisted of a portable dual-channel applicator, which had no moving components. The system is initiated by opening the trigger's air valve, which would eventually expel the hydrogel components from two separate tubes, mixing together at the site of application. Other applicators used a combination of gas and vacuum and manual force to start the system. A specific innovation adopted the use of two syringe-like reservoir. Nevertheless, there are still problems associated with internal blockage, hydrogel wastage and incompatibility with the nature of surgical procedures, perhaps owing to the nozzle dimension and the viscous nature of the biomaterial.

Based on the various spray systems developed over the years, the most prevalent problem was blockage of the needle with substances. This has led to further development of systems with less moving parts (hence facilitating fluid delivery that provide stability during surgical procedures), introducing homogenous fluid mixing prior to delivery and homogenous fluid coating. To determine whether a computational approach will help overcome the above questions and develop organ-specific parameters such as required volume flow of the cell suspension and the external air pressure at the injector, we analyse a potential treatment for glaucoma. We will now start by describing the spraying device used for the animal study in section 2.9 and in other studies (67,70). We also intend to use the same equipment during the experimental analysis (see chapter 5).

2.7.5. Baxter Healthcare Easyspray System™

The Easyspray System developed by Baxter Healthcare Corporation USA, is readily available in the market and closely represents the setup in Figure 2.5(b), where the design promotes simultaneous delivery of multiple fluid components, mixing the components prior to reaching a desired sight, ease of manipulation through single hand application and integrating external air pressure to create aerosolization effects.

This system is made of the following components: a joining piece, a DUPLOJECT plunger and a DUPLOJECT two syringe clip (see Figure 2.6). Two syringes are loaded with fibrin glue components: the sealer protein and thrombin solution. The syringes are then fixed into the DUPLOJECT two-syringe clip, which holds them in place and allows thumb pressure to be applied simultaneously by holding both syringe plungers together. There is also a safety strap provided on the joining piece itself, to fully constrain the syringes and prevent disassembly and leaking during spraying. The joining piece connects the application needle to the remaining apparatus, which varies in size depending on the volume of the spraying to be applied (see Figure 2.6 and schematic overview in Figure 2.7).

The external pressure regulator is attached at the bottom of the joining piece, with pressures applied ranging between 0 and 2 bars. As the diameter of a human eye can range between 2.3-2.6 cm (93), it was recommended from the host lab that an ideal spraying should cover a distance to be less or equal to 2 cm.

Using the current setup of the Baxter system as a reference point, with a simplified version of a potential surgical setup (Figure 2.7) it is hoped to eventually derive ranges of pressure, volume and flow rates suitable for the human eye, which varies from the animal models dimension and can be

potentially applied to the human eye. Such a device could potentially be used for cell delivery through robotic surgery and microsurgical technique in the retina; which has been widely reviewed over the past decade (94) as discussed in next section. If combing robotic surgery with the mathematical modelling technique devised in this thesis, aerosol spraying parameters could be closely monitored and tuned according to patient-specific eye geometry and introduce accuracy for cell delivery.

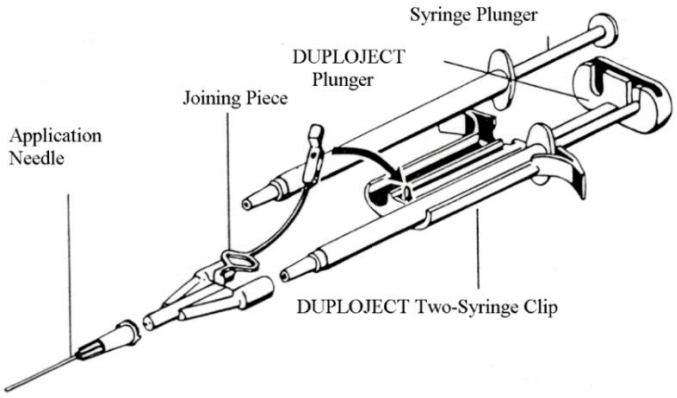

(a)

(b)

Figure 2.6 (a) Baxter Easyspray set components and (b) different needles used for different clinical applications (95,96).

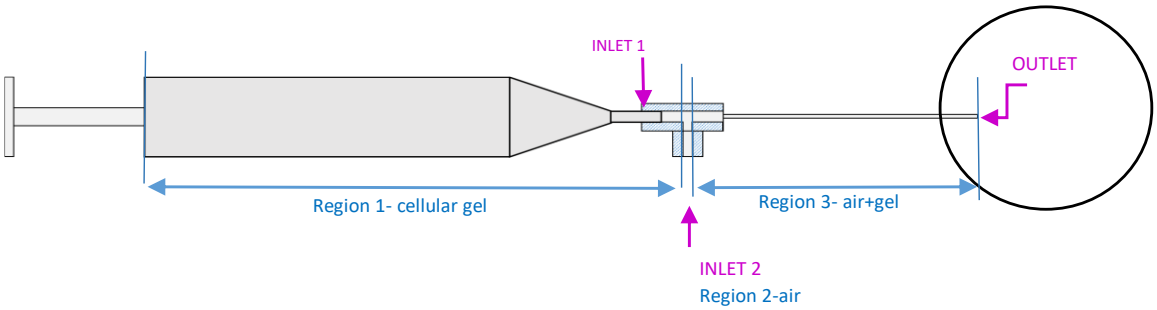

Figure 2.7 Two dimensional schematic diagram for the Easyspray System shown in Figure 2.6, comprising of the dual syringe system, showing secondary inlet for external air pressure and needle through which the cell-laden hydrogel will be sprayed through.

2.8. Microsurgery in the retina

Robotics has been widely used in surgery for several years in various disciplines such as gynaecology, urology and cardiovascular surgery (97). Its use in ophthalmic surgery is still at its early stages due to restrictions with existing equipment, such as ease of manipulation, executing seven degrees of freedom and compatibility with surgical environment. Robotic surgery would overcome some involuntary movements faced by conventional surgery, that will have a negative impact on the overall surgery; such as tremor, jerk and low- frequency drift (94); which also affect conventional microsurgery in the retina. Retinal microsurgery involves a challenging set of surgical tasks, needing miniature and sophisticated instrumentation and requires instruments which enable ease of manipulation and precision (98). During conventional vitreoretinal surgery, a cannula with a diameter of less than 1 mm is inserted through an incision made through the sclera as briefly discussed in section 2.9. The increased demand for retinal surgery over the past four decades has stimulated advances of instrumentation technology to treat conditions such as retinal detachment, macular hole and treating the epiretinal membrane. With the need for dedicated ocular robotic surgical system, these have been classified in the literature into four main categories: hand-held surgical tools, co-manipulation systems, telemanipulation systems and magnetically controlled micro-robots.

For example, the recent study by Edward et al (94), uses telemanipulation, which previously showed success through animal trials. The study integrated the first use of a remotely controlled electronic robotic device, for high precision surgery inside the eye. It provides proof of concept that general intraocular surgery can be carried out using robotic assistance. Here, a randomized double-armed clinical investigation was carried out to compare robot-assisted and manual surgery in patients needing retinal treatments. The procedures (requiring high level of accuracy and precision) were used as test models to evaluate feasibility and safety for introducing robotic assistance in

ophthalmology. If robotic assisted surgery could be used for treating retinal diseases, stem cells could be aerosolized in a controlled manner.

Through this, the surgeon is able to align the equipment accordingly, pause the operation if required and promote drug delivery onto the correct tissue plane. The tip of the cannula position was paused to control rate of drug delivery and promote safety during the procedure. Such technique could be a great advantage it incorporated for controlled delivery of stem cells into the human eye. Not only it would control spraying parameters such as volume flow rate and external air pressure for aerosolization, but also support safe cell delivery to promote cell proliferation post-aerosolization. Although the robotic assisted was more time consuming than the manual surgery, safety was used as a measure of success rather than operating speed. For example, with the robotic assisted surgery there were fewer haemorrhages and on this instance, there was no system malfunction. A manipulator used in the literature by Jensen et al (99), consisted of a computer-controlled surgery, specifically manufactured for retinal microsurgery. This equipment had the ability to align instruments precisely at the retina surface, providing six degrees of freedom.

However, with robotic surgery, precision is traded for surgical time. A disadvantage that arose through robot assisted surgery is that it was slower compared to manual surgery. For example, to align the 23 G cannula by the retinal surface from the sclera it took 2 min 26 s and it takes 12 s through manual surgery. Also, the overall surgery took 55 min through the robot and 31 min through manual surgery. However, it might be argued that the length of surgery might necessarily not be a disadvantage, if it compensates with increased cell viability and proliferation at targeted sites.

This is considered a relevant operation for treating retinal degenerative diseases such as glaucoma. The size of the retina vessel has restricted several microsurgery procedures from being performed by hand. Other

restrictive factors include the fragility of penetrating equipment needed for the procedure and limitations from manual dexterity (99). For example, when the micro pipetting is inserted for local anaesthetic delivery, it must remain within the retinal lumen for several minutes, whilst pressure inside the eye is measured. However, further research is required to identify most suitable experimental protocol and technique for stem cell delivery that will promote cell proliferation post-aerosolization. As mentioned in Section 2.7, combining mathematical modelling with robotics approaches will give a much detail insight into development of spraying devices for cell-based therapy, by promoting automating control of input n output parameters by specifically defining the desired outcome and reducing human errors during surgical procedures. Next, we explore experimental protocols that have been developed in animal eye models, and of relevance for delivery cell-based therapies to the retina.

2.9. Experimental protocol derived from animal study as benchmark to develop future procedure stem cell delivery

This thesis focuses on a recent animal study, to suggest a potential technique for stem cell delivery. This study showed that isolation and culturing of human Muller stem cells (hMSCs) have the ability to differentiate into functional RGC precursors when *in vitro* and migrated into RGC layers when transplanted *in vivo,* thus partial recovery of visual function in an experimental model of glaucoma (63). This was carried out using rodent eye models. The small vitreous volume compared to the large crystalline lens allows the cells to be delivered closely to the inner retina surface (see Figure 2.8a). However, this is not the case for the large mammalian eyes, which have a smaller crystalline lens and a greater vitreous volume compared to the rodent eye (see Figure 2.8b). This means that upon injection, cells need to travel a longer distance. With feline eyes having a similar anatomical structure to that of human eyes (see Figure 2.8c), a recent experimental method was developed at the Institute

of Ophthalmology to deliver therapeutic stem cells to the inner retina (5). We therefore hope to use this experiment setup as a platform to upscale cell-spraying from animal models to humans.

The procedure involved carrying out a complete posterior vitrectomy prior to delivering the cellular scaffold to the inner retina, thus preventing the fluid inside the eye, known as vitreous humour, to act as a barrier. Vitrectomy is a surgical procedure where the vitreous humour is removed from the eye. Three scleral incisions were made using a 20-gauge (20G) cannula on either side of the sclera to supply pressurized air and deliver the cellular scaffold (Figure 2.9). Subsequent procedures involved fluid-air exchange to maintain the intraocular pressure; and attachment of a cellular scaffold made of collagen and retinal cells on the inner surface of the retina.

Vitrectomy is performed in cats (see Figure 2.9 and Figure 2.10) as the eye model has a larger vitreous volume compared to rats' eye models, where no vitrectomy was needed. Therefore, following this animal method as benchmark procedure, the prospective cell therapy will involve cell aerosolization onto the retina surface after vitrectomy. During the aerosolization process, the cellular scaffold combines with the external air pressure, forming a multiphase flow. To predict and understand the behaviour of the sprayed mixture, we will now look closely at the mathematical theories that may be used to describe such a multiphase flow.

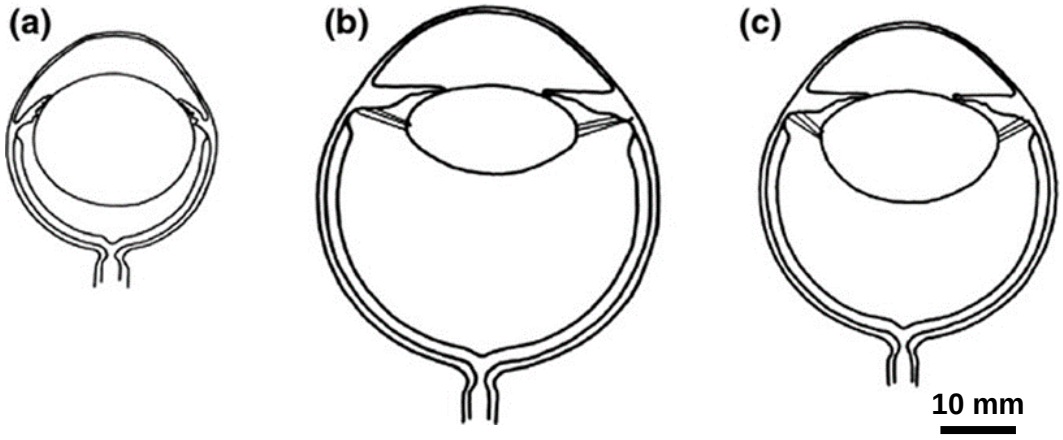

Figure 2.8 Schematic diagram comparing sizes of lens and vitreous of (a) a small rodent with a mean axial length of 6.9 mm, (b) a human eye with mean axial length of 23.9 mm and (c) a feline eye with mean axial length of 20.9 mm. It is clearly illustrated the small rodent eye has a large lens and smaller volume of vitreous humour. The human eye on the other hand, as a larger volume of vitreous humour and a smaller lens, which surgical access to the vitreous cavity more challenging (5).

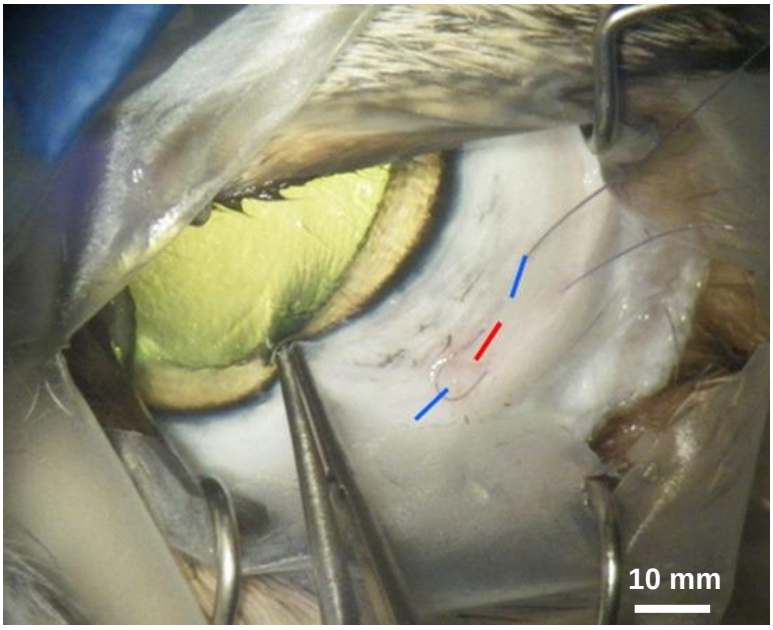

Figure 2.9 Incisions made on the cat's sclera, shown through the blue lines and the red line (5).

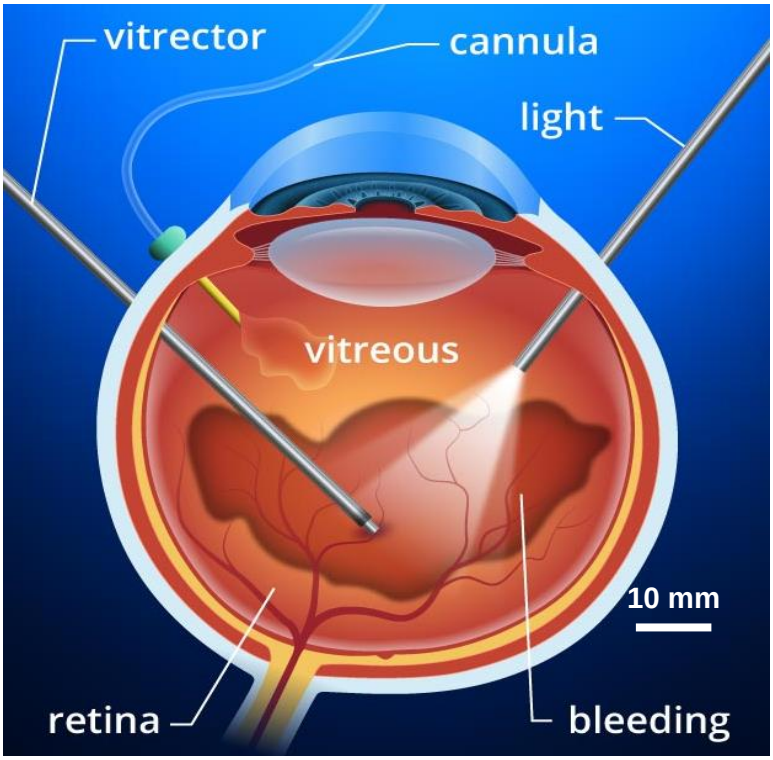

Figure 2.10 Human eye illustrating the vitrectomy procedure carried out. The cannula and the vitrector is used to extract the vitreous humour (100)

2.9.1. Modelling the multiphase flow

Based on the experiment described in section 2.9, we focus on delivering a cellular scaffold onto the inner human retina following vitrectomy, which consists of removal of the vitreous humour from the eye (Figure 2.11). In this thesis, the set up for the potential human therapy will include the Baxter spraying system as a tool for carrying the cellular suspension inside the vials, connected to an external pressure regulator pumping gas into the eye to ease cell delivery through aerosolization (see Figure 2.7). The setup for the dual syringe system equipment is simplified to a 2D model, with the assumption that hydrogel components to make the cell-based scaffold have been mixed). Further details on the selected hydrogel for cell delivery will be discussed in Chapter 3. We present the mathematical theories applicable to the such multiphase spraying systems, with the provision of the specific mathematical model and computational model detailed in Chapter 4.

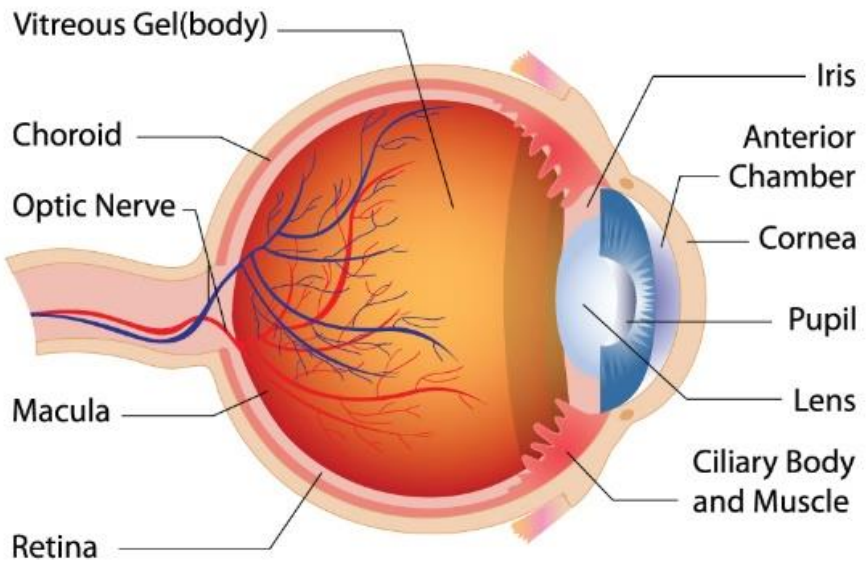

Figure 2.11 Anatomy of the human eye with a typical average diameter of 25 mm, showing the location of the vitreous fluid, covering ¾ of the human eye's volume (101).

To study the spatial distribution and the behaviour of cellular suspension droplets sprayed onto the inner surface of the eye, we will use Computational Fluid Dynamics (CFD). The use of the CFD solver Simcenter STAR-CCM+ will enable spatial simulation of aerosol spraying into the human eye, using real measurements of the eye (102,103). Simcenter STAR-CCM+ is an integrated comprehensive engineering simulation package (104), with high capabilities in addressing multi-physics problems and complex geometries. Mathematical theories are used to describe the behaviour of the cellular mixture at different stages of the apparatus set up.

The cellular suspension is composed of neural stem cells and fibrin-based hydrogel, a biodegradable biomaterial acting as a scaffold by holding the cells in place. As the cellular suspension is displaced from the syringe vials (through the nozzle into the eye), a spray is generated and the droplets path is bounded within a cone-like region, which generates upon the fluid-gas interaction at the nozzle and is directed towards the target region (105). Once the cellular mixture encounters air, they both interact with one another through displacement and interphase momentum and aerosolization.

The cellular scaffold is described mathematically as a multiphase flow. A multiphase flow is a flow where multiple phases interact within the same system. Examples include liquid-fuelled combustors, chemical reactors and sprays. Multiphase flows can be categorised into dispersed flows such as bubbles and droplets, and stratified flows such as free surface flows (104). In this research, we are working with droplets. In this thesis, we consider a multiphase flow consisting of a dispersed phase which describes the cellular suspension, and a continuous phase describing the air. Full details of the mathematical and computational descriptions, and geometry, will be provided in Chapter 4.

2.10. Summary

With the increased demand for cell-based therapies to treat chronic diseases, cell-spraying is identified as a promising technique offering direct and rapid application of stem cells onto the diseased anatomy. With the historic success of this procedure for treatment of cutaneous wounds and burns, cell spraying applications are now being explored to treat degenerative retinal diseases such as glaucoma. There are existing limitations associated with practicality in delivering these cells onto the large retina surface. Theories of aerosolization are therefore used to analyse and predict the potential behaviour of the cellular suspension once sprayed. Additionally, key features for future spraying applicators are identified by reviewing evolutions of spray systems used in medicine and for industrial applications. For example, a key feature such as integrating a dual syringe concept for application of prospective cell-based therapies, is justified due to the potential viscous nature of the biomaterial that may be used as a cell delivery vehicle. The mechanical properties of possible hydrogels to be used as a delivery vehicle will be identified in Chapter 3. In order to derive surgery specific parameters, the setup from an existing protocol from an animal study (involving intraocular vitreous removal) is used as benchmark for future development and for hopefully introducing simultaneous spraying of cells with hydrogel. However, due to geometric variabilities between rats and adult human eyes, the existing protocol from the animal study does not provide spraying parameters suitable for human eye. As such, parameters relative to human eye geometries and will be derived in the forthcoming Chapters.

2.11. Research Objectives

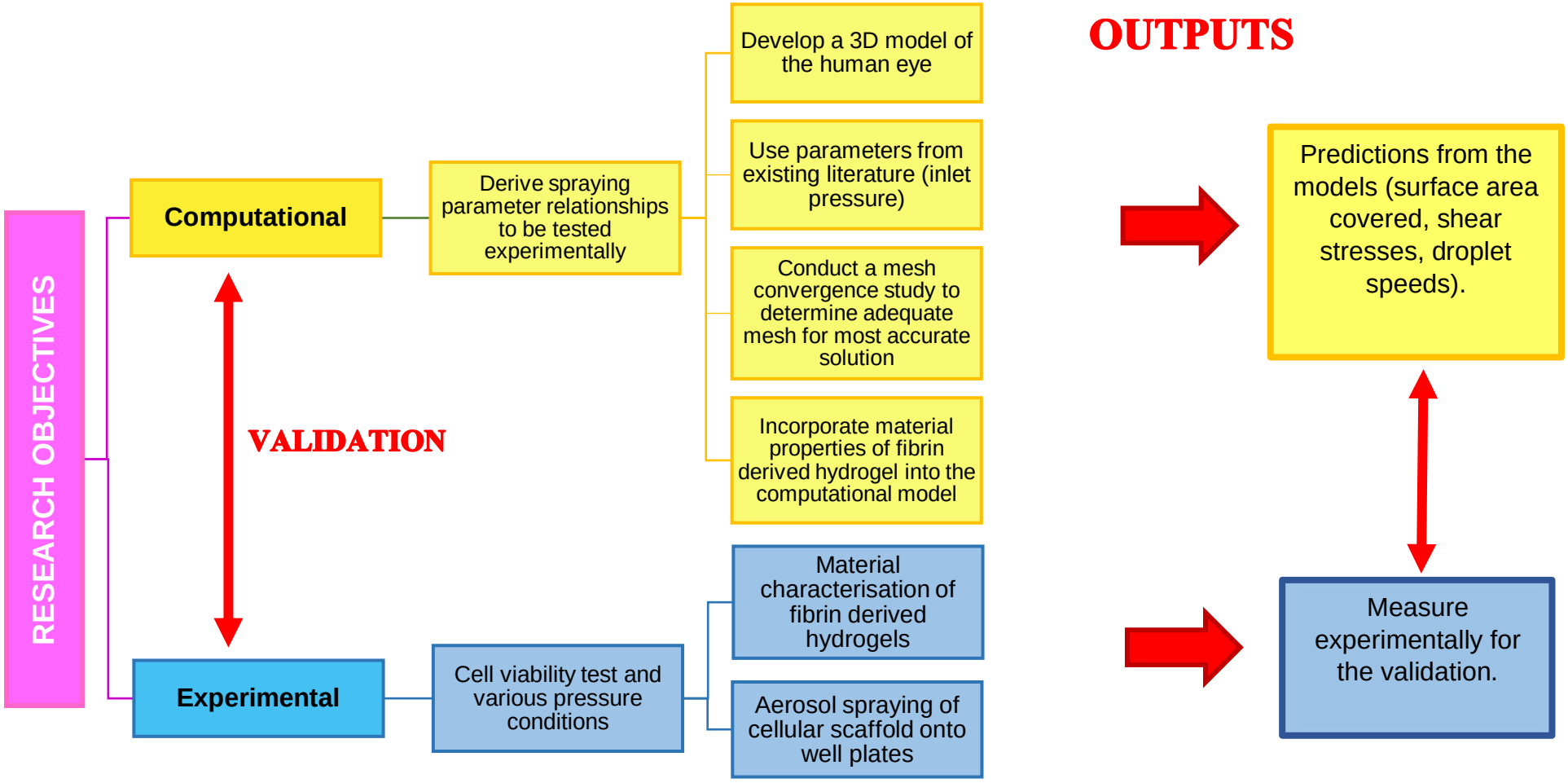

Figure 2.12 Computational and experimental objectives for this research.

The objectives for this research are divided into two interlinked categories; computational and experimental. The experimental work includes characterising rheological properties of the fibrin-derived hydrogels (see Chapter 3), to provide parameters which are then imported into the 3D computational model of the eye, (Chapter 4). The computational section starts with the development of a 3D computational model for the human eye using dimensions from the literature. Human eye dimensions vary from patient to patient; however, we use average values from published data. It is hoped the model will also be used as benchmark for testing several patient-specific eye dimensions and spraying parameters in the future. Model predictions are tested through further experimental analyses (for example, by validating the surface area spraying for a range of spraying parameters).

Ultimately, the computational models are used to define spraying parameters, which will be used for future designs of spraying systems for treating retinal diseases. The use of mathematical modelling in deriving organ specific spraying parameters and as tool for advancing cell-based therapies are finally discussed. It is hoped that we would eventually introduce a computerised system to facilitate parameter control. This may hold a greater advantage compared to a manual one (such as the Baxter system), by providing more accuracy and reliability on the required air pressure for aerosolization and volume flow rate for the cellular suspension.

The success of using of mathematical modelling for advancing cell-based therapies, could hopefully introduce development of a virtual computational model that will allow to control parameters such as volume flow rate, nozzle diameter, external air pressure; and assess how established relationships among these parameters may affect spraying outputs such as retinal surface area covered, thickness of cellular scaffold at the retina and wall shear stress at retinal wall upon spraying impact. For example, changing the geometry of the nozzle will equally impact other spraying outputs such as droplets velocity

magnitude, droplets mean dimension at the retinal wall and film thickness of the cellular suspension. Although in this research we do not focus on varying the geometry of the nozzle, if we develop a model that allows interchangeable nozzles to be used, it is believed the same approach may be implemented for other clinical applications and hopefully integrate microsurgery techniques in the future for cell spraying, which will be validated with further *in vitro* and *in vivo* studies. This thesis firstly starts with material characterisation for the chosen hydrogel to facilitate cell delivery.

3. Experimental Characterisation of Material Properties of Hydrogel Scaffolds

This Chapter presents different biomaterials used in ophthalmology and identifies fibrin-derived hydrogels as the most suitable candidate for cell-based scaffold therapies. This is due to advantages associated with natural hydrogels, such as reduced toxicity, ease of injectability and application when using a syringe, biodegradability and ability to hold cells in structure until delivered to the targeted site. Rheological testing for the fibrin-derived gels are conducted to identify behaviours and parameters, which are subsequent inputs into the computational models.

3.1. Biomaterials in ophthalmology

Biomaterials are defined as substances with natural or synthetic origin, which assist in treating, enhancing or replacing tissues, organs or functions of the body (106). They are generally applied as adhesives, sealants, haemostatic agents, regenerative scaffolds for wound healing and for drug delivery (107). Extensive advances into biomaterials for medical applications have enabled a variety of interventions and treatments, as varied as heart bypass surgery, anaesthetic administration, intravenous drug delivery and blood transfusion. Extensive research on biomaterials have improved their applications for ophthalmic surgery by considering features such as biocompatibility, biodegradation, host tissue response and transparency. Ophthalmology has a successful history of conventional biomaterials applications including viscoelastic polymers, drug delivery vehicles, contact lenses and a variety of implants (108). Their various properties make them potential candidates for cellular scaffolds to support with structural organisation.

Ophthalmic biomaterials can be synthetic or natural. Synthetic polymers such as poly (lactic-co-glycolic acid) PLGA and poly (ethylene-glycol) PEG possess high biocompatibility and biodegradable properties; they have been widely investigated for their role towards retinal cell transplantation. If a biomaterial degrades too fast, a fraction of its strength could be lost as such that the delivered cells separate prematurely and the attachment onto the damaged

tissue fails. If they degrade too slowly, it could interfere with the regeneration process. For example, PLGA has supported human embryonic stem cells (hES) cells in neural differentiation to promote cell survival when transplanted onto the retina (109). Other synthetic biomaterials used in ophthalmology are cyanoacrylates. These are widely used in ophthalmic surgery; however, as they induce inflammation, they can only be applied externally, and they are therefore unsuitable for *in-vitro* and *in-vivo* applications into the neural retina.

Natural biomaterials are viscoelastic, whereby they can exhibit nonlinear mechanical properties, which are vital for their biological functions. Biomaterials can degrade at an appropriate rate once applied onto the injured area. In this type of system, the regeneration process of the cells controls the biodegradation, also known as biofeedback-controlled degradation (see Table 3.1). During a normal wound healing process, when cells arrive onto the damaged area, they breakdown the provisional matrix (107). Some of the natural biomaterials (such as fibrin) undergo this degradation mechanism because of normal enzymatic processes. The most common natural scaffolds used for transplantation are derived from proteins and polysaccharides found in the extracellular matrix (ECM). ECM is a complex environment playing a vital role in providing tissue-specific biophysical, biochemical and mechanical properties (110). These properties, in turn influence the design requirement of a biomaterial for their respective clinical usage, as illustrated in Table 3.1. ECM provides a niche environment for stem cell proliferation, self-renewal and maintenance. These derived materials include collagen, gelatine, fibrin and hyaluronic acid (HA).

Biomaterials are being investigated for their use in retinal application for tissue engineering and for cell delivery. They could potentially be used as vehicle for stem cell delivery and hopefully retina reconstruction. A promising candidate for retinal scaffold would need to provide flexibility and facilitate intraocular penetration using minimally invasive surgery as proposed in Section 2.9, whilst also being amenable to surgical manipulation (see Section 2.1, where we

outline specific spraying parameters, geometry parameters and desired output from aerosolization). For a scaffold for cell delivery, the interactions between the scaffold and stem cells need to be considered. Currently there is no biomaterial that has all the optical properties required for designing a cellular scaffold for cell transplantation. Thus, a combination of biomaterials may need to be considered. When adopting such a combination, the mechanical properties, the controlled degradation, setting time and viscosity are manipulated by varying the chemical composition of the biomaterial, to eventually develop a suitable biomaterial to help cellular attachment onto the retina. The mechanical properties of the hydrogel may impact cell outcomes, for example the study by Engler et al (111), showed that elasticity of the matrix on which mesenchymal stem cells (MSCs) were cultured, had altered cell proliferation rates.

Here we focus on hydrogels, which have been used already in numerous clinical applications. A hydrogel is a three-dimensional network of polymers, with the ability to absorb a large amount of water whilst maintaining structural integrity. Hydrogels are considered as adequate soft materials for several biomedical applications such as scaffolds for tissue regeneration and culturing cell substrates, drug delivery and cell encapsulation, and medical devices (112). In a nutshell, hydrogels are widely used as they can mimic physical properties of biological tissues, they are biocompatible, with the potential to respond to small environmental changes. Furthermore, their injectability and the ease of administration through a syringe is a major requirement sought in this thesis.

Table 3.1 Biomaterial Characteristics identified during a range of clinical applications (107)*. This table summarises the use of biomaterials in various of clinical settings, along with their respective outcomes met during the stated applications.*

Biomaterial characteristics							
Application	**Viscosity**	**Setting time**	**Adhesive strength**	**Time to degrade**	**Tissue irritation**	**Tissue ingrowth**	**Controlled degradation**
Arterial hemostasis	Moderate	Rapid	High	Rapid	Low	No	Maybe
Venous hemostasis	Moderate	Rapid	Medium	Rapid	Low	No	Maybe
Sealant (air, fluid)	Moderate	Rapid	High	Medium	Low	No	Maybe
Embolization	Low	-	-	Rapid	High	No	Maybe
Fistula occlusion	Low	-	-	Medium	High	No	Maybe
Joining tissue	Moderate	Rapid	Medium	Rapid	Low	Yes	Yes
Coating implant	Low	-	Low	Slow	Low	Maybe	Maybe
Wound healing	Low	-	Medium	Medium	Low	Yes	Yes
Drug delivery	-	-	-	Slow	Low	No	Maybe
Bone repair	High	Slow	High	Slow	Low	Yes	Yes
Skin grafts	Low	Slow	Medium	Rapid	Low	Yes	Yes

Different biomaterials applications are associated with several design requirements (107); Table 3.1 shows some examples relevant to different applications. Biomaterials have also been developed for some medical applications and they have combined two or more materials to improve their existing mechanical properties and functions. For example, ECM components such as HA, could be added to improve the viscoelastic properties of a biomaterial. HA, the major component of the ECM of the eye, plays an important role in the ocular development and it has been used to embed retinal progenitors, which can proliferate into mature photoreceptors. High HA concentrations are associated with scar-less wound healing; however, they are rapidly absorbed by the body once applied onto the wounded site. Although HA can be used as a potential cellular matrix for the retina, it has the disadvantage of degrading too quickly, by separating prematurely from the attached cells and preventing adhesion onto the inner retina.

Other biomaterials that can be potentially used for retinal cell therapies include fibrin and its derived composites, which are used for selected medical applications. Fibrin, also referred to as fibrin glue (FG) and fibrin sealant, is a biological wound sealant; it is by the far the most complex human plasma derivative and is used across a range of medical applications (113), including cardiovascular, gastrointestinal, cosmetic, oral, orthopaedic, and urology and is the dominant biomaterial used for ophthalmic surgery. FG is used for several surgical and medical platforms to promote homeostasis, tissue bonding and drug delivery. A possible treatment for glaucoma could involve delivering therapeutic stem cells onto the inner retina, embedded in FG. The next section focuses on fibrin in more details and its clinical uses as a cell delivery vehicle.

3.2. Fibrin glue

Fibrin glue (FG), also known as fibrin sealant, has been hailed as the first truly successful adhesive in medicine (114). FG is made of two components, thrombin and fibrinogen. It is a complex and absorbable plasma-derived fluid, which can be used as biodegradable adhesive to control or to stop bleeding, or provide air tightness in several surgical procedures (113,115). The fibrin network provides support to cells, ultimately combining with components from the ECM to rebuild damaged tissue. FG encourages minimal inflammation and it is formed when fibrinogen (the main structural protein responsible for blood clots) binds with thrombin. It is used in numerous surgical procedures spanning neurosurgery, gastrointestinal surgery, plastic surgery and skin grafts. FG also has a wide application in ophthalmic procedures such as corneal perforations, lamellar keratoplasty and suture substitute during glaucoma drainage surgery (70).

FG acts as an adhesive, sealant and haemostatic agent. It is also used for other applications including fistula occlusion, embolization, joining tissues, coating implants, wound healing, drug and cellular delivery, skin grafts and bone repair. FG acts as a tissue engineering scaffold when it is combined with therapeutic cells to form a substrate, therefore protecting cells from forces exerted during the cell delivery process, to enhance cell viability and tissue regeneration (116).The stiffness of the FG clots vary according to the clot structure, which depends on the thickness of fibrin fibre, the pore size of the clots and thrombin concentration. Studies have been carried out showing that a greater thrombin concentration would increase the stiffness of the fibrin gel formed (114). This is an important feature, which will be used in the future to determine the required thrombin concentration to facilitate cell delivery and prevent clogging in the needle. FG has both viscous and elastic properties, and these will be characterised experimentally in this Chapter.

Fibrin-based materials have the advantage of complete degradation and rapid removal from the body. Although there exist synthetic biomaterials that have been used in the clinic for some ophthalmic surgical procedures (such as cyanoacrylates used for skin closures), not all can be applied in the ophthalmic practice. For this reason, biological biomaterials such as fibrin are potential candidate for retinal delivery of stem cells. The have excellent biocompatibility, transparency, setting time and biodegradability and can be applied between tissues (70). It is hoped that the highlighted features of FG will work as advantage during the cell delivery process onto the inner retina. There are still outstanding limitations in adequate methods of cell delivery onto the retina, in order to promote both cell viability and tissue regeneration.

Delivering cells homogeneously and directly onto the large surface area of the inner retina necessitates a minimally invasive method which can be rapid and well controlled. With the high demand for a technique for direct cell application to treat many retinal diseases such as glaucoma, there is a need for designing cell-spraying devices. Hydrogels may exhibit both viscous flow under shear stress and time dependent recovery upon relaxation. These class of hydrogels are known to be shear thinning. Hydrogels with shear thinning properties are known to facilitate cell delivery under stress *in-vivo* applications, by forming desired mechanical and biological properties (117). During a desired spraying event, the chosen hydrogel for potential glaucoma cell-based therapy must flow under modest pressure and set at the targeted area. The mechanical properties of the hydrogel build soon after the injection and maintain the cell in place and be biocompatible with no toxicity. Next, we focus on experimentally characterising the rheological properties of fibrin-derived hydrogels, which have a robust basis for use as the substrate for cell-based therapies in ophthalmology.

3.2.1. Fibrin-derived hydrogel material properties

In this thesis, we computationally model the delivery of cells embedded in a fibrin-derived hydrogel, made by combining thrombin with fibrinogen (67,70), onto the retina (see Chapter 4). Here we quantify the rheological properties of these gels, to provide accurate parameter values for the computational model. These rheological properties depend strongly on the relative volumes of thrombin and fibrinogen used to form the hydrogel. Increasing thrombin concentration relative to that of fibrinogen accelerates the gelation time, resulting in a denser gel with thinner protein fibres; however, high fibrinogen concentrations may cause clogging during spraying (116). Here we quantify the rheological properties of the fibrin-derived hydrogel for a range of thrombin and fibrinogen compositions.

A serial dilution was carried out for both thrombin and fibrinogen, with the aim to suggest potential concentration compositions that will promote cell delivery, without clogging inside the needle. The material properties of these different mixtures have not yet been rheologically evaluated in the literature. Here, each component is diluted using phosphate- buffered saline (PBS). The human thrombin (100 U/ mL), purchased from Sigma- Aldrich (St Louis, USA), was diluted into 200 µL of PBS, to yield concentrations from 5.00 U/mL to 0.04 U/mL. Fibrinogen (110 mg) was also diluted within 4.15 mL of PBS to achieve a final concentration of 26.50 mg/mL. Four mixtures were tested with the same concentration of fibrinogen (0.50 mg/mL) and different thrombin dilution; 0.30, 0.15, 0.08 and 0.04 U/mL of thrombin respectively. The samples were individually loaded onto the rheometer's metal plate of the Discovery Hybrid Rheometer-3 (TA Instruments) (see Figure 3.1), controlled at a constant temperature of 37°C, Firstly, a sweep test is carried out to evaluate critical strain values for the hydrogel by observing the material storage and loss moduli. The region whereby strain is linear is observed and a shear rate value is therefore determined; a shear rate value of 0.015 s^{-1} is therefore selected and applied for the flow peak hold test. The flow peak hold test is carried out

to evaluate the evolution of the viscosity of the biomaterial. Hydrogel samples (with a cylinder-shaped geometry with a cross-sectional diameter of 40.0 mm and vertical height of 1.0 mm) were subject to constant shear rate of 0.015 s^{-1} for a period of 10 minutes (600 s).

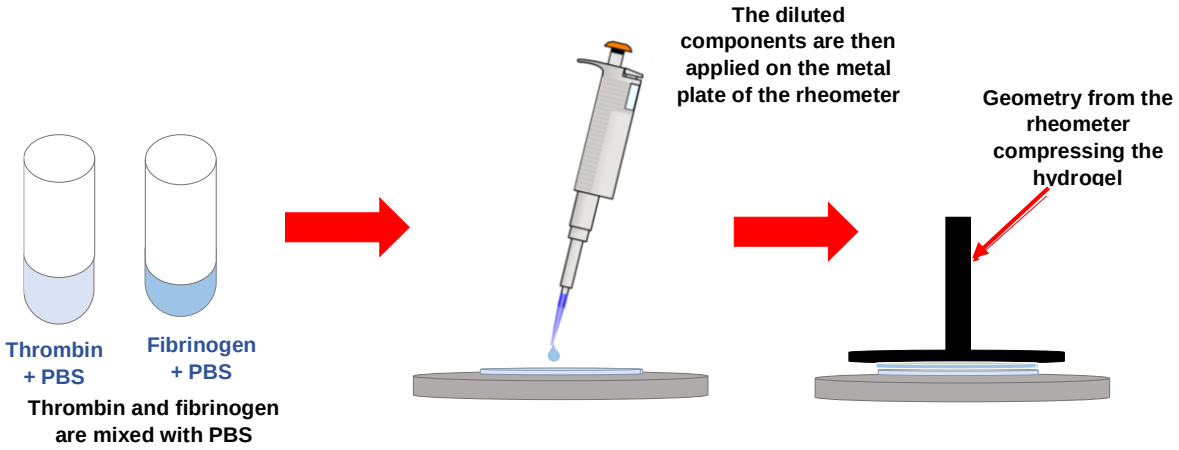

Figure 3.1 Thrombin and fibrinogen are diluted into PBS and mixed to produce hydrogels at a range of concentrations which then underwent rheological testing. Fibrinogen concentration was kept constant at 0.50 mg/ mL, whilst thrombin was diluted from 0.30 U/mL to 0.04 U/mL.

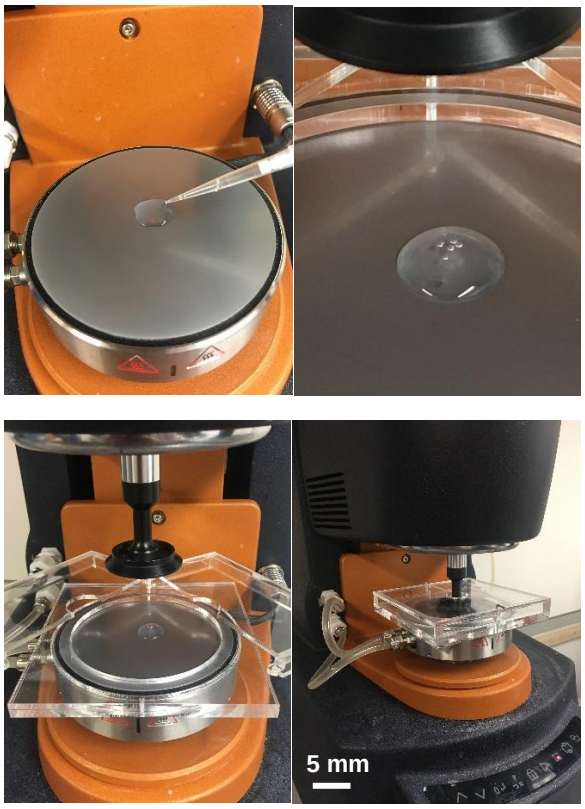

Figure 3.2 Fibrin derived hydrogel sample applied on the rheometer metal plate with a diameter of 40 mm for mechanical testing, using the Discovery Hybrid Rheometer-3 (TA Instruments).

3.3. Results: Rheological Parameters of Fibrin-Based Hydrogels

Figure 3.3 and Figure 3.4 describe how the viscosity of different fibrin-derived hydrogels varies as a function of time. Figure 3.3 describes how the viscosity of hydrogels varies in time for fibrin-derived mixtures with different thrombin concentrations. The fibrinogen concentration and volume are kept constant for all the hydrogel mixtures (0.50 mg/mL and 100 µL respectively); giving a total hydrogel volume of 420 µL. When subject to shear, the viscosity of the fibrin-based hydrogels increases as a function of time and then equilibrates, showing an increase in structural strength of the tested samples between 1.0 and 5.0 s. The lower the concentration of thrombin, the slower the rate to reach the same viscosity of a higher thrombin concentration. For example, for the sample with 1.00 µL of thrombin (0.30 U/mL), the viscosity increases between 3.0 and 9.0 Pa.s in just over 2.0 s. On the other hand, the sample with 0.25 µL of thrombin (0.08 U/mL) takes double the time to achieve the same viscosity. The data shows hydrogel viscosity increasing in time across all samples; the higher the thrombin concentration, the higher the gel viscosity. Thus, the lower the concentration of thrombin in the hydrogel, the longer it would take for the sample to increase in viscosity.

The relaxation time for the hydrogel samples is beyond the 5.0 s testing timeframe, however here we focus on characterising rheological parameters within 5.0 s, as the duration of a spraying event will not exceed this. The dynamic viscosity gradient in time was also dependent on the thrombin concentration; the higher the thrombin concentration, the denser the gel and the higher the maximum linear viscosity before reaching the relaxation period. Thus, the lowest the concentration of thrombin in the hydrogel, the longer it takes for the sample to increase in viscosity. In the first instance in this thesis, we select the mixture with 0.25 µL of thrombin (0.08U/mL) and total volume of 100 mL and impose its time-dependent viscosity into the computational model based on interpolating the data provided in Figure 3.3. However, we note that

it would be straightforward to use the computational model to explore other viscosity profiles in future.

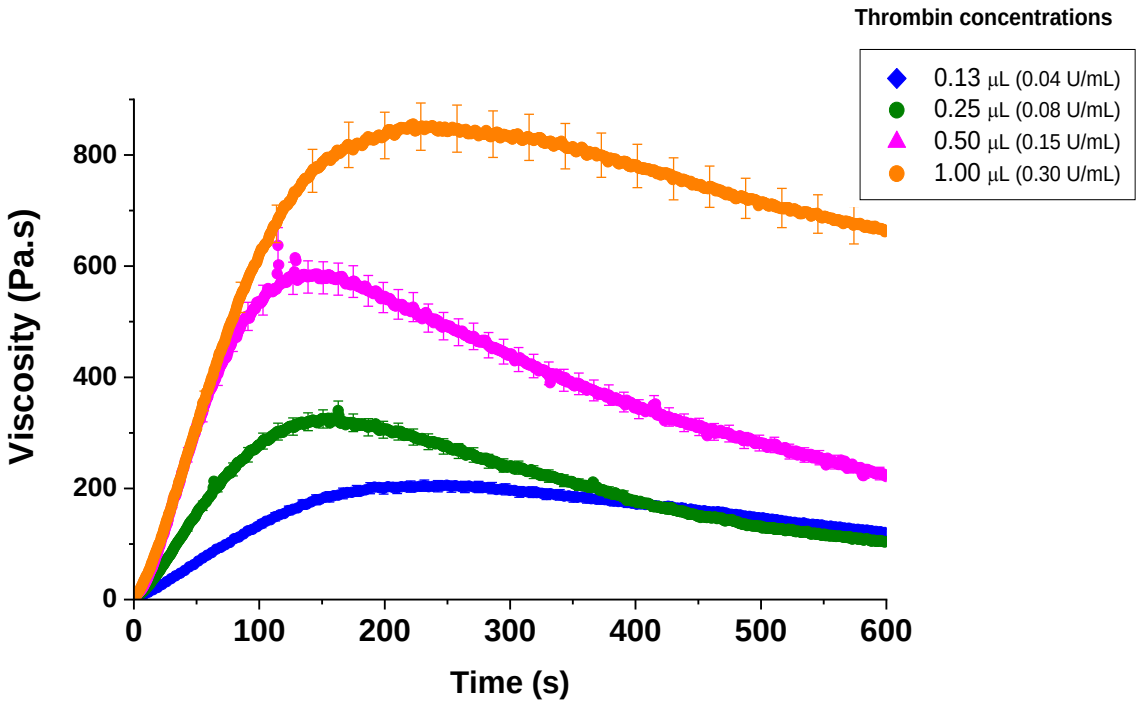

Figure 3.3 Viscosity of fibrin-derived hydrogels with a fixed fibrinogen concentration (0.50 mg/ mL) with a range of thrombin concentrations, as a function of time, as determined via rheological testing (error bars represent standard deviation based on n= 3 repeats).the total volume for each mixture is mantained contstant at 420 µL.

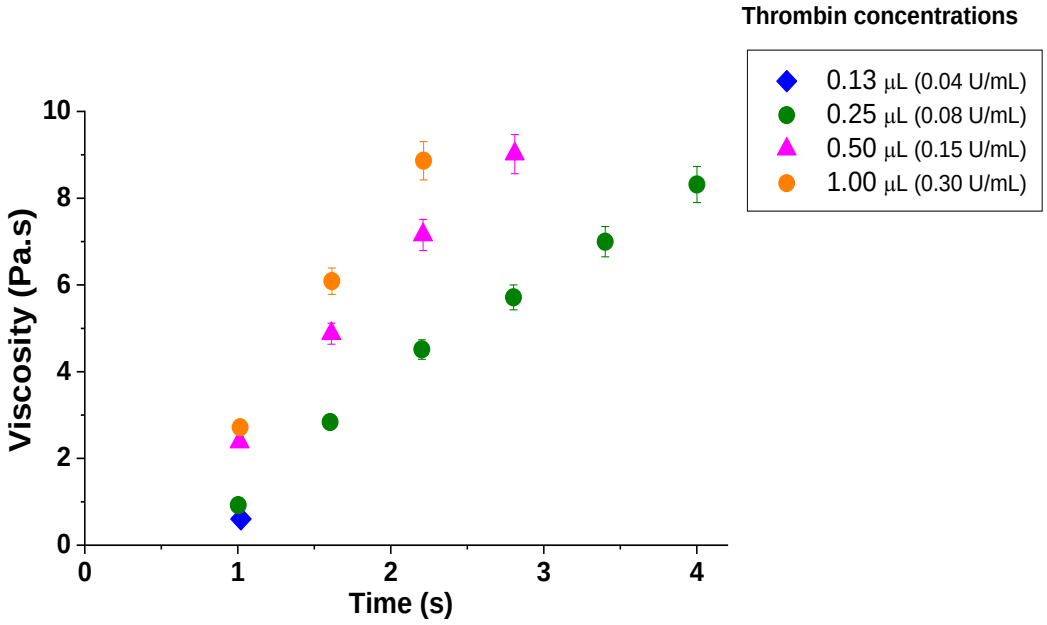

Figure 3.4 Dynamic viscosity as a function of time for fibrin-based hydrogels with constant fibrinogen concentration (0.50 mg/ mL) and a range of thrombin concentrations (results show mean viscosity with error bars representing the standard deviation based on n=3 repeats). Total volume for each hydrogel mixture is fixed at 420 µL. In general, higher thrombin concentrations yielded hydrogels with a higher viscosity.

3.4. Discussion

The goal of this Chapter was to design scaffolds that will be easily injected, promote stem cells delivery onto the desired anatomy, prevent clogging inside the needle, be transparent and controlled degradation. By performing a serial dilution for the components of the fibrin-derived hydrogels, we can quantify the properties of hydrogels with a variety of compositions. The rheological properties of fibrin-based hydrogels were evaluated experimentally (see Figure 3.3 and Figure 3.4). The experimental data suggest that the hydrogels are shear-thinning fluids; however, as the length of spraying is 1 second, the viscosity does not very within this short period of time. Constant shear rate was applied in this research to evaluate gels behaviour, through which rheological properties of hydrogels were analysed at a fixed the time of 10 minutes, however with attention to the first 3 seconds, as the hydrogel will be subject to spraying and a spraying event is assumed to last no more than 3 s. The data from the material characterisation showed that fibrin is a viscoelastic material, exhibiting both elastic and viscous properties.

During a realistic condition, the shear rate level depends on the applied external pressure to the sprayed cellular mixture. Thus, for the highest-pressure condition, the cellular scaffold will be the least viscous. However, it is imperative highlighting that high pressure and high shear, also means reduced cell survival and possibly increase damaged to the remaining retinal tissue. The overall time-dependent hydrogel behaviour exhibited in Figure 3.3 is exported into the mathematical model described in Chapter 4.

These fibrin-derived hydrogels are important as they have the potential to be used as vehicle for Mueller glia stem cell (MGCs) delivery in ophthalmology. Characterising these material properties is important to help predict the behaviour of the mixture during delivery to the retina via aerosolization through mathematical modelling. The rheological properties of the hydrogels were

quantified as a function of time, and these data are now available for importing into a computational model of the spraying process in the next Chapter.

4. Computational Modelling of the Delivery of a Cell-Laden Biomaterial to the Retina

This Chapter begins by discussing the history of computational modelling in healthcare, including within the tissue engineering field. A mathematical model for simulating the spraying of a cell-laden biomaterial onto the retina is developed, and its computational implementation discussed. This consists of constructing a 3D human eye model (using realistic dimensions), followed by discretisation through finite element method (FEM), and applying boundary and ambient conditions to mimic the spraying process and environmental conditions, (including realistic environmental factors, namely temperature and atmospheric pressure), including the spraying parameters (volume flow rate and external air pressure). The mechanical properties of the fibrin-derived hydrogel (see Chapter 3) are inputted as model parameters. A sensitivity analysis is performed to test the influence of spraying parameters (e.g. volume flow rate, injector pressure) on key outputs, such as the surface area of retina covered. These data are used to inform spraying parameters for future experimental testing.

Advances in information technology have revolutionised biotechnology and the world of medicine. Computational fluid dynamics (CFD) is defined as a specialist mathematical area and branch of fluid mechanics, used for numerous engineering-based systems (118). CFD modelling facilitates rapid, economical and low-risk prototyping and has transformed research and development of medical devices and implants. The nature of the physiological problem and the fluid to be investigated determine the mathematical equations to be used in the solver, and CFD is particularly appropriate for complex 3D geometries where analytical analysis would not be possible. The CFD models may require significant computational storage and time to solve, depending on the complexity of the computational model.

Several studies have incorporated mathematical modelling in tissue engineering to promote interdisciplinary collaborations between engineers, biologists and biomedical scientists. Over past decades, mathematical modelling has been used in tissue engineering to review mechanical

stimulations of functional physiological tissues, by simulating realistic physiological environment, incorporate realistic mechanical and chemical factors, to control functional development of tissue engineered structures and predict tissue response prior to pursuing animal studies. (119). Numerical results have had a positive impact in analysing and tuning biological parameters for realistic tissue structures simulated under realistic environmental conditions through mathematical modelling (120). Mathematical modelling in tissue engineering is helping investigate specific biological questions, such as predicting cell mechanics and cell matrix interactions among many others.

Mathematical modelling has therefore been identified to play an important role in improving development of medical implants, improving existing bioreactor designs and tissue engineering therapies through empirical approaches (121,122). This thesis is therefore used to reinforce benefits of mathematical modelling to provide insight for spraying parameters for retinal diseases.

4.1. Computational modelling

Here the computational model is used to describe the spraying technique and underpinning parameter values and implementation. By simulating a physiological environment, we could almost say that CFD introduces a ‘digital patient’ model, whereby realistic human dimensions and boundary conditions in some cases are sought through real patients using medical imaging techniques and conventional diagnostic techniques. To accomplish this process, this thesis uses Simcenter STAR-CCM+, which is a Computational Aided Engineering (CAE) package providing integrated components such as 3D-CAD modelling, CAD embedding, surface preparation tools, automatic meshing technology, physics modelling and post-processing. Construction and solution of a CFD model can be generally described into five stages: reconstruction of the 3D model, discretisation, defining the physical model, boundary conditions application, simulation and post processing.

4.2. Reconstruction of the 3D model

A 3D anatomical structure can be extracted through medical imaging techniques such as ultrasound, CT, MRI or X-ray. However, in this research, eye dimensions are taken from literature to build a 3D representative eye geometry (see Figure 4.3) which is then discretised and used as the basis for simulations.

4.3. The Mathematical model

The spraying of the cell-laden hydrogel is simulated by assuming stem cells are embedded in the fibrin-derived gel. The mixture is sprayed onto the retina surface of the human eye (3D model). A two-phase spray nozzle (comprising of air and the cell- laden hydrogel) is used to generate the spray at a known distance *s* from the sclera as shown in Figure 4.1. The fluid at the injector is

defined as continuum using the Lagrangian Multiphase model, with a constant density, laminar flow and the same material properties of the hydrogel characterised in Chapter 3. The multiphase interaction model is used to define how the fluid and gas phases interact with each other and contains sub-models predicting conservation of mass, momentum and energy between the two phases. We create a phase interaction between the Lagrangian phase and the fluid-film phases. The fluid- film boundary condition is set as such that an additional fluid- film and wall boundaries are automatically added; to allow cell-laden hydrogel droplets defined as Lagrangian phase, to be collected at the retina wall as fluid-film (hence mimicking cell and gel attachment at the retinal wall).

The geometry of the model is based on mean dimensions of an adult human eye and the inner retina covers approximately ¾ of the inner optical surface (102). The 3D domain that is modelled, includes a spherical eye with mean diameter of 25 mm (102) and an injector nozzle is introduced at position (x_1, y_1, z_1) mm from the centre of the eye, which is used as origin from the schematic and for cell delivery directed towards the optic nerve and macula. The cell-laden hydrogel is aerosolised through the nozzle injector and the suspension droplets are directed at the optic nerve. A Lagrangian approach is implemented and the cell suspension droplets are defined as multiphase viscous material. The droplets' path is confined in a cone-like pattern, generated following the fluid-gas interaction at the injector nozzle and directed to cover the optic nerve and macula (105). The cone pattern created by the sprayed cellular mixture predicts and defines the sprayed surface area of the retina. Equations of conservation of mass, momentum and energy are solved for each phase identified (air and cell-laden hydrogel). Each phase is assumed as incompressible and with a laminar flow. Materials properties for air (using Navier-Stokes equations as derived in section 4.6) and rheological properties for the cell-laden hydrogel are defined; the latter are extracted from results of Chapter 3.

A no-slip boundary conditions are defined at the retinal wall. An implicit unsteady model with segregated flow is introduced for time-dependency for conservation equations for the gas -phase using the second order upwind scheme. A pressure swirl injector was used to describe the injector inlet, through the Linear Instability Sheet Atomization (LISA) model, using stated assumptions in Section 4.7.3. A summary of parameters computed are shown in Table 4.2. The Lagrangian and Eulerian approach implemented in the mathematical model are now explained further.

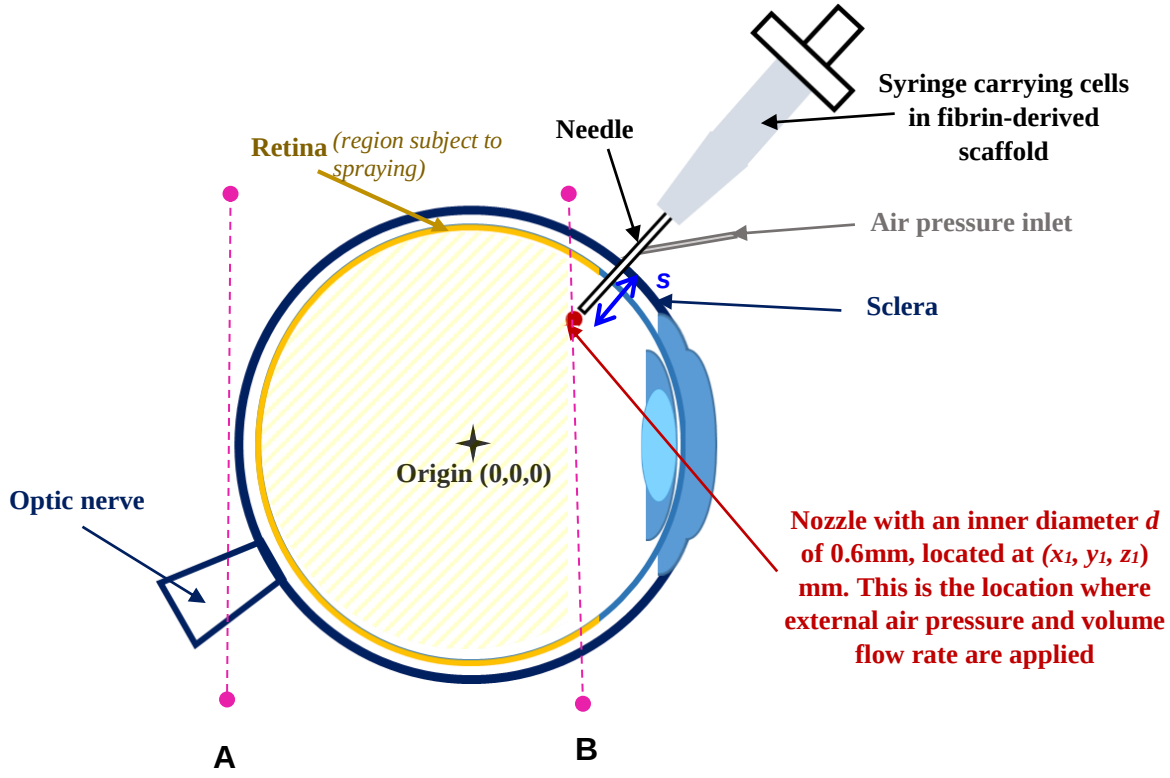

Figure 4.1 Schematic representation of the simulation geometry, showing the injector nozzle, optic nerve and retina locations. For the simulations presented here, the diameter of the eye (measured to the sclera) is fixed at 25 mm, the diameter to the retina is approximately 24 mm, and the injector has an inner diameter of 0.6 mm, positioned with its outlet at (x_1, y_1, z_1) mm. The position of the nozzle defines the distance s, which is the distance between the nozzle position and the sclera. The geometry between points A and B represents the geometry modelled in the 3D mathematical.

4.4. Eulerian Approach vs Lagrangian Approach

There are two methods for modelling particle transport in CFD analysis: the Eulerian and the Lagrangian methods. In the Eulerian multiphase model, the phases are described using a continuum approach. The droplets of the cellular suspension are defined as one phase, treated as continuum. Equations of conservation of mass, momentum and energy are solved for each phase, using a control volume as the reference space (Figure 4.1). The Lagrangian method provides a statistical approach that uses a discrete model and subsequently calculates the overall particle concentration within the domain. This method tracks the pathway of each individual particle (123). By tracking the trajectory of individual particles, the Lagrangian method is also able to predict the overall particle dispersion pattern, assess the particle concentration distribution and calculate particles dimension.

In summary, whilst the Eulerian approach models conservation of mass and momentum through continuum approaches throughout the domain, the Lagrangian approach applies counterpart physical descriptions to each fluid particle. With the aim of predicting the overall dispersion pattern and film thickness of the cellular suspension droplets along with other droplet specific properties (such as droplet dimension), the Lagrangian approach is the most suitable. The Lagrangian method can also predict detailed particles properties, although this requires greater computation time and storage.

Through the Lagrangian framework, the properties of fluid particles such as position, velocity and change in temperature can be determined as the particles move and interact with each other within the domain. The Lagrangian method locates each sprayed particle. Considering a particle with a velocity vector $\mathbf{u}$, $\mathbf{u}$ is dependent on ($\mathbf{x}_0$, t), where $\mathbf{x}_0$ is the initial position of the particle at a fixed time t. In the same manner, the density of the particle ρ is also dependent on the initial position $\mathbf{x_0}$ and time t. The acceleration $\boldsymbol{a}$ of the particle

is defined as the derivative of the velocity vector **u**, as $\boldsymbol{a} = \frac{\partial \boldsymbol{u}}{\partial t}$. If the fluid is incompressible in the Lagrangian framework, the density of each particle remains constant so that

$$\frac{\partial \rho}{\partial t} = 0. \tag{4.1}$$

In the Eulerian model, on the other hand, the fluid properties are observed as a function of a fixed spatial location $\boldsymbol{x}$ so that.

$$\boldsymbol{u} = \boldsymbol{u}(\boldsymbol{x}, t) \text{ and } \rho = (\boldsymbol{x}, t). \tag{4.2}$$

The new position of the particle after a minimum time change δt is defined as $\boldsymbol{x} + \delta \boldsymbol{x}$. Therefore, the velocity at the new position is given, using a Taylor series expansion by

$$\boldsymbol{u}(\boldsymbol{x} + \delta \boldsymbol{x}, t + \delta t) = \boldsymbol{u}(\boldsymbol{x}, t) + (\delta \boldsymbol{x} \cdot \nabla)\boldsymbol{u} + \delta t \frac{\delta \boldsymbol{u}}{\delta t} + O(\delta \boldsymbol{x}^2, \delta t^2). \tag{4.3}$$

Analogously the acceleration is

$$\lim_{\delta t \to 0} \frac{\boldsymbol{u}(\boldsymbol{x}+\delta \boldsymbol{x}, t+\delta t) - \boldsymbol{u}(\boldsymbol{x}, t)}{\delta t} = \frac{\delta \boldsymbol{u}}{\delta t} + \boldsymbol{u} \cdot \nabla \boldsymbol{u} \equiv \frac{D\boldsymbol{u}}{Dt}; \tag{4.4}$$

where, $\frac{\delta}{\delta t} + \boldsymbol{u} \cdot \nabla \equiv \frac{D}{Dt}$ is known as the rate of change with time following the fluid particle. The velocity of a particle can change as a function of the coordinate system. In the Eulerian model, if a fluid is incompressible, the density of the particle is constant, but not the density of the fluid at a fixed position in space. Thus, incompressibility in the Eulerian framework is defined as

$$\frac{D\rho}{Dt} = 0 \ . \tag{4.5}$$

We assume the cellular suspension is an incompressible fluid; as the density is constant as defined in equations (4.1) and (4.2). We will use conservation

of mass and momentum to derive the Navier-Stokes equation and predict the Reynold's number for our fluid flow.

We note that in the surgical setting explored in this thesis, temperature is constant and thus conservation of energy is automatic (does not need to be solved for).

4.5. Dispersed phase – droplets

The droplets of the cellular suspensions are defined as the dispersed phase within the domain. These droplets consist of neural stem cells and the fibrin-derived hydrogel, which is in turn formed by combining two components known as fibrinogen and thrombin. A multicomponent fluid can be assumed to be emulsified or miscible. For an emulsified mixture, it is assumed that the liquid droplets are unaffected by the presence of air pressure. In a miscible mixture, on the other hand, the two components (liquid and gas) are affected by each other's flow. This relationship is also known as two-way coupling, which will be discussed later.

Droplets may become unstable as a result of their motion relative to the continuous phase. STAR-CCM+ provides system specific models addressing break-ups of liquid models within a gaseous system, namely Reitz and Diwakar model, Kelvin-Helmholtz Rayleigh- Taylor model, Stochastic Secondary Droplet model and Taylor Analogy Breakup models.

The momentum equation for each individual droplet is given by

$$m_d = \frac{d\boldsymbol{u}_d}{dt} = \boldsymbol{F}_{dr} + \boldsymbol{F}_p + \boldsymbol{F}_{am} + \boldsymbol{F}_b \tag{4.6}$$

Where

- m_d is the mass for each droplet;
- $\boldsymbol{u}_d$ is velocity of each droplet;

- $\boldsymbol{F}_{dr}$ is the drag force;
- $\boldsymbol{F}_{p}$ is the pressure force;
- $\boldsymbol{F}_{am}$ is the virtual mass- defined as the force needed for the fluid contained in each droplet to travel within the domain;
- $\boldsymbol{F}_{b}$ is the body force.

However, implementing equation (4.6) for each droplet would not be practical. In STAR-CCM+, liquid droplets are also referred to as particles. In the Lagrangian framework the liquid particles are grouped into parcels, in turn representing populations of droplets with alike properties and modelled as continuum. Using the Lagrangian framework the collective behaviour of the droplets will be assessed by solving equation (4.6) as a sum of all the droplets. The droplets are followed through the domain and recorded through the particle tracking feature; they can be modelled as material particles or massless particles. In this study, the droplets are modelled as real particles, by assigning realistic material properties.

Depending on the nature of the problem assessed, multiphase flows can be simulated differently. STAR-CCM+ provides six different mathematical models:

- The Multiphase Segregated Flow, also known as the Eulerian Multiphase model. In this model, the conservation equations for mass, momentum and energy are solved for each phase. A phase interaction model is introduced to define the affect one phase has onto another.
- The Lagrangian Multiphase model, where the equations of motion are solved for the dispersed phase within the domain. The droplets are treated as a continuum. This is applied for systems with a single continuous phase holding a very small volume of particles.
- The Dispersed Multiphase Model, which combines aspects from both the Lagrangian Multiphase model and the Segregated (Eulerian) Multiphase model, using the Eulerian framework.

- The Discrete Element Model is an extension of the Lagrangian Multiphase model; however, the equations of motion are applied to individual particles rather than applying the equations to clusters of particles, also known as parcels.
- The Fluid Film Model, which uses boundary layer approximation to determine the dynamic characteristics of wall films; such as film thickness, change in temperature, viscosity and shear stress.
- The Volume of Fluid Model, which is applied to a system with two or more immiscible fluid phases. This model looks at the interface between the fluid phases and is mostly applicable for marine applications.

In summary, the models above are built using either the Eulerian approach or the Lagrangian approach. STAR-CCM+, provides a Lagrangian/Eulerian approach, whereby the momentum and energy equations for the dispersed phase are derived for each droplet.

4.6. Derivation of Navier-Stokes Equations for Flow of a Single-Phase Fluid

The Navier-Stokes (NS) equations can define the velocity vector field that applies to a fluid. They can be determined by applying Newton's second law of motion in combination with fluid stress as a result of viscosity, and a pressure term. The NS equations can be derived considering the basic conservation and continuity equations.

4.6.1. Mass conservation

Considering an arbitrary fixed control volume in the lab frame as shown in Figure 4.2, the theory of mass conservation states that the amount of mass entering a system is equal to the quantity of mass contained within the system itself.

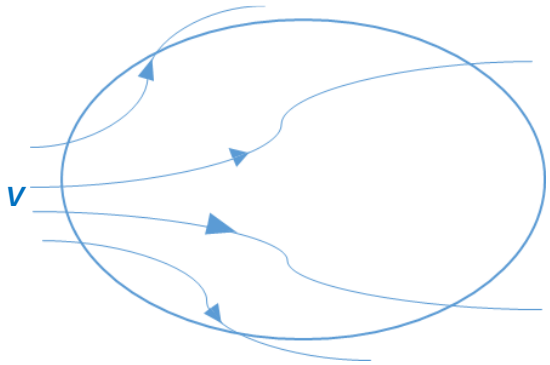

Figure 4.2 Fixed control volume V in a lab frame, where the streamlines are used to visualise the fluid flow.

In other words:

$$\frac{d}{dt}\int_V \rho \, dV = -\int_{\partial V} \rho \boldsymbol{u} \cdot \boldsymbol{n} \, dS, \tag{4.7}$$

where $\boldsymbol{n}$ is the unit outward-pointing normal to ∂V. Applying the divergence theorem to equation (3), we obtain

$$\int_V \frac{\partial \rho}{\partial t} dV = -\int_V \nabla \cdot (\rho \boldsymbol{u})\, dV, \tag{4.8}$$

$$\therefore \int_V \frac{\partial \rho}{\partial t} dV + \int_V \nabla \cdot (\rho \boldsymbol{u})\, dV = 0. \tag{4.9}$$

With the integrals and volumes worth nothing as V is fixed in time t, the differential equation defining mass conservation is reduced to

$$\frac{\partial \rho}{\partial t} + \nabla \cdot (\rho \boldsymbol{u}) = 0. \tag{4.10}$$

The equation can be rearranged as

$$\frac{D\rho}{Dt} + \nabla \rho \cdot \boldsymbol{u} = 0. \tag{4.11}$$

Hence, if the fluid is incompressible, we have

$$\nabla \cdot \boldsymbol{u} = 0. \tag{4.12}$$

4.6.2. The momentum equation

The rate of change of total momentum within the control volume (Figure 4.2) is determined by the momentum flux acting through the boundary and the forces acting on the fluid. Such relationship can be expressed as:

$$\frac{d}{dt}\int_V \rho\, \boldsymbol{u} dV = -\int_{\partial V} (\rho \boldsymbol{u}) \boldsymbol{u} \cdot \boldsymbol{n}\, dS + \frac{d}{dt}\int_V \boldsymbol{F}\, dV + \int_{\partial V} \sigma \boldsymbol{n}\, dS. \tag{4.13}$$

Rate of change of tot. | Momentum flux | Body force | Surface forces

Sigma (σ) from (4.13) is the stress tensor. By assuming the fluid in question is a Newtonian fluid (which has isotropic properties), its stress and rate of strain have a linear relationship so that the stress tensor is symmetrical. In a nutshell, there is a direct proportionality between the stress in each direction and the strain in that same direction. Thus:

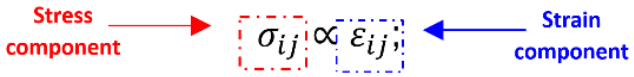

Where the stress component is the same in all directions ($\sigma_{ij} = \sigma_{ji}$). We split the stress tensor $\boldsymbol{\sigma}$ into an isotropic part and non-isotropic part, also known as the deviatoric stress tensor **d**. The isotropic component assumes the fluid is pushed equally in all directions, and the deviatoric stress **d** is dependent on the velocity gradient $\nabla \cdot \boldsymbol{u}$ with **d**=0, when $\nabla \cdot \boldsymbol{u} = 0$. With stress being symmetrical, **d** is defined as

$$d_{ij} = A_{ijkl} \frac{\partial u_k}{\partial x_l}, \tag{4.14}$$

where A is the isotropic part of the stress tensor (assuming we have an isotropic fluid) and (4.14) includes both velocity and stresses as variables. By assuming **A** is isotropic, it can be defined as

$$A_{ijkl} = \lambda \delta_{ij} \delta_{kl} + \mu \delta_{ik} \delta_{jl} + v \delta_{ij} \delta_{kj}; \tag{4.15}$$

where λ, μ and v are constants. Therefore, from the symmetrical nature of stress, we conclude that the deviatoric stress **d** is also symmetrical.

Thus, considering stress tensor σ and (4.14), (4.13) can also be defined as

$$\int_V \frac{\partial}{\partial t} (\rho \, \boldsymbol{u_i}) dV = - \int_V \frac{\partial}{\partial x_j} \left(\rho u_i u_j \right) dV + \int_V F_i \, dV + \int_V (\sigma_{ij}) \, dV,$$

$$\therefore \rho \frac{D\boldsymbol{u}}{Dt} + \boldsymbol{u} \left(\frac{\partial \rho}{\partial t} + \nabla \cdot (\rho \boldsymbol{u}) \right) = \boldsymbol{F} + \nabla \cdot \sigma. \tag{4.16a}$$

As mass is conserved, the second term from (4.16b) reduces to zero so that

$$\rho \frac{D\boldsymbol{u}}{Dt} = \boldsymbol{F} + \nabla \cdot \sigma. \tag{4.16b}$$

Thus $d_{ij} = d_{ji}$ and $A_{ijkl} = A_{jikl}$; therefore $\mu = v$. As such, using equation (4.17):

$$A_{ijkl} = 0 \Longrightarrow 3\lambda + \mu + v = 0,$$

$$\therefore 3\lambda + 2\mu = 0,$$

$$\therefore 3\lambda = -2\mu,$$

$$\therefore \lambda = -\frac{2\mu}{3}\,. \tag{4.17}$$

Therefore, the definition of **d** becomes:

$$d_{ij} = \mu\left(\frac{\partial u_i}{\partial x_j} + \frac{\partial u_j}{\partial x_i}\right) - \frac{2}{3}\mu\frac{\partial u_k}{\partial x_k}\delta_{ij}, \tag{4.18}$$

Where the constant μ is the dynamic viscosity of the fluid. Using σ for (4.16) gives:

$$\rho\frac{D\boldsymbol{u}}{Dt} = -\nabla\boldsymbol{p} + \mu\nabla^2\boldsymbol{u} \equiv \rho\left(\frac{\partial \boldsymbol{u}}{\partial t} + \boldsymbol{u}\cdot\nabla\boldsymbol{u}\right) = -\nabla\boldsymbol{p} + \mu\nabla^2\boldsymbol{u}. \tag{4.19}$$

The above expression, together with equation (4.12) as the conservation of mass, are also known as the Navier-Stokes equations. Next we non-dimensionalise the NS equations to identify the dominant terms and physics.

4.6.3. Non-Dimensionalisation of Navier-Stokes equation

We perform a non-dimensionalisation to assess the relative importance of different terms in the Navier-Stokes equations. To perform non-dimensionalisation, we rescale all the variables using five different parameters: density ρ, viscosity μ, characteristic time, reference length and velocity. This will enable us to assess the magnitude of the different terms in the Navier-Stokes equations and to define the Reynold's number.

1. *Characteristic length scale*

Assuming a Cartesian coordinate system, the spatial coordinates are normalised as follows:

$$x^* = \frac{x}{L};\ y^* = \frac{y}{L};\ z^*\frac{z}{L}; \tag{4.20}$$

where L is the characteristic length. The gradient operator |∇| is defined as$\left|\frac{\partial}{\partial x}, \frac{\partial}{\partial y}, \frac{\partial}{\partial z}\right|$, the non-dimensionalisation of the Laplacian operator gives:

$$\nabla = \frac{\partial}{\partial x^* L}, \frac{\partial}{\partial y^* L}, \frac{\partial}{\partial z^* L} = \frac{1}{L}\left(\frac{\partial}{\partial x^*}, \frac{\partial}{\partial y^*}, \frac{\partial}{\partial z^*}\right)$$

$$\therefore \nabla = \frac{1}{L}\nabla^*. \tag{4.21}$$

Therefore, the same applies for $\nabla^{*2} = L^2\nabla^2$;

where $\nabla^2 = \frac{\partial^2}{\partial x^2} + \frac{\partial^2}{\partial y^2} + \frac{\partial^2}{\partial z^2}$.

2. *Timescale*

$$t^* = \frac{t}{t_{ref}}. \tag{4.22}$$

Where t_{ref} is the time it takes the fluid to travel across the characteristic length.

3. *Velocity scale*

$$\boldsymbol{u}^* = \frac{\boldsymbol{u}}{U}. \tag{4.23}$$

Where U is the velocity defined throughout the boundary conditions.

4. *Pressure Scale*

$$p^* = \frac{p}{\mu\frac{U}{L}}. \tag{4.24}$$

Where $\mu\frac{U}{L}$ defines pressure scale and it balances pressure changes with viscous forces; therefore from (5) by substitution

$$\frac{\rho U}{t_{ref}}\frac{\partial \boldsymbol{u}^*}{\partial t^*} + \rho\frac{U^2}{L}\boldsymbol{u}^* \cdot \nabla^*\boldsymbol{u}^* = -\mu\frac{U}{L^2}\nabla^* p^* + \mu\frac{U}{L^2}\boldsymbol{u}^*\nabla^{*2} \tag{4.25}$$

Dividing through by $\mu \frac{U}{L^2}$ gives

$$\rho \frac{UL}{\mu} \frac{L}{t_{ref} U} \frac{\partial \boldsymbol{u}^*}{\partial t} + \rho \frac{UL}{\mu} \boldsymbol{u}^* \boldsymbol{\nabla}^* \boldsymbol{u}^* = -\boldsymbol{\nabla}^* p^* + \boldsymbol{\nabla}^{*2} \boldsymbol{u}^* \tag{4.26}$$

Re 1/ St Re

The Strouhal Number (St) and Reynold's number (Re) are the two dimensionless coefficients. St is a function of Re, and it measures the rate of the inertial forces as a result of the unsteadiness of the flow, due to changes in the velocity across the characteristic length. Re defines the ratio between inertial and viscous forces, with the viscous forces being dominant in this experimental setup. Therefore, the above equation can be rewritten as

$$\frac{Re}{St} \frac{\partial \boldsymbol{u}^*}{\partial t^*} + Re \boldsymbol{u}^* \cdot \nabla \boldsymbol{u}^* = -\nabla^* p^* + \nabla^{*2} \boldsymbol{u}^*. \tag{4.27}$$

For microfluidic flows, we expect the Re to be relatively small, as a result of the small velocities and length scales involved. In this scenario, terms multiplied by Re and St can be ignored, simplifying equation (4.27) to

$$\nabla^* p^* = \nabla^{*2} \boldsymbol{u}^*. \tag{4.28}$$

Equation (4.28) is also known as the Stokes equation, and is the governing equation for a low Re flow. Next, we consider the model for transport in the multiphase region. The discretisation process is now described.

4.7. Discretisation

The computational model described is solved using finite element method (FEM) through the CFD solver Simcenter STAR-CCM+. Spatial discretisation (also known as meshing), is the process whereby the 3D geometry is divided into discrete volumetric elements and cells (118). A mesh element is made of vertices, faces and cells, where several vertices define a face. A cell is a collection of faces defining a closed volume. There are several meshing strategies available on Simcenter STAR-CCM+ as summarised in Table 4.1. A mesh can be unstructured or structured. With unstructured meshing, the mesh is built using either region-based or part-based information from the geometry. Part-based meshing provides better repeatability compared to region-based meshing, as it allows the geometry to be easily modified and the changes automatically propagates to the mesh and volume of the geometry itself. With region-based meshing on the other hand, geometry changes must be specified for each region, volume, feature curve and boundary individually.

The meshes that are currently available in parts- and region-based meshing are summarised in Table 4.1; surface wrapping, surface remesh, automatic surface repair, polyhedral mesh, tetrahedral mesh, trimmed mesh, prism layer mesh, advancing layer mesh, extruder mesh, thin mesh, generalized cylinder mesh. Using the automesh facility provides benefits such as size customisation, volume control and minimum input required by the user. The two main options suitable for a 3D geometry are tetrahedral and polyhedral meshes, and we discuss these next. Tetrahedral meshes are relatively easy to generate automatically, very popular and are therefore used by major CFD software tools such as CCM+. For the solution to achieve the desired degree of accuracy, a mesh convergence study needs to be carried out; as the mesh is refined, the solution becomes more accurate. When using a tetrahedral mesh, mesh refinement is carried out with tetrahedral elements by reducing the base size of the element mesh, therefore increasing the total number of elements in the geometry, memory and computing time requirements (124).

Polyhedral meshes consist of arbitrary polyhedral-shaped cells, they have the same benefits as tetrahedral meshes. Although both mesh types are easy to build, with more neighbouring cells, polyhedral meshes are more flexible due to the number of neighbouring cells discretisation of a domain using linear shape functions and offer more accurate final solution compared to tetrahedral meshes (125). This is not the case when using a tetrahedral mesh. Polyhedral cells can be automatically modified (split or joined) by introducing more points, edges and faces which are controlled according the specified mesh element size. More neighbouring cells require more storage and computing operation per cell; with fewer cells compared to tetrahedral mesh, polyhedral meshes are more efficient computationally. Polyhedral cells are considered suitable for this research, as fewer polyhedral elements are needed to achieve a specific accuracy compared to tetrahedral meshes (124).

To create a mesh through part-based meshing, the automated mesh operation is activated from the geometry dialog. The desired mesh types are selected from the continua mesh node. In this thesis a part-based mesh was generated using polyhedral elements and a tetrahedral mesh was therefore applied to the 3D geometry. To improve the solution accuracy, the prism layer mesh is selected to generate orthogonal prismatic cells next to wall boundaries. The surface remesh tool is finally used to optimize the surface of the geometry (see Figure 4.3), followed by a mesh convergence study.

4.7.1. Initial and Boundary Conditions

Two distinct boundaries are defined in the geometry: the wall region (representing the surface of the eye) and the pressure inlet boundary, where the injector nozzle is applied (see Figure 4.4). The pressure boundary is set as per vitrectomy, whereby the intraocular pressure is stabilised by creating an additional incision on the sclera. A no-slip condition is applied at the wall of

the eye for all phases. The fluid-film model is used to model distribution of the cellular scaffold on the retina wall.

After creating the geometry of the eye, the initial and boundary conditions are assigned to mimic experimental and environmental conditions (see Figure 4.1).The properties of the injector are used to define the initial conditions for the cellular suspension droplets, which will be discussed later in Section 4.11 To mimic a realistic biological setting, the atmospheric pressure is used as reference pressure of 101 325 Pa. the temperature is assumed constant at 37°C (293 K).The recorded initial pressure inside the eye (at the initial time *t* of 0 s) is assigned to be a healthy human intraocular pressure of 12 mmHg (126).We therefore predict the behaviour of the cellular scaffold under air pressure conditions between 10 kPa and 100 kPa and volume flow rates between 100 and 400 µL/s (127).

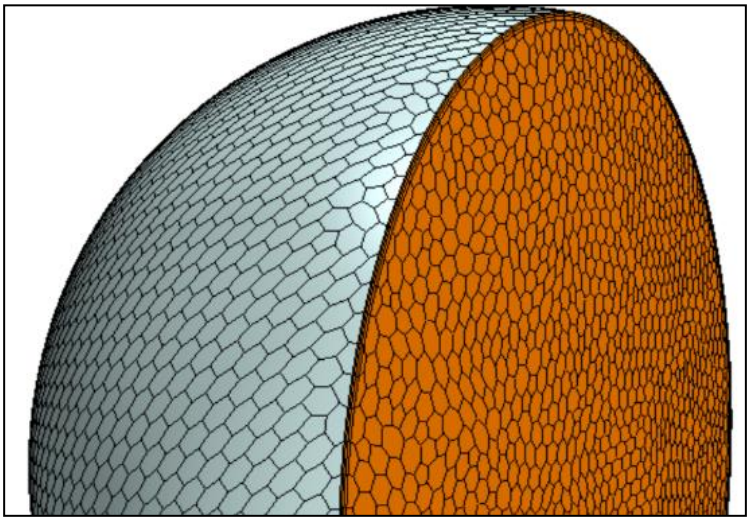

(a)

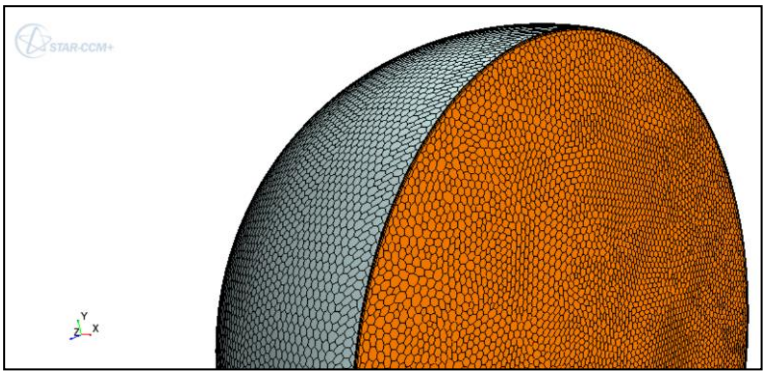

(b)

Figure 4.3 Geometry of the eye with assigned mesh, showing refinement of the edge element size from 0.6 mm (a) to 0.8 mm (b).

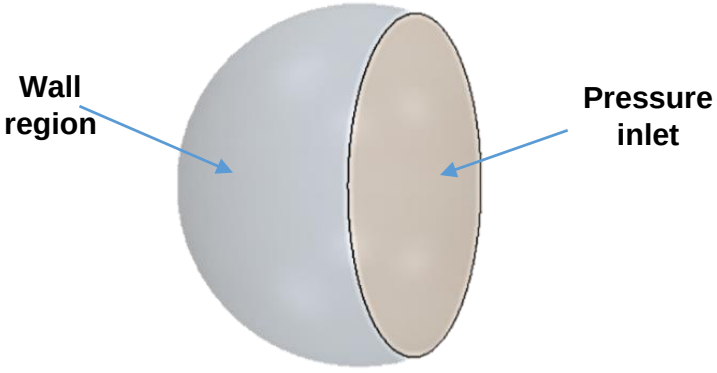

Figure 4.4 3D model with defined boundaries (wall and pressure inlet).

Table 4.1 Table of supported meshes in Simcenter STAR- CCM+

Mesh	Region-based meshing	Parts-based meshing
Surface wrapper	X	X
Surface remesh	X	X
Automatic surface repair	X	X
Polyhedral mesh	X	X
Tetrahedral mesh	X	X
Trimmed mesh	X	X
Prism layer mesh	X	X
Advanced layer mesh	X	
Extruder mesh	X	
Thin mesh	X	
Generalized cylinder mesh	X	

Table 4.2 List of parameters used for the computational model.

Parameters	Value
• Gravity	9.81 m/s^2
• Temperature	293 K (37°C)
• Continuous phase material properties	
(air)	1.184 kg/m^3
-Density	1.855x 10^{-5} Pa·s
-Viscosity	
• Fibrin-derived hydrogel material properties	
-Density	Taken from Figure 3.3 and Figure 3.4
-Dynamic viscosity	
• Duration of spraying event	1 s
• Reference pressure	101 325 Pa
• Pressure inside the eye	1599.864 Pa (12 mmHg) (128)
• Injector position	(x_1y_1,z_1) mm = (3,7,0) mm
• Pressure at injector	10, 25, 50, 70, 100 kPa
• Volume flow rate of cellular suspension	100 – 400 µL/s
• Outer cone angle	5- 100°

4.7.2. Injector Models in STAR-CCM+

To simulate cell spraying, the injector nozzle is applied on the 3D eye model. Simcenter STAR-CCM+ currently provides eight types of injectors and each type is represented through individual properties that describe where and how the droplets are ejected.

- Part injector- representing a collection of injection points, which are positioned based on the geometry of the part selected.
- Point injector- where a single point of injection is specified
- Hollow cone injector- the parcels are injected in a cone formation about a specified axis.
- Solid cone angle- similar to the hollow cone injector type, except only the outer cone angle is specified.
- Surface injector- the particles are injected from the centroid of a face of the geometry
- Pressure swirl injector- used with the Linear Instability Sheet Atomization (LISA) where properties of the injector are defined.
- Lattice injector used with the Discrete Element Method to inject particles using specified mesh independent spatial distribution.
- Random injector also used with the Discrete Element Method, the particles are injected with a random point of distribution and the number of injected particles is specified.
- Film stripping to simulate particles formed from the surface of a fluid film.

To simulate the setup from Figure 2.7, we implemented the pressure swirl injector type through the LISA model, to mimic aerosol cell-spraying, to define the injector nozzle by applying the characterised hydrogel material properties and applying the external pressure as a secondary inlet, to create

aerosolization effects. Through this model we are also able to predict the external spray behaviour by defining values for the outer cone angle. This parameter will be used to control the surface area of the retina needing cell treatment, specifically spraying of the cell-laden hydrogel, of which values used are shown in Table 4.2.

The purpose of the pressure swirl atomizer is to generate small droplets, distributed over a wide angle. Theoretically, with this type of atomizer, a swirl motion takes place; through a centrifugal force, the liquid spreads out in the form of a conical sheet developing either a hollow or solid air cone. However, we are yet to determine whether such assumption is valid for our situation, but let's assume it does. We now explain the LISA model.

4.7.3. The LISA Model

The LISA model acts as primary atomization process, whereby a liquid is forced through an orifice at a high pressure, thus resulting in a fine spray of liquid droplets (105). The LISA model introduces a secondary inlet, where external air pressure is applied as a secondary inlet; we mimic this by imposing pressure at the injector. This was computationally achieved by implementing the LISA model and the pressure swirl injector type. The model consists of three stages: film formation, sheet break-up and lastly atomization (see Figure 4.5). Firstly, as the air pressure is applied at the injector nozzle, a swirling motion applies and gradually forms a film from the injected liquid with initial thickness $\delta_0$within the injector. As the liquid starts to accelerate, it creates a sheet breakup, finally undergoing atomization. This relationship is used to define the LISA model within the developed computational model of the human eye, to predict the ejection of the cell-laden hydrogel from the injector into the eye cavity. The CFD solver Simcenter-CCM+ implements the equation (4.29) below to predict the mean thickness of the cellular scaffold sprayed at the retinal wall. The thickness of the film is therefore calculated based on the

parameters specified for the pressure-swirl injector with the following mathematical expression:

$$\dot{m}_f = \pi \rho u_f \delta_0 (d_0 - \delta_o); \tag{4.29}$$

where $\dot{m}_f$ is the mass flow rate through the injector (which we specify), ρ is the density of the continuous phase (air inside the eye), d_0 is the injector diameter and δ_0 is the initial film thickness in the nozzle. (see Table 4.2). this theory (which is valid for multiphase models) The axial component of the velocity at the injector exit defined as u_f is assumed to be uniform. This is the first time the LISA model is used to predict spraying processes in the eye, and still requires extensive validation to be taken forward. Usually, the mass flow rate would be determined experimentally, however, in this first instance, the mass flow rate was determined by considering realistic clinical measurements of volume of cellular suspension to deliver, capacities of syringe to use in the Baxter system, and time course duration of one spraying event.

During the sheet breakup stage, the effects from surrounding gas, liquid viscosity and surface tension on the breakup of the liquid sheet are considered, as shown in Figure 4.5. As details of our spraying system are yet to be characterised, future experiments could be carried out later in the project to determine whether this theory is applicable to our system. The LISA model considers the film exiting the injector as a 2D viscous, incompressible liquid sheet of thickness *2h*, moving through a motionless gas medium. The last atomization stage involves secondary breakup models, which depend on the specified nature of the flow. The LISA model combines the sheet breakup and atomization phase into one.

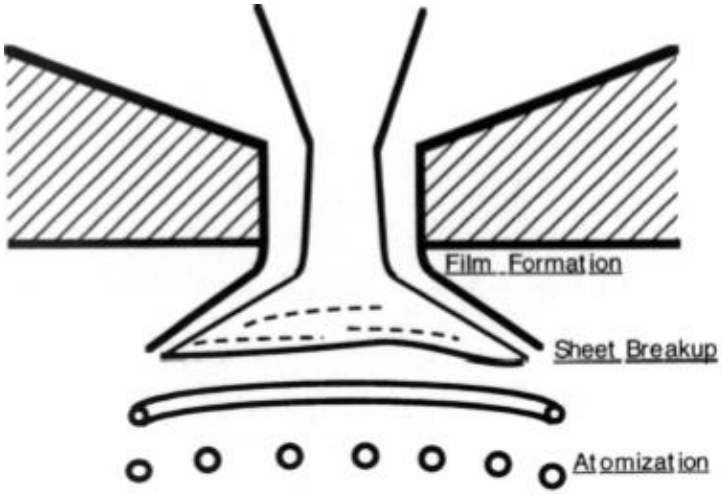

Figure 4.5 A sketch of the transition of fluid to external spray, also showing the three stages of the LISA model (105).

When using the pressure-swirl atomizer, the relationship between the injector and spray must be acknowledged. The LISA model operates using the following assumptions:

- Hollow cone spray forming;
- Droplets are generated at the injector according to the Rosin-Rammler size distribution, which describes the volume of the particles as a function of their diameter;
- Mean diameter value predictions can be extracted during post-processing;
- Droplets are uniformly distributed in the spray cone;
- The injector flow rate is assumed to be steady;
- The atomized particles appear at the point of injection immediately;
- The slip velocity between the liquid sheet and the surrounding air is equal to the absolute velocity of the liquid near the injector ($V_s \equiv V_f$).

The absolute velocity magnitude of the liquid (V_f), is related to the injection pressure head Δp by

$$V_f = |V_f| = k_v \sqrt{\frac{2\Delta p}{\rho}}; \quad (129)\ (4.30)$$

where $k_v$is the velocity coefficient and ρ is the density and Δp the pressure difference. The fluid film model is now introduced.

4.7.4. Using the fluid film model

The fluid film model in Simcenter STAR-CCM+ allows us to provide a mathematical description of the behaviour of the cellular suspension deposited in the inner surface of the eye as a result of spraying. In this thesis we will

specify the properties for the initial layer of film, formed at the inner surface of eye, which is defined as wall. The injector is defined with the Lagrangian Multiphase model and a Film-Lagrangian Phase Interaction model with impingement.

To work with the fluid film model, firstly we define the fluid film phase by creating desired phase models and a shell region to subsequently initialise the film. By activating the fluid film model, the solver calculating the properties of the fluid is also activated. The fluid film properties such as its thickness, shear stress and surface velocity are field functions that can be post-processed. Once activated, the fluid film phase needs to be defined by creating a fluid film phase, selecting the models to define the problem, selecting the material properties and customising them if need be. The fluid- film phase is defined to have constant density, laminar flow and the same fluid properties as the liquid sprayed into the eye.

Firstly, the multiphase interaction model is selected, followed by the Film-Lagrangian phase interaction. Secondly, the properties of the Film-Lagrangian phase are then to be assigned. We define the fluid film continuum to interact with the Lagrangian phase and vice versa. The impingement model is then selected. The fluid- film boundary condition is set as such that an additional fluid- film and wall boundaries are automatically added. This type of boundary allows all the droplets from the Lagrangian phase to be converted into fluid- film. The stick physics mode is then activated to allow the sprayed droplet to attach at the retinal wall; is to allow the droplets to stick at the surface of the wall to simulate a gel-like behaviour. The multiphase interaction model is used to define how the fluid and gas phases interact with each other and contains sub-models predicting conservation of mass, momentum and energy between the two phases. We create a phase interaction between the Lagrangian phase and the fluid-film phases. This phase interaction allows us to predict and define the relationship. In summary, the physics models selected to set up the simulation are as follows

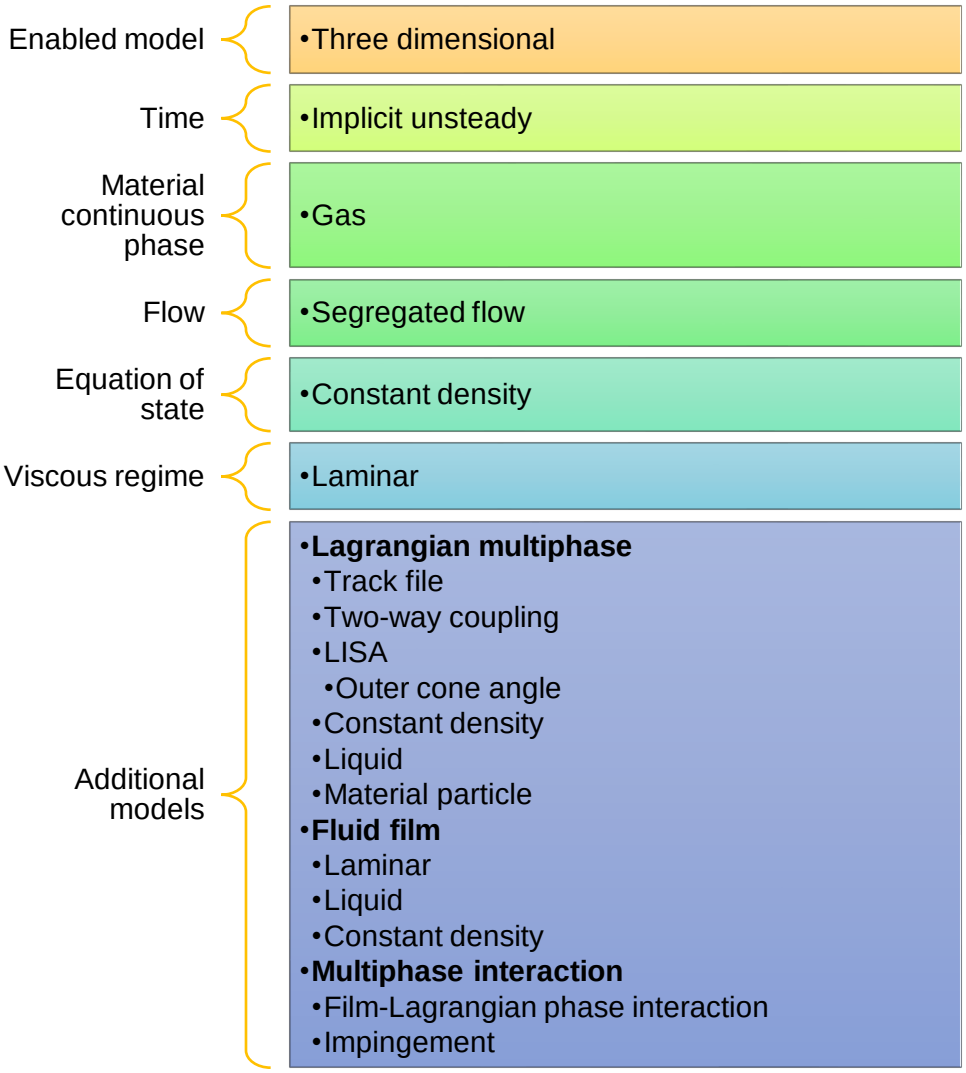

Figure 4.6 Order of physics models selected in Simcenter STAR-CCM+.

4.8. Results

4.8.1. Convergence study

To determine an appropriate mesh element size, a convergence analysis was carried out on the 3D human eye model. To generate the mesh as described in Section 4.7). The mesh was initially creating using the minimum number of elements to analyse the model, using an edge element size of 2.0 mm. The mesh edge element size was initially reduced by increments of 0.2 mm between the sizes of 2.0 and 1.0 mm, and reduce further by increments of 0.1 mm between edge element size of 1.0 and 0.1 mm. Here we observe how parameters such as thickness of the cell-laden hydrogel at the retinal wall (referred as fluid film thickness) varies through mesh refinement. We present the data when the cellular scaffold is sprayed at a volume flow rate of 200 µL/s and an external pressure of 25 kPa applied at the injector; with a specified outer cone angle of 50°. Convergence with respect to Figure 4.7 was achieved at the edge element size of 0.4 mm.

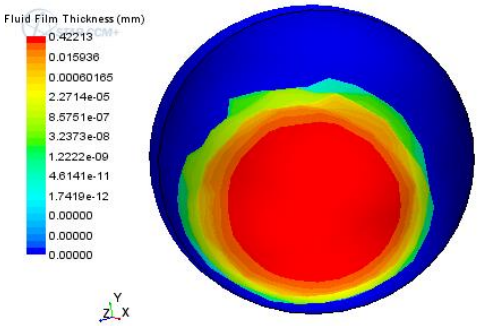

(a) edge element size of 2 mm

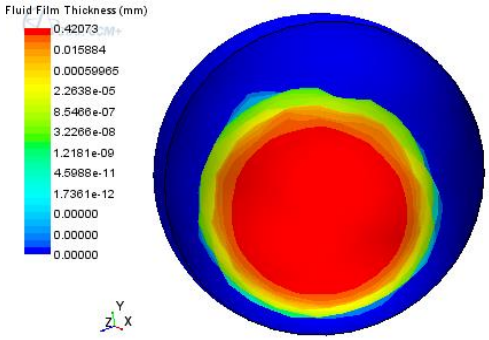

(b) edge element size of 1.8 mm

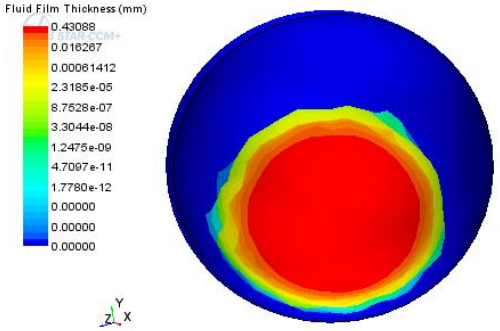

(c) edge element size of 1.6 mm

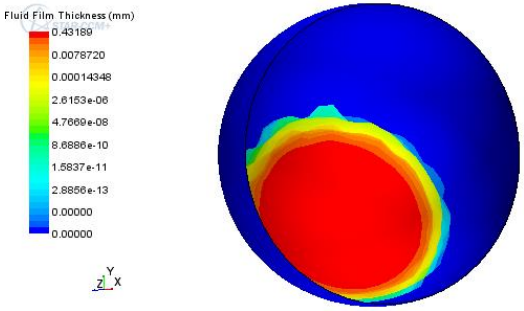

(d) edge element size of 1.4 mm

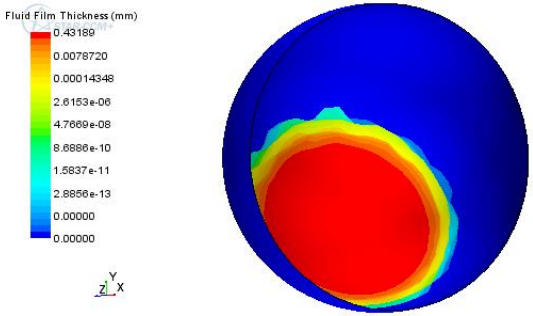

(e) edge element size of 1.2 mm

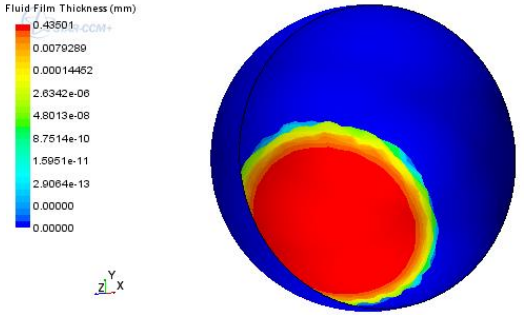

(f) edge element size of 1 mm

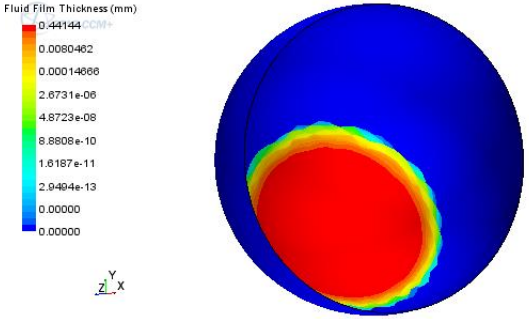

(g) edge element size of 0.9 mm

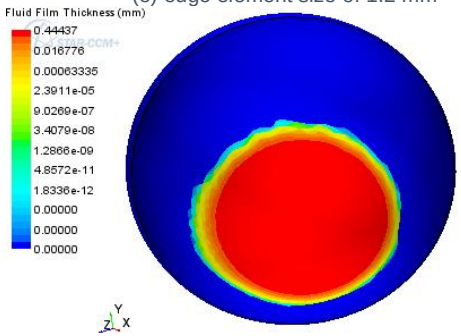

(h) edge element size of 0.8 mm

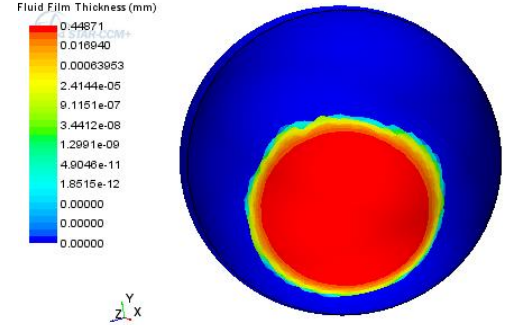

(i) edge element size of 0.7 mm

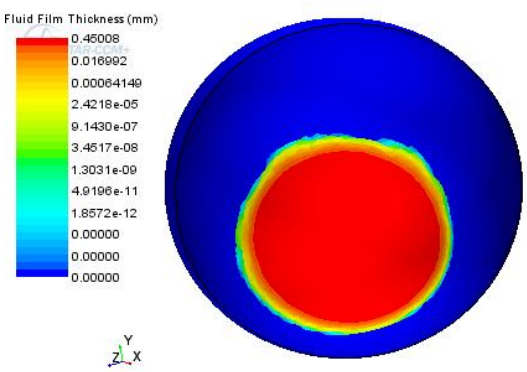

(j) edge element size of 0.6 mm

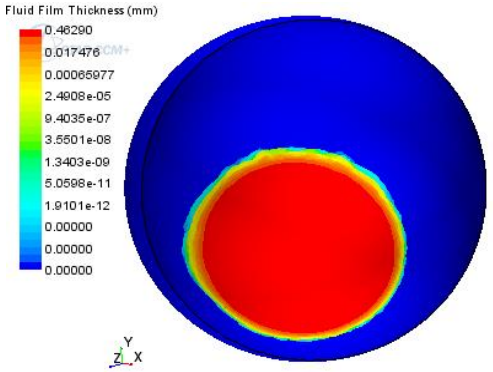

(k) edge element size of 0.5 mm

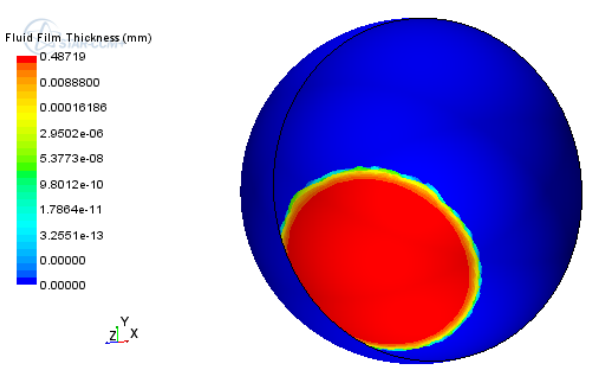

(l) edge element size of 0.4 mm

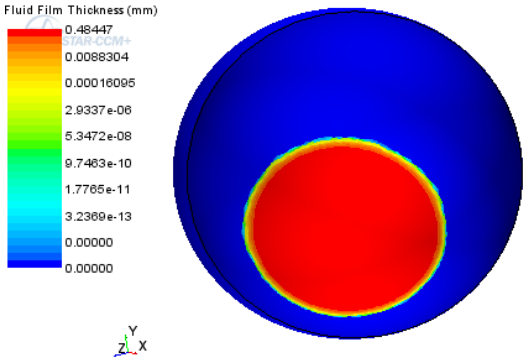

(m) edge element size of 0.3 mm

Figure 4.7 Distribution of thickness of the sprayed cell-laden hydrogel at the retinal wall (referred to as fluid film thickness) using various edge element size, varied between 2.0 to 0.3 mm. The film thickness was obtained upon spraying the cellular suspension onto the inner retina at a spraying duration of 1s at a pressure of 25 kPa and outer cone angle of 50°. The illustrations show an increase of the total thickness of the cell-laden hydrogel at the retinal wall with reduced edge element size.

4.8.2. Simulation predictions

The CFD solver Simcenter STAR-CCM+ is used to define the material properties for the cell-laden hydrogel sprayed onto the retina.

The spray system is intended for spraying cells that can be attach to the retina, such as Müller glial cells. Müller glia are structurally supportive cells, have a very high metabolic function and are very resilient to stress. Neurons are very sensitive to physical and metabolic damage and the spray is not intended for use with neurons.

Droplets' speed is predicted when applying different pressure conditions at the injector nozzle with a constant volume flow rate, also applied at the nozzle. We also inspect the droplets' speed when varying the volume flow rate of the cellular scaffold, with a constant pressure at the injector. We derive relationships between volume flow rate and air pressure supplied. Different volume flow rates are observed at different pressure conditions (Table 4.2) to evaluate output parameters, namely thickness of the cellular scaffold at the retina wall, droplets spatial distribution and retinal surface area are assessed. The external pressure was kept constant, whilst volume flow rates were varied from 100 to 400 µL/s. this procedure was repeated for pressures of 10, 25, 50, 75 and 100 kPa. The surface area of the inner retinal wall is controlled by the outer cone angle which is defined with the nozzle properties. The outer cone angle was therefore varied from 5° to 100°.

The region of interest at the retina wall to evaluate droplet speed and wall shear stress at the retina wall, is inspected by creating a threshold region with specified film thickness values, then highlighting the region of interest. Although both shear and normal stresses should communicate influence on cell population; this thesis focuses on shear stress to demonstrate the model's behaviour. The threshold region is then specified as part when creating the

histogram. This data is also used to determine the average film thickness at the retina wall at various conditions.

We then plot a histogram showing thickness distribution of the cellular scaffold over the inner retinal wall as shown in Figure 4.12, showing the number of elements (Frequency, x-axis) within the specified region of interest at the retina wall, against the predicted thickness band for the cell-laden hydrogel at the retinal wall (Fluid Film Thickness/mm, y-axis). The elements represented in the histogram, reflect the elements within the region covered by droplets spatial distribution from the retinal wall. This predicts maximum and minimum values for thickness of cell-laden hydrogel at the retina wall.

4.8.3. Droplets' speed and wall shear stress on the retinal surface

The speed of sprayed cell-laden hydrogel droplets can be tracked in space (see Figure 4.8). The model adopts Han et al's theory (129) also defined in Chapter 3. The droplet speed varies with increasing pressure at the injector (see Figure 4.7); with a percentage difference varying between 14.9 and 35% in the tracked droplet speed at pressure conditions of 10, 25, 50, 70 and 100 kPa. For example, the maximum droplet speeds at a pressure of 25 kPa and 50 kPa, have a 25% difference (4790 mms^{-1} and 6890 mms^{-1} respectively), whereas the droplets speed at 50 and 70 kPa have a percentage difference of 14.9% (6890 mms^{-1} and 8910 mms^{-1} respectively). As such, there appears to be a positive correlation between the air pressure and the magnitude of the droplets speed.

During a spraying event we can extract wall shear stress magnitude at the retinal wall upon impact between hydrogel droplets and the retinal surface, by creating a threshold region (see Figure 4.8(a)). Cells may be damaged as a result of shear with increasing external air pressure at the injector; not only as a result to the impact, but also as a result of shear cells are subject to during

a spraying event. As cells perception of mechanical forces is still poorly understood (130), there remains a challenge to quantify these forces experimentally; one option to advance this research could be introduce cell viability after aerosolization under same pressure conditions and volume flow rates used in the computational model. However, as we can only predict shear stress magnitude at the retinal wall after the impact at the retina, there remains the limitation of predicting the shear stress magnitude during a spraying event.

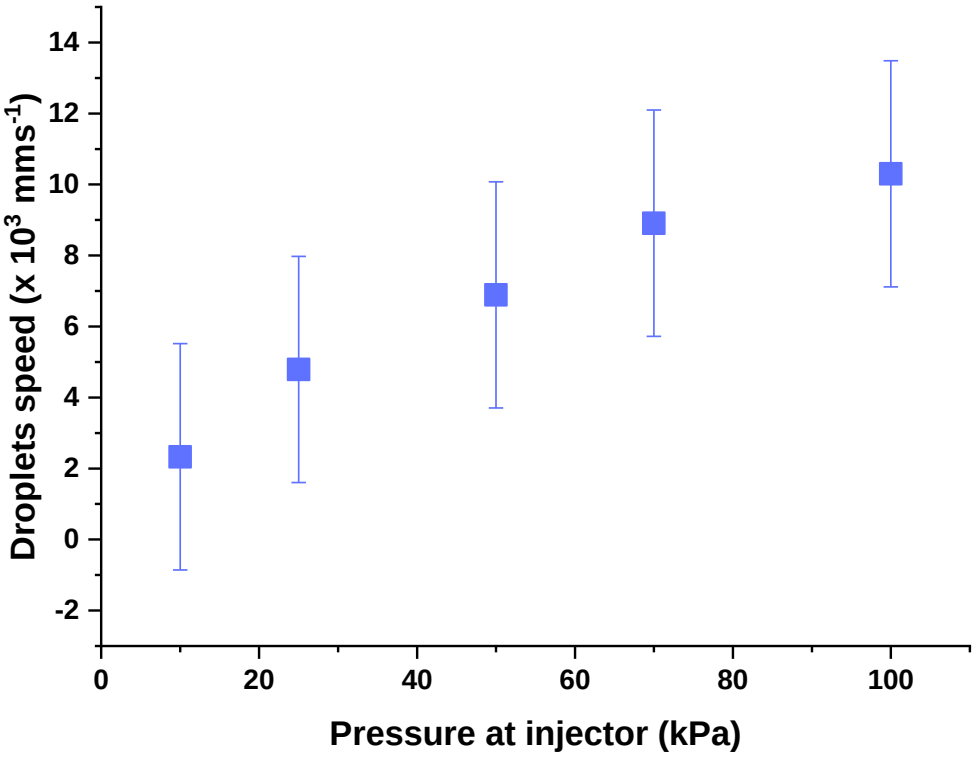

Figure 4.8 Mean and variability in droplet speed on the retinal surface for varying injector pressure (volume flow rate and outer cone angle held fixed at 400 µL/s, 50° respectively; error bars +/- 2 standard deviations from the mean).

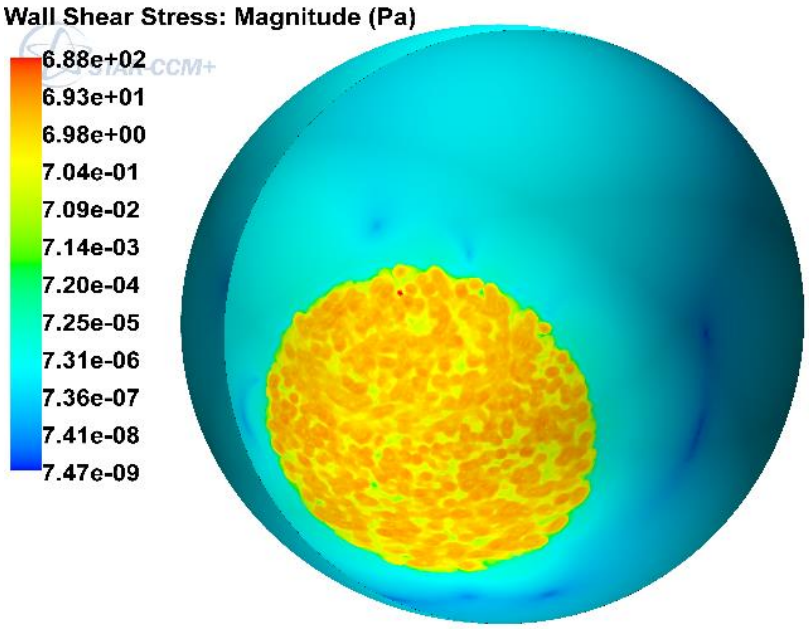

(a)

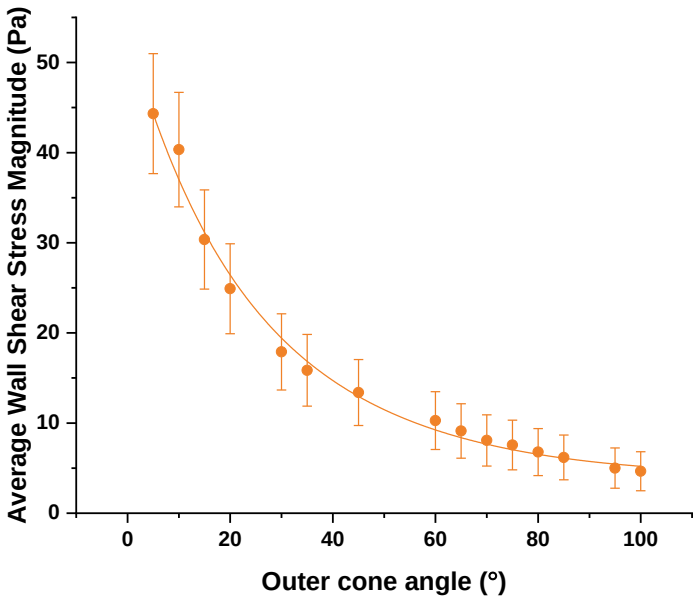

(b)

Figure 4.9 (a)The retinal surface is sprayed with volume flow rate of 250 µLs^{-1} at a pressure of 25 kPa The region of the retinal wall covered with the hydrogel, referred as threshold, is used to calculate the average wall shear stress (WSS) magnitude at the retinal wall. (b) The cellular scaffold is sprayed at a volume flow rate of 400 µL/s at a pressure of 100 kPa at the injector. We present WSS magnitude values covering different surface area at the retinal wall, expressed through outer cone angles 5° to 100° (n=3 repeats, R^2=0.80, p < 3.13x 10^{-6}).

4.9. Spatial distribution of cellular thickness distribution at the retinal wall

The coloured mapping of the model shows a logarithmic scale for the thickness of the sprayed cell layer. These figures capturing the logarithmic scale suggest the volume of the cellular scaffold is sprayed and appearing layered, thus showing homogeneous distribution. Figure 4.10 shows the cellular suspension sprayed on the retina. The film thickness of the cellular suspension is represented using a logarithmic scale and it shows the homogeneity of the sprayed cellular scaffold. A similar result is also described in the literature as a result of a similar experimental protocol (67,79).

According to Figure 4.9, the thicknesses of the cell-laden hydrogel sprayed on the retinal surface is examined at varying flow rates (from 150 to 275 μLs-1) with the inlet pressure fixed at 10 kPa, and cone angle fixed at 50°. The thickness of the layer is broadly uniform, and film thickness increases with increased volume flow rates, as expected (see Figure 4.10). The thickness of the cellular scaffold at the inner retinal wall is also observed at varying flow rates and fixed pressure inlet. The pressure is kept fixed at 10 kPa, whilst the volume flow rate is varied from 150 to 275 μLs^{-1}. It is predicted for the increase in film thickness at the retina to be directly proportional to the increased volume flow rate.

Secondly, we plot a histogram showing thickness distribution of the cellular scaffold over the retinal wall as shown in Figure 4.12, showing the number of elements (Frequency) within the specified region of interest at the retina wall, against the calculated thickness band (Fluid Film Thickness/mm). The elements represented in the histogram, reflect the elements within the region covered by droplets spatial distribution from the retinal wall. This performed by identified maximum and minimum values for the parameter in question (in the case the maximum film thickness) we create a threshold region with the sprayed retinal surface.

The maximum film thickness for each spraying event are shown in Figure 4.11, as a function of volume flow rate and injector pressure. As such, it can be concluded that the mean thickness at the retina wall is significantly affected by the pressure supplied at the injector. Increasing the external air pressure at the injector nozzle appears to have a positive impact by increasing the overall fluid film thickness and releasing finer droplets (129). Nevertheless, we could argue there are other factors influencing mean film thickness, such as aerodynamic forces and force applied at the plunger when releasing the mixture, which currently can only be controlled manually. Introducing an automated device that would control the forces applied at the plunger (by manipulating input parameters), will help specify desired outputs from the computational model. It is therefore possible to derive relationships for spraying parameters (see Figure 4.10). These parameters could be used to predict operating relationships that enable a desired thickness on the retina to be achieved. For example, the exponential relationship between maximum film thickness (*y*) and volume flow rate (*x*) at 10 kPa in the form of $y = Ae^{B}$ as:

$$y = 0.30e^{0.004x}. \tag{4.3}$$

If we desire a thickness of 1.5 mm using an injector pressure of at 10 kPa, inverting this equation indicates the cellular suspension should be sprayed at 400 μLs^{-1}. Exponential relationships at different pressure conditions are presented on Figure 4.11, and the relationship between their coefficients A and B is also defined. We use an equation to define the latter as shown in Figure 4.12 (*y = 0.014 -0.035x*). This helps not only to correlation coefficients relationship, but to possibly introduce an alternative method for predicting outputs such as desired film thickness at the retinal wall, for future spraying condition which were not observed in this thesis, but could be investigated as future work.

There remains existing limitation associated with named identified factors influencing film thickness. For example, it is currently challenging to quantify aerodynamic forces and forces applied at the plunger. However, with the introduction of mathematical modelling providing an insight for future design

of spray systems, it is hoped that future research will support deriving these predictions.

It is vital highlighting that increasing the pressure at the nozzle, may introduce damage to the underlying retinal tissues and cells. A standardised computational model where the chosen external pressure and applied volume flow rate promote cell viability and cell proliferation, could be introduced in the future. It is hoped these values will be dependent on the geometry of the damaged organ, its location and the surface area of the damaged tissue needing treatment. Using the data obtained from the various fluid film thickness plots, we will now proceed to calculate the average thickness of the cellular suspension over the surface area of the inner retina within the sprayed region.

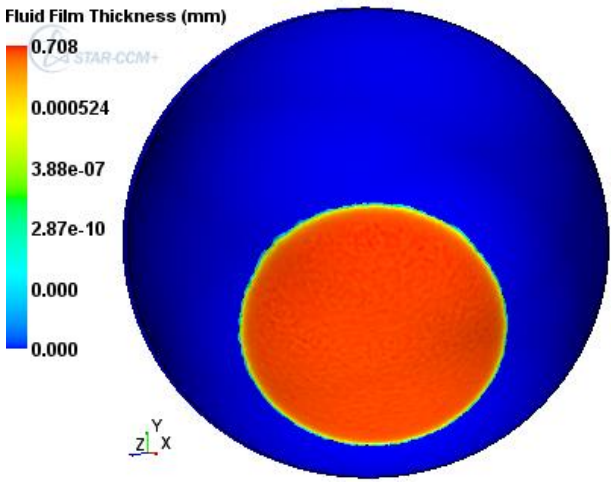

(a) 150 µLs-1

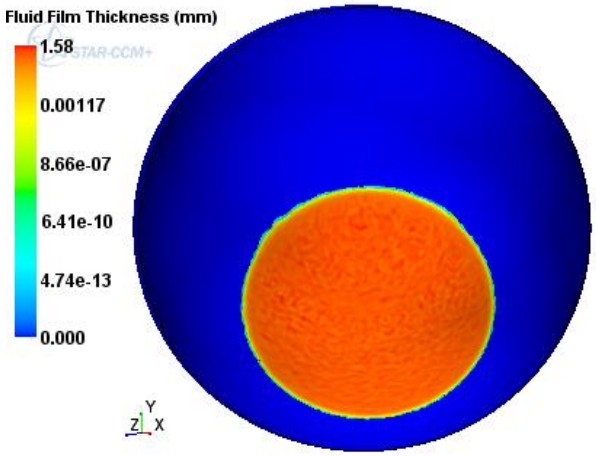

(b) 200 µLs-1

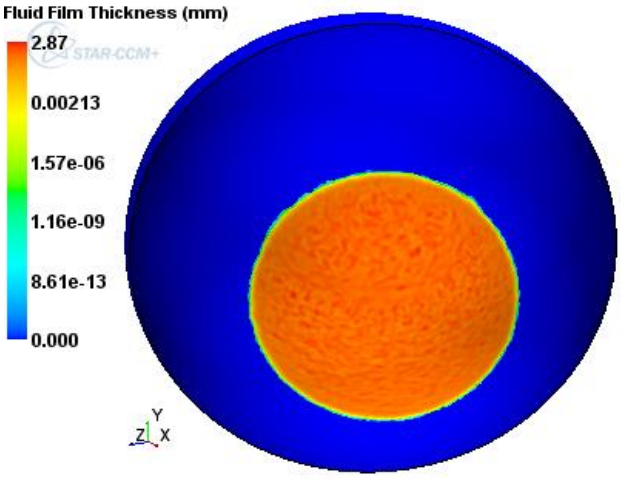

(c) 275 µLs-1

Figure 4.10 Logarithmic scale of fluid film thickness distribution on the retina, with varying volume flow rate between 150 to 275 µLs-1, at a constant pressure condition of 10kPa at the injector and an outer cone angle of 50°.

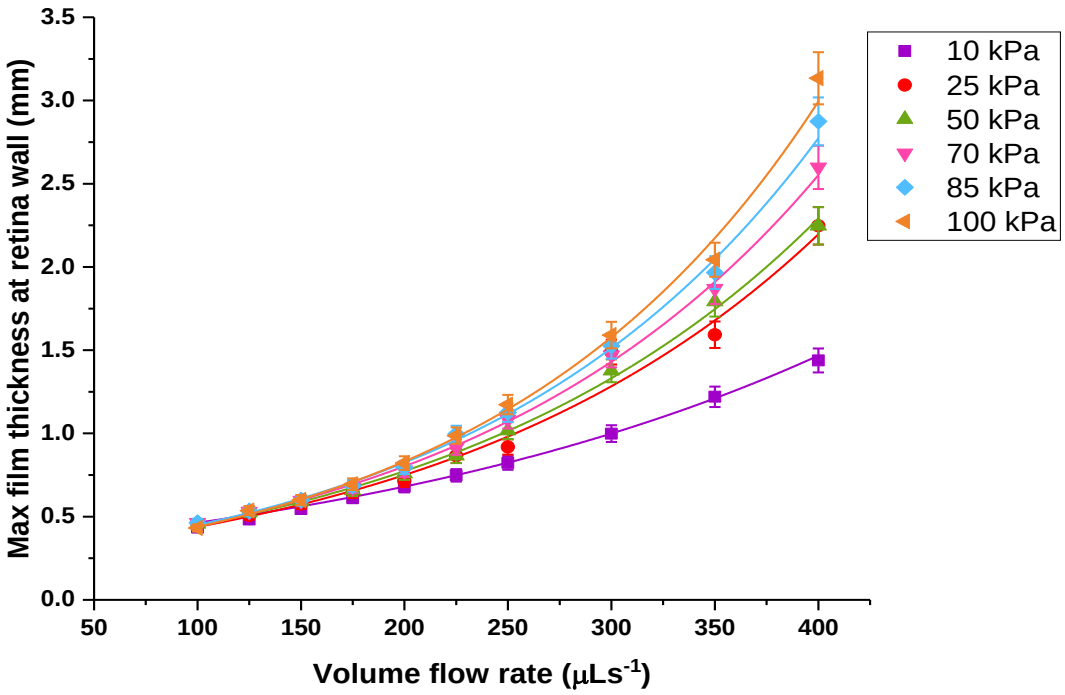

Figure 4.11 The maximum film thickness at the retina surface (y-axis) has an exponential relationship with the volume flow rate (x-axis), for each given pressure value and at an outer cone angle of 50°. Data points show the mean, and error bars +/-1 standard deviation from the mean when averaging across the spatial domain. Lines show fitted exponential relationship based on defined relationships in Table 4.4 with R^2 values for each regression line (ranging between 0.91 and .98) summarised in Table 4.3.

Table 4.4 Exponential relationships linking maximum film thickness (mm, y) with volume flow rate (μL/s, x), at different inlet pressures, as summarised in Figure 4.11. R^2 values quantify the variation of maximum film thickness at the retina wall, accounted by the variation in volume flow rate.

Pressure/ kPa	Equation	R^2	Coefficient A	Coefficient B
10	$y = 0.30e^{0.004x}$	0.98	0.30	0.0040
25	$y = 0.26e^{0.0054x}$	0.93	0.26	0.0054
50	$y = 0.26e^{0.0054x}$	0.95	0.26	0.0054
70	$y = 0.25e^{0.0058x}$	0.94	0.25	0.0058
85	$y = 0.24e^{0.0061x}$	0.92	0.24	0.0061
100	$y = 0.23e^{0.0064x}$	0.91	0.23	0.0064

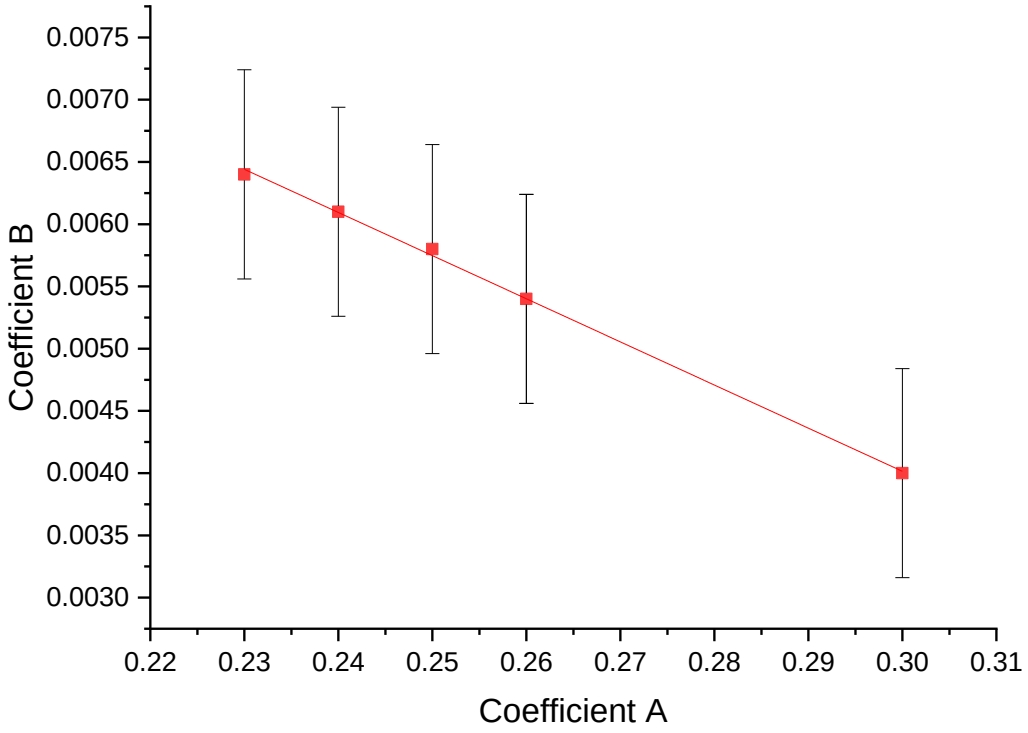

Figure 4.12Coefficents A and B relationship defined as y = 0.014 -0.035x (R^2=0.99). This relationship can be used to predict future empirical equations for other pressure conditions which could be investigated in future research.

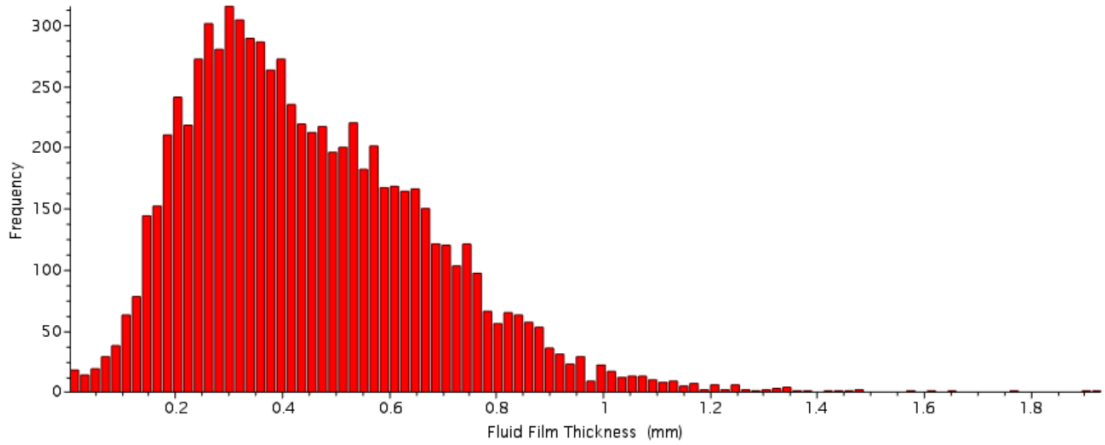

Figure 4.13 A histogram of film thicknesses by CFD elements. Here we present film thickness distribution at the retina l wall, with outer cone spraying angle of 50°, volume flow rate of 200 µL/s and external pressure of 25 kPa applied at the injector.

4.10. Covered surface area of the retina

The surface area covered by the spray system is dependent on the cone angle used to spray the cells (see Figure 4.11). We can derive an exponential relationship between the covered surface area of the inner retina and the defined outer cone angle (R^2 =0.99). The outer cone angle used to spray the cell suspension can also be used to specify the desired surface area of the retina, needing spraying. The error bars are determined for the calculated surface area values at the retina wall. The surface areas calculated with an outer cone angle of about 80° or more, captures more data points compared to other outer cone angles less than 80° (hence offering a greater platform for cell proliferation). Here we assume the outer cone angel of the sprayed hydrogel is mixed with the cells. However, we are yet to validate this experimentally. Nevertheless, it was also possible to define the relationship between the covered surface area and outer cone angle, which could be used on the retina to predict the required cell population for each treatment, whilst acknowledging dimension of retina stem cells.

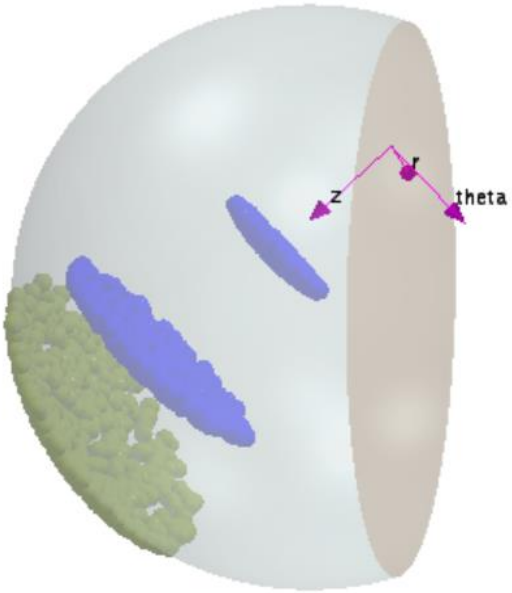

Figure 4.14 The 3D eye model with a diameter of 25 mm; and a demonstration of how the droplets' spatial and temporal distribution are tracked in time, at an outer cone angle of 30°, with the z-axis representing the direction of the trajectory of the sprayed droplets.

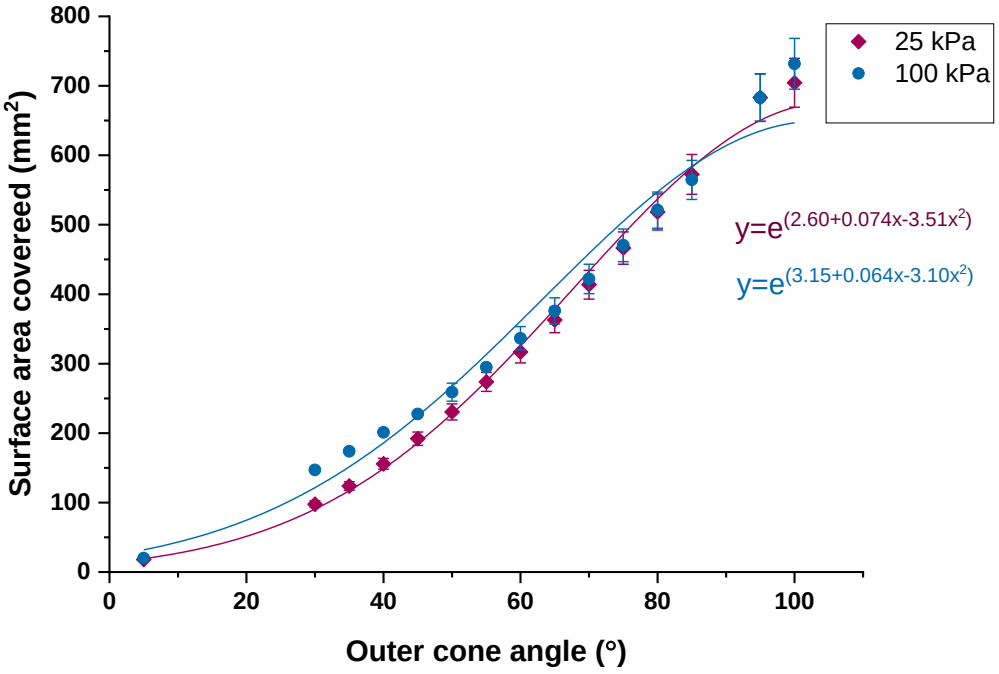

Figure 4.15 Relationship between surface area covered and outer cone angle, varying between 5° to 100°, using volume flow rate of 250 µL/s at 25 kPa and 400 µL/s at 100 kPa. Data points indicate average values for 3 repeats and and error bars +/- 1 standard deviation of the mean.

4.11. Droplets dimension

According to the results, at a higher pressure of 100 kPa, it is predicted there will be a finer droplets distribution, with droplets mean diameter of 170 µm, compared to the peak mean diameter of 180 µm at 70 kPa and 325 µm at a pressure condition of 25 kPa. The droplet size distribution is characterised not only be external pressure applied at the nozzle, which determine the hydrogel's velocity in terms of both magnitude and direction. We predict droplet dimension at the retina wall. Simcenter STAR-CCM+ uses the Rosin-Rammler distribution to define droplet dimensions through the Linear Instability Sheet Atomization (LISA) model. Results show the Rosin-Rammler model assumes droplet size distribution are uniformly distributed as a cone-like spray pattern. The range of droplets dimension is statistically displayed in Figure 4.16, Figure 4.17 and Figure 4.18 using a cumulative distribution function, where the frequency represents the volume flow rate, droplet volume or number of droplets using the Rosin-Rammler distribution function (65). This function is defined as

$$F(D) = 1 - exp\left[-\left(\frac{\mathrm{D}}{\mathrm{D_{ref}}}\right)^{\mathrm{q}}\right]; \tag{4.4}$$

Where $F(D)$is the cumulative distribution function, D_{ref} is the mean diameter for the simulation results (also referred to as peak diameter or the Rosin-Rammler), D is the droplet diameter value and *q* is the Rosin-Rammler exponent. this theory describes the volume distribution of hydrogel droplets as a function of their diameter. The cumulative distribution function represents the mass fraction of droplets with a dimeter value between zero and one, assuming we have an infinite number of droplets. The droplet size distribution described in terms of constant *q* that provides a measure of the spread of droplet size. Its value generally lies between 1.5 and 4 the higher the q value, the more uniform the spray. Here we use a value of 1.5. The Rosin-Rammler distribution function It allow data to be extrapolated into a range of fine droplets, where measurements are mostly difficult to derive experimentally.

The cumulative distribution function also gives a number of droplets with given diameter D, and we now show examples of how to use this equation.

Let us take into consideration from Figure 4.16 where we apply a volume flow rate of 200 µL/s and a pressure of 25 kPa at the injector nozzle; we want to quantify the percentage of droplets with a diameter of 150 µm. we therefore rewrite the equation as follows:

$$F(D) = 1 - exp\left[-\left(\frac{150}{325}\right)^{1.5}\right] = 0.269.$$

Therefore 30% of the cell-laden hydrogel droplets at the retinal wall have a diameter of 150µm.

We try another example, by considering Figure 4.17, where we maintain a constant volume flow rate of 200 µL/s and an external pressure of 70 kPa. For a diameter of 250 µm, we calculate as follows:

$$F(D) = 1 - exp\left[-\left(\frac{250}{180}\right)^{1.5}\right] = 0.805.$$

Therefore, approximately 80% of the cell-laden hydrogel droplets at the retinal wall have a diameter of 250 µm.

As a result, the Rosin-Rammler function not only is used for mathematical simplicity, ease of manipulation in computations, but the above data and could be used for future research do develop further numerical equations, which predict droplets size distribution at the retinal wall for varying pressure conditions and if implementing a higher measure of droplet size spread *q,* which could ultimately evaluate numerical value for obtaining finer droplets at the retinal wall.

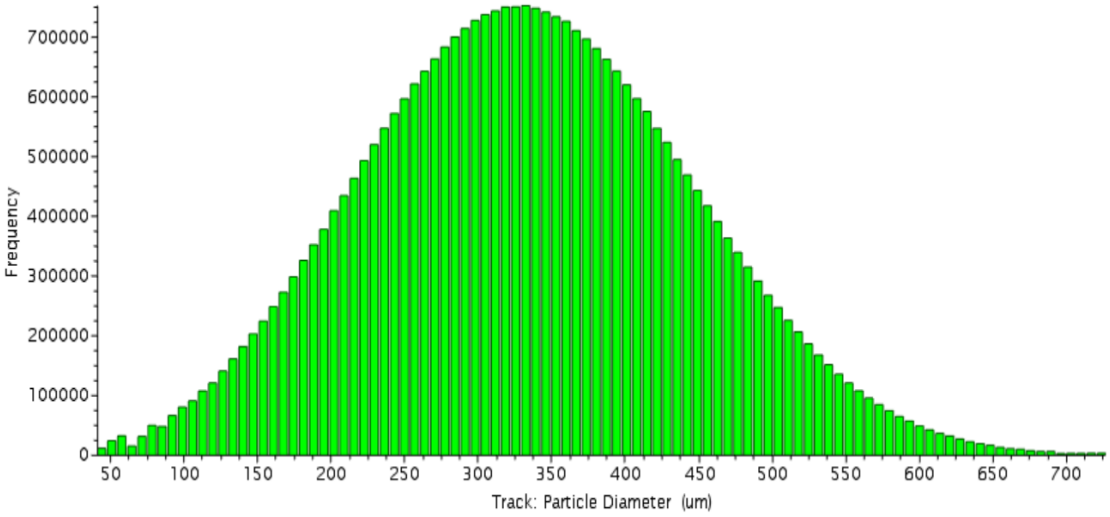

Figure 4.16. The cellular scaffold is delivered at 200μL/s, with a pressure of 25 kPa at the injector. Droplet size distribution at the retina wall using the Rosin-Rammler cumulative distribution function, with a diameter peak value of about 325 μm and an outer cone angle of 50°.

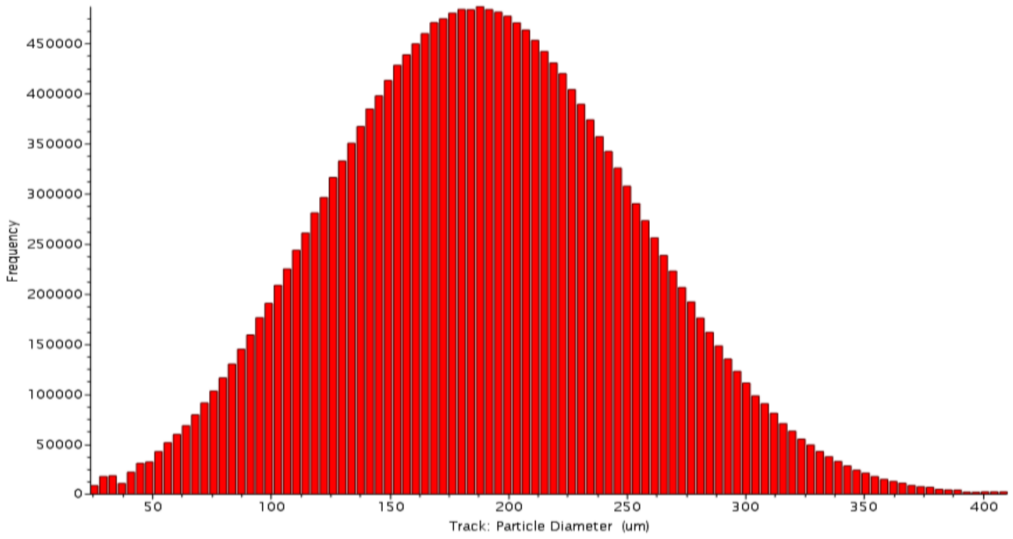

Figure 4.17 The cellular scaffold is delivered at 200μL/s, with a pressure of 70 kPa at the injector. Droplet size distribution at the retina wall using the Rosin-Rammler cumulative distribution function, with a diameter peak value of about 180 μm and an outer cone angle of 50°.

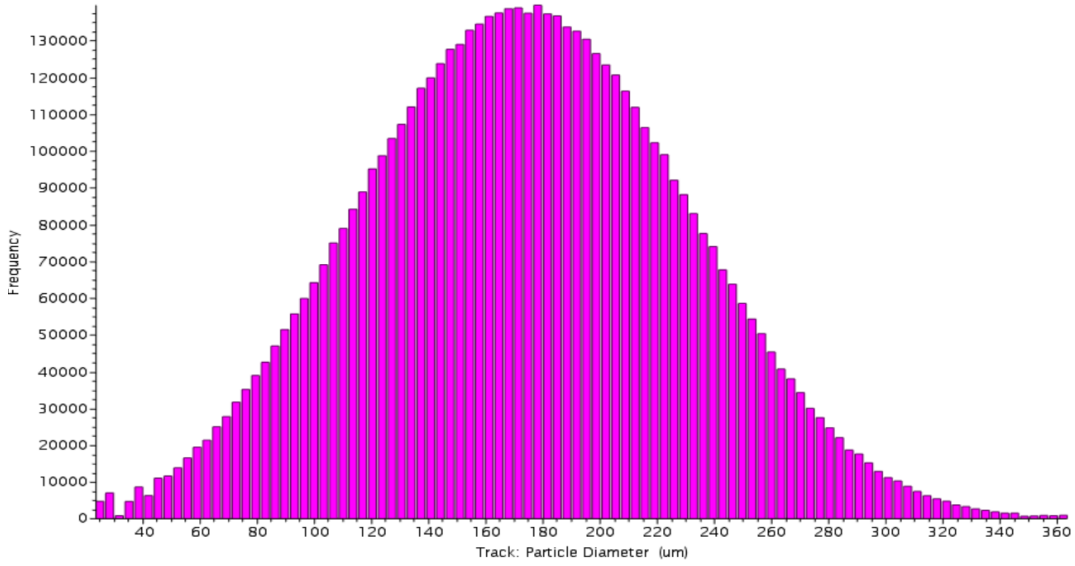

Figure 4.18 The cellular scaffold is delivered at 200μL/s, with a pressure of 100 kPa at the injector, with reduced parcel number. Droplet size distribution at the retina wall using the Rosin-Rammler cumulative distribution function, with a diameter peak value of about 170 μm and an outer cone angle of 50°.

4.12. Discussion

In this Chapter, computational modelling is used to predict spatial distribution of cell-laden hydrogel droplets, controlling surface area of the inner retina during a spraying event and droplet dimension. The fibrin-derived hydrogel is used as vehicle to aid cell delivery onto the inner retina, to ultimately explore the impact of varying spraying parameters (pressure and volume flow rate at the injector nozzle, outer cone angle for the spray) on key outputs of high priority, namely the spatial distribution of the delivered hydrogel on the retinal wall, the surface area of the retina covered, and droplet speed.

To derive a sensible compromise between accuracy and computational time, a convergence study was initially carried out by establishing a suitable edge element size to discretize the geometry of the human eye. The mesh refinement was also used to evaluate predictions for cumulative thickness of cumulated cellular suspension at the inner retina. The range of pressures used were based on the Baxter spray system and a recent study in the literature (67,70). The predictions showed that different volume flow rate, require different external pressure to achieve the desired thickness of the cellular suspension. Such relationship could be used to instruct operating parameters for cell-based therapies for retinal degenerative diseases, specifically glaucoma. As such, parameters could be closely tuned to control cell delivery during a clinical application.

This could hopefully be assisted by introducing patient-specific parameter relationships. For example, depending on patient-specific eye geometry and stage of retinal degeneration, we could tune the external air pressure and volume flow rate for the cellular scaffold to reach a desired thickness at the retina using the suggested parameter relationships developed in this research. Nevertheless, there is the need for validating these predictions experimentally.

Theoretically, high pressures are known to support a homogeneous distribution (67); however, the applied volume flow rate also plays a vital role on the overall thickness of the sprayed cellular scaffold at the retinal wall and cell viability. Nevertheless, by acknowledging the delicate nature of the human retina, and lens to vitreous ratio in the human eye as seen in Figure 2.8, organ-specific pressures need to be derived to support cell viability. Thus far, published literature outlines pressure conditions suitable for rodents' eye, of which eye to lens ratio promoted the use of high pressures such as 100 kPa or higher (70). This unfortunately cannot be used in humans due to anatomical differences compared to rodents. It is therefore hoped that relationships established in this research using mathematical modelling, will help predict suitable pressure and volume conditions for the human retina and possibly used for future research.

Mathematical modelling supports the understanding of physical phenomena within a system by suggesting theories to make predictions. The application of stem cells using the existing spray systems in the market, remains a challenge for most of the anatomical structures, specifically the human eye. Mathematical modelling therefore aims to help save time and cost before conducting animal testing. As a result, introducing mathematical modelling as an imperative protocol for cell-based therapies, could reduce the number of animal test that would need to be carried out. Mathematical modelling would help guide and ultimately lead to a standardised procedure in defining organ-specific spraying parameters for cell-based therapies, which will be specific to each organ to be transplanted with stem cells.

With known pressures and volume flow rates, the surface area is determined by the outer cone angle for aerosolization. For example, with a cone angle of 50°, the surface area covered is of about 211 mm^2. Figure 4.15 shows an exponential relationship between the spraying outer cone angle and the surface area covered. Using this data and knowing the dimension of the eye in need of stem cell delivery, a clinician could be able to predict the cone angle

required to cover the region of interest. As such, adopting this method for parameter prediction will serve useful in replicating such method for other degenerating organs and tissues around the body; by estimate the surface area needing spraying (using numerical values such as organ dimension).

To facilitate the design of organ-specific spray systems, computational modelling was introduced to create a virtual replica of prospective future surgical technique for cell-based therapies, simulating aerosol spraying into the inner retina of the human eye. Aerosol technology was adopted with the hope to support retinal stem cells delivery into the human eye, as a potential therapy to treat glaucoma. Through mathematical modelling we could develop a computational design of tissues and organs undergoing transplantation and obtain results comparable to *in-vivo* experiments at a reduced time, cost and reduced health and safety risks compared *to in*-vivo experimental studies (80). In this thesis, realistic measurements were taken into consideration such as human eye dimensions (with a diameter of 25 mm), proposed volume flow rate of cellular scaffold (ranging between 100 and 400 μL/s), and external pressure to be applied at the injector nozzle (which was varied between 10 and 100 kPa).

The cellular scaffold was sprayed onto the retinal wall in a fast and controlled manner. Such technique is known to accelerate the healing process of damaged tissues, as spraying of cells directly to the affected area is one delivery mechanism that has shown to promote cell viability and proliferation (66,67). On this basis and acknowledging the link between the observed cell spraying output (such as surface area covered, droplets spatial distribution film thickness and droplets velocity magnitude) and input (air pressure at nozzle, volume flow rate of cellular suspension and nozzle dimension), computational modelling appears to be a significant tool to inform these relationships by promoting organ-specific application for cell delivery.

The simulations indicate that the surface area covered can be controlled by predicting the outer cone angle for spraying the cellular suspension (R^2 = 0.99). With the aim of covering a larger inner surface area of the retina, based on the data predicted, a suitable cone angle should not be lower than 80° (see Figure 4.15). This will ensure the large area of the inner retina and the macula are covered, during the proposed cell-based treatment. The spatial distribution of the cellular scaffold is also dependent on mathematical spray models adopted. Perhaps, it could be ideal observing other injector models available on Simcenter CCM+ requiring other parameters such as droplet dimensions and droplet velocity, hitherto compare the obtained output. In addition, we are also able to inspect droplet size distribution at different pressure conditions; the higher the external pressure at the injector nozzle, the finer the droplets, which in compliance with previous literature findings (67). We quantify percentage of droplets with a specific diameter size at the retinal wall. Such relationship could be employed in future studies to define further parameters to instruct finer droplets at the retinal wall.

Applying lower pressures compared to the range used in this thesis (pressures less than 10 kPa), might also be an advantage to reduce cell death, which was encountered in the literature (67). Despite the success of designing potential injectable hydrogels in Chapter 3, there are existing challenges that might stand as barrier for cell viability post aerosolization. Firstly, although mechanical stresses can influence cell physiology, cellular response remains challenging to quantify and knowledge of the mechanical influence of sprays on different cell types remains scarce (131). During aerosolization, cells can also be damaged by air bubbles; the extent of cell damage depends on the cell type, level of shear stress and exposure to shear (131). Nevertheless, it is worth emphasising that applying external pressures is prescribed as input from existing spraying systems for larger organs, such as the skin. We are yet to determine whether applying higher pressure values at the injector would be beneficial for human ophthalmic spraying applications, and whether the absence of the pressure at the injector would help us achieve desired results.

Some studies have explored cell viability and proliferative capacity after aerosolization, but have demonstrated high variability in cell viability (between 37% and 94% (67)). This variability is hypothesized to be due to the range of different hydrostatic, elongation and shear stress that cells are exposed to, as well as uncontrolled factors such as changes in cells' cycle and ions leakage following lysis.

Cell delivery onto the retina is hoped to be achieved by injecting hydrogel with cells. If the cellular scaffold is known to ease the application of cell onto the retina, it acts as a supportive vehicle where cells are seeded *in-vitro* and combined with growth factors that will help *in-vivo* differentiation and promote tissue repair (68). We desire for cells to be released at rates whereby the rheological properties of the hydrogel are supporting and promoting the cell proliferations process, before undergoing degradation. However, these rates are yet to be quantified and have been a challenge in previous research (131).Findings form these Chapter, highlight potentials for mathematical modelling to predict these rates, hence opening doors for future research.

However, this introduces an outstanding question on how the surface area to be covered can be controlled experimentally. Perhaps, variable interchangeable injector nozzles may be introduced to spray the region of interest. With the view of informing cell delivery parameters and ease of parameter manipulation, computational modelling also appears to be an alternative method to minimise costly ad time consuming experimentation. With the intention of outlining additional actions to enhance the current findings, experimental assessment of derived spraying parameters is now discussed.

5. Experimental Assessment of Spraying Parameters

In this Chapter, an experimental assessment is carried out to evaluate the influence of the spraying parameters identified in Chapter 4 on spraying outputs. Specifically, the link between volume flow rate and nozzle pressure, and the surface area of the retina covered is explored. In addition, cell viability is assessed in order to hypothesise the link between nozzle flow rate, induced shearing stresses on the cells, and the cell response to these stresses. First of all, the experimental methods are presented, followed by the results and conclusions.

5.1. Cell culture

Müller stem cell lines MIO-M1 from the UCL Institute of Ophthalmology were used in this research (6). Cells were passaged by creating monolayers of cultured cells and dissociated using 3ml of TrypeIE ^{TM} 1X (Life technologies), and incubated for 5 minutes at 37°C, with 5% CO_2. Cells were cultured in a flask containing Dulbecco's Modified Eagle Medium (DMEM) x 1 with GlutaMAX with 10% Foetal Calf Bovine Serum (FCS) (Invitrogen, UK) and Penicillin/ Streptomycin (10000 units per 5ml in the T-25 flask). Cell suspensions were centrifuged at 1400 rpm for 5 minutes at 15°C.

5.2. Cell Spraying

The procedure carried out in Section 5.1 was used to culture to prepare the cells for aerosolization. Müller stem cell lines MIO-M1 were once again passaged by creating monolayers of cultured cells and dissociated using 3ml of TrypeIE^{TM} 1X (Life technologies), and incubated for 5 minutes at 37°C, with 5% CO_2. Cells were cultured in a flask containing Dulbecco's Modified Eagle Medium (DMEM) x 1 with GlutaMAX with 10% Foetal Calf Bovine Serum (FCS) (Invitrogen, UK) and Penicillin/ Streptomycin (10000 units per 5ml in the T-25 flask). Cell suspensions were centrifuged at 1400 rpm for 5 minutes at 15°C. After centrifuging the cells, the excess media is removed, and the cells

are suspended into a volume of 1.32 mL of thrombin and PBS. ad loaded into the Baxter Healthcare System syringes for spraying. The thrombin and PBS combined with the MIO-M1 cells are loaded separately from the fibrinogen, which was also diluted into PBS (150 µL of thrombin mixed with 1.17 mL of PBS, hence giving a total volume of 1.32 ml). The Baxter spray system was then connected to the external pressure regulator, where the desired pressure was applied (50, 70 and 100 kPa) and the cell laden hydrogel was sprayed onto a 6-well plate at a distance of 2 cm from nozzle to the sprayed surface.

Once sprayed, the cell-laden hydrogel was stained with trypan blue, to inspect cell viability of MIO-M1 cells post-aerosolization. Experiments were conducted to assess surface areas post-aerosolization by spraying the fibrin-derived hydrogel, oil and water at pressure of 50, 70 and 100 kPa respectively. Each fluid was stained with trypan blue and sprayed onto filtered paper in a petri dish. The sprayed filtered sheets were scanned and processed for imagining on ImageJ Software, to calculate the areas covered. We also use this technique to assess the covered area of the retinal surface predicted with the computational model, by inspecting surface area coverage on a petri-dish with filtered paper. Although the outer cone angle for each spraying event could not be measured experimentally, we employ this comparison (together with data from Chapter 4) to predict outer cone angle values following cell spraying.

As mentioned, we assess spraying on a flat surface, by applying the following pressure conditions at the nozzle; 50, 70 and 100 kPa using the Baxter Healthcare spraying System. Spraying distance and volume flow rate are kept fixed at 2 cm and 400 µL/s respectively, in correlation with the computational model. The surrounding temperature is also maintained at 37°C. We test spraying with water, emulsion oil, fibrin derived hydrogel without the cells and with the cells also, to explore the influence of material rheology on spraying surface area sprayed, which is used as spraying output. The same protocol is then reapplied to spray the cultured cells with the fibrin-derived hydrogel on a 6-well plate.

5.3. Results

5.3.1. Surface area covered

Figure 5.1 compares the average surface area covered for different nozzle pressure conditions and fluids, for fixed volume flow rate of 400µL/s. Firstly, it is clear the fluid rheological properties are a high contributing factor to the surface area covered. For example, the viscosity of the fibrin-derived hydrogel (varying between 3Pa. s and 9 Pa. s) is greater than that of water (8.9×10^{-4} Pa.s), due to combination with the matrix. There is therefore a significant difference in the surface areas covered at the same nozzle pressures. By comparison, emulsion oil, fibrin-derived hydrogel and its cellular counterpart have a similar viscosity and display similar surface area trends.

Secondly, let's explore results for surface area (SA) covered when spraying the fibrin-derived hydrogel and the cell-laden hydrogel (see Figure 5.1) . Figure 5.1(B) compares more closely SA covered using the produced hydrogel, with and without the MIMO1 cell line. For example, the SA covered when spraying the hydrogel only at 100 KPa (1771.21 mm^2) is approximately 3 times greater than the SA covered at 70 KPa and 50 kPa (553.72 mm^2 and 549.77 mm^2 respectively). Similarly, comparing SA covered with cells and hydrogel mixed, results show a coverage of 1806.63 mm^2 and 657.55 mm^2 at 100 kPa and 70 kPa respectively.

This works as an advantage for results previously obtained in Chapter 4 for the mathematical modelling, where mathematical predictions and rheological properties in the model are implemented with the assumption that cells and hydrogels are mixed. We can also observe that higher pressure at the injector resulted in greater surface area coverage at the surface. However, this was not the case with the mathematical predictions (see Chapter 4); with the mathematical model, the outer cone angle was defined and used to define the

surface area for spraying. Such relationship cannot be imposed experimentally and to the best of our knowledge techniques to impose such instructions are still undergoing development and require further research. This highlights the need for further advances in technology and robotics to introduce an automated system to instruct a desired surface area to be covered. This will ultimately help clinicians manipulate spraying inputs by specifying desired output parameters; hence controlling retinal surface area needing treatments.

A

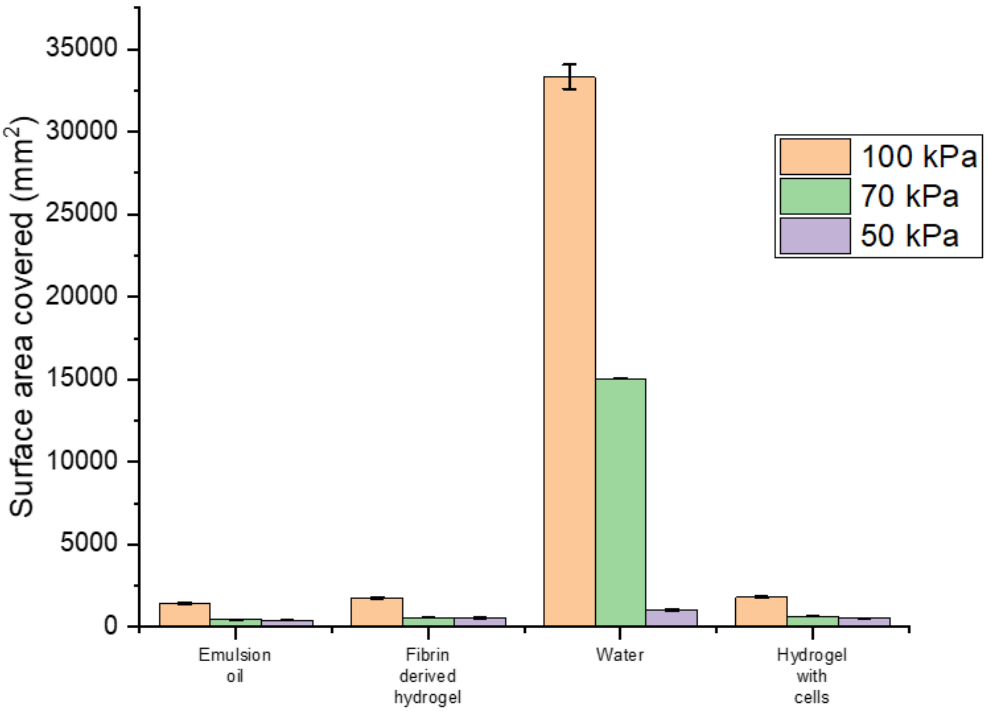

B

		Pressure conditions at the injector/ kPa		
		100	**70**	**50**
Surface area covered /mm²	**Hydrogel only**	1771.21	553.72	549.77
	Hydrogel with cells	1806.63	657.55	535.60

Figure 5.1 (A) Column graph showing surface area covered (mm², y-axis), which was assessed experimentally post-aerosolization(error bars +/- 1 standard deviations from the mean). Spraying was conducted at three pressure conditions (50, 70 and 100 kPa) using the Baxter Healthcare spraying system. Each fluid is sprayed at a volume flow rate of 400 µL/s for on a petri dish covered with filtered sheet. The covered surface is calculated using ImageJ software. The data indicates average values for the surface area covered and the error bars representing standard deviation averaged over 3 repeats, and later summarised to closely look at the surface area sensitivity of surface area covered at different pressure conditions with the cell-laden hydrogel (B).

5.3.2. Cell viability

Here we present cell viability post-aerosolization using the cell-laden hydrogel and spraying parameters as described in the Methods section. Cells are sprayed at a fixed volume flow rate of 400 µL/s. Live/ dead staining using trypan blue was conducted (see Figure 5.2) using a Leica TCS-SP2 confocal microscope using a 20x oil immersion objective lens. Image were processed through the Leica AF Lite Confocal Software, prior to further analyses through ImageJ. Each experiment is repeated three times; examples of dead cells are identified with red arrows and live cells, with green arrows (see Figure 5.2, Figure 5.3 and Figure 5.4). The cell-laden hydrogel was sprayed onto a 6-well plate. At a pressure condition of 100 kPa, cells showed 93 % viability (see Figure 5.2 and Figure 5.5). At 70 kPa there was a viability of 91%, whereas at 50 kPa cell viability reduced to 83%. Collectively, these data show a high rate of cell survival within this pressure range. The results indicate that, within the range tested, the higher pressures gave rise to higher cell viability. There are numerous mechanisms which could give rise to this trend, for example the cells may respond positively to shear stimulation, or the increased pressures may increase the probability of attachment to the surface upon spraying.

With a positive correlation of air pressure and droplets speed predicted in Chapter 4, we could suggest this positive correlation has a positive impact on cell viability *in*-vitro. Although we are unable to measure film thickness of sprayed cell-laden hydrogel experimentally, our mathematical prediction suggests cells had enough surface area on the plate, which promoted their survival post-aerosolization. We previously hypothesised reduced viability as a result of increased external pressure at the injector nozzle, however, these experimental data state the contrary. In addition, having finer droplet as a result of higher-pressure conditions as shown in Chapter 4, may therefore be an advantage for rapid cell delivery onto the region interest. There is indeed high cell viability at higher pressure values, however their survival after several

weeks cannot be quantified in this study, but open doors for future studies to observer their survival and possibly proliferation.

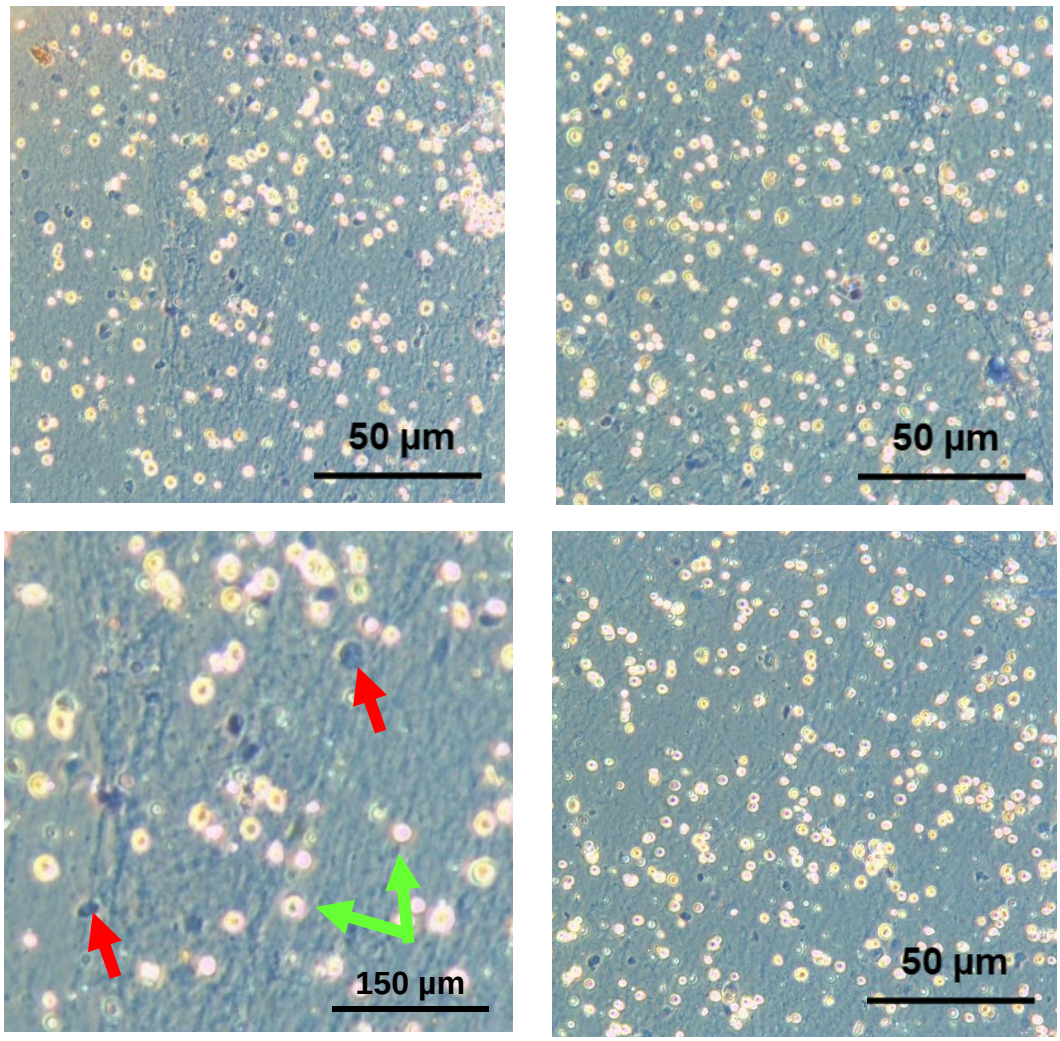

Figure 5.2 Viability of Müller stem cells sprayed with the Baxter Healthcare Easyspray system at pressure of 100 kPa using trypan blue staining using a Leica TCS-SP2 confocal microscope at 20x magnification. Images were processed through Leica AF Lite Confocal Software and ImageJ for further analyses. After being cultured, cells are mixed with the fibrin-derived hydrogel (with a thrombin concentration of 0.08U/mL) and sprayed at a volume flow rate of 400 µL/s on a 6-well plate and applying an external pressure of 100 kPa and the second inlet of the spraying device. The sprayed cell laden-hydrogel is then coated with 50 µL trypan blue, diluted into 200 µL of PBS. The red arrows indicate the dead cells and the green arrows the live cells (scale of 50 µm). The experiment was repeated three times.

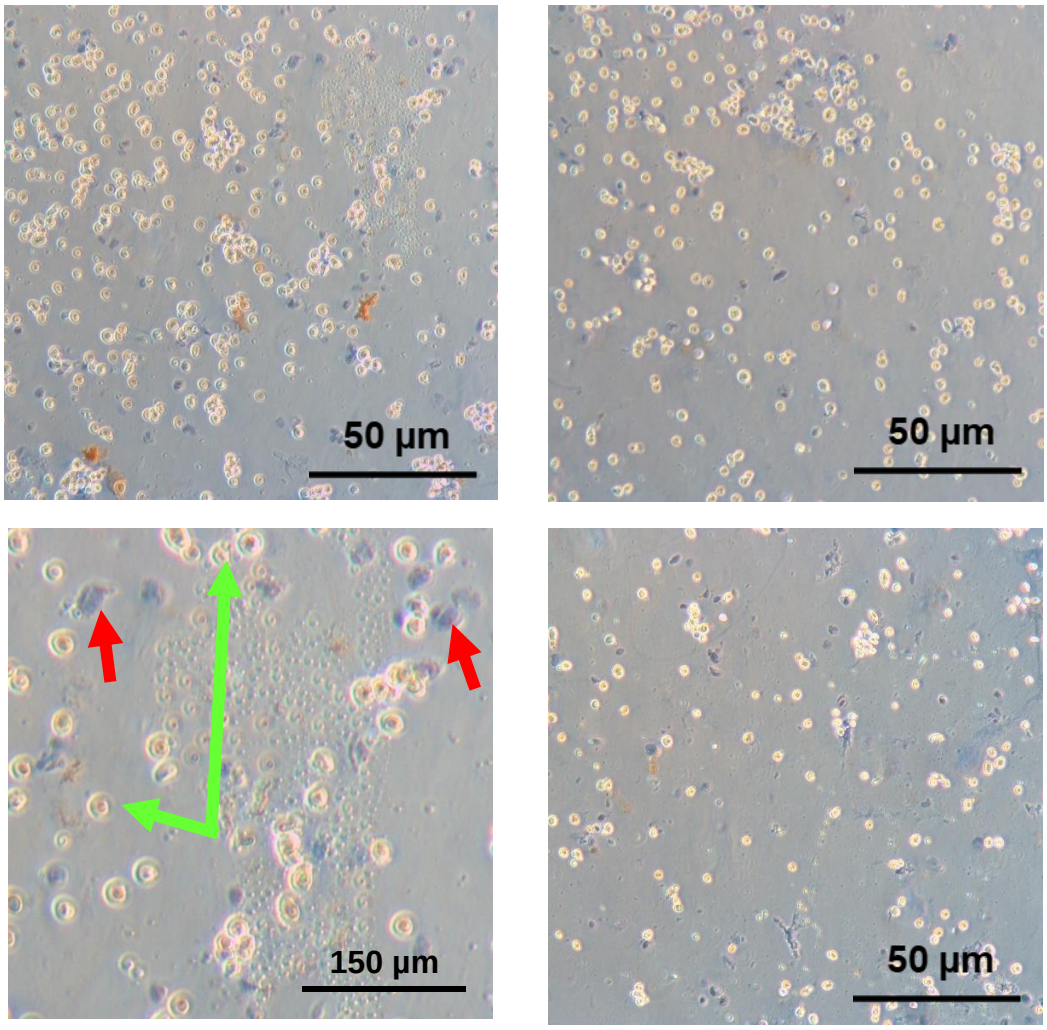

Figure 5.3 Viability of Müller stem cells sprayed with the Baxter Healthcare Easyspray system at pressure of 70 kPa using trypan blue staining using a Leica TCS-SP2 confocal microscope at 20x magnification. Images were processed through Leica AF Lite Confocal Software and ImageJ for further analyses. After being cultured, cells are collected using fibrin-derived hydrogel (with a thrombin concentration of 0.08U/mL) and sprayed at a volume flow rate of 400 µL/s on a 6-well plate and applying an external pressure of 70 kPa and the second inlet of the spraying device. The sprayed cell laden-hydrogel is then coated with 50 µL trypan blue, diluted into 200 µL of PBS. The red arrows indicate the dead ells and the green arrows the live cells. Images were taken at 20x magnification. The experiment was repeated three times.

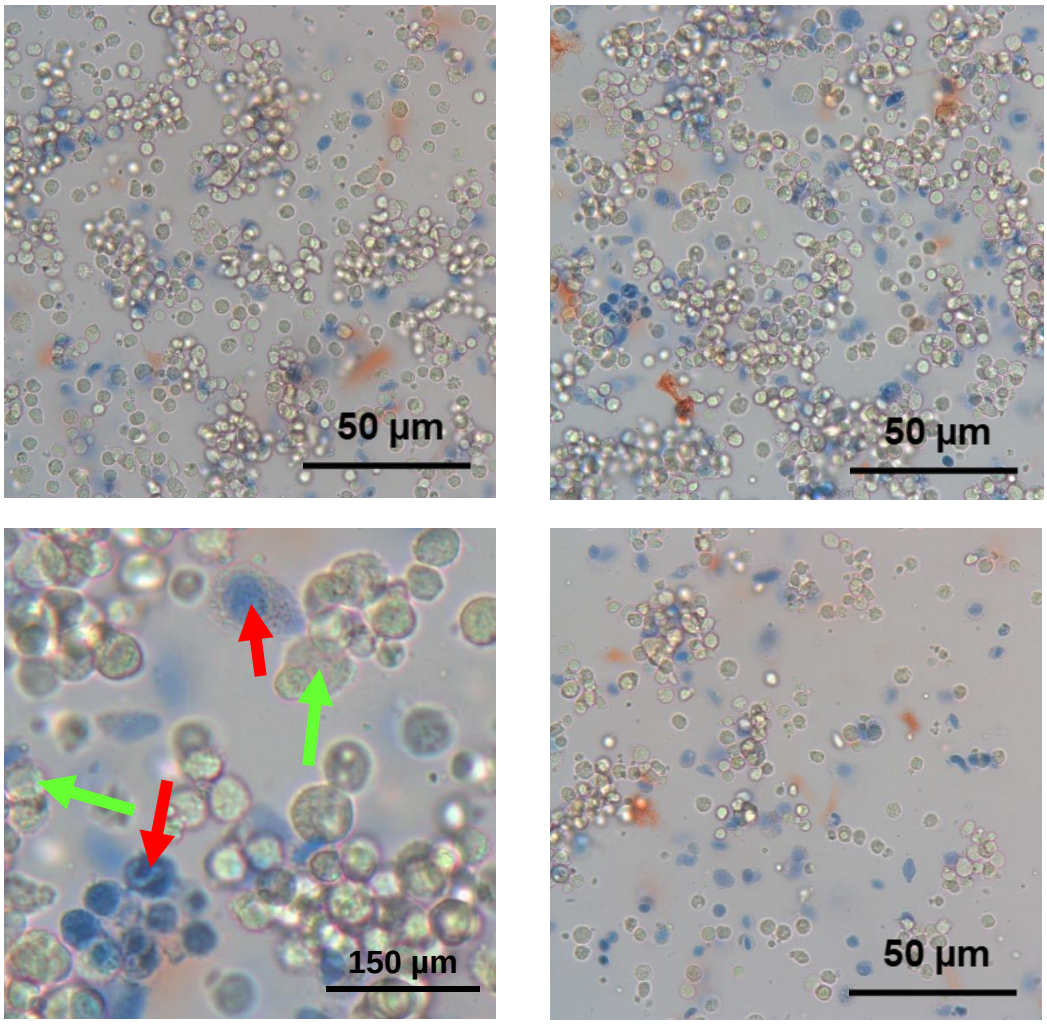

Figure 5.4 Viability of Müller stem cells sprayed with the Baxter Healthcare Easyspray system at pressure of 50 kPa using trypan blue staining using a Leica TCS-SP2 confocal microscope at 20x magnification. Images were processed through Leica AF Lite Confocal Software and ImageJ for further analyses. After being cultured, cells are collected using fibrin-derived hydrogel (with a thrombin concentration of 0.08U/mL) and sprayed at a volume flow rate of 400 µL/s on a 6-well plate and applying an external pressure of 50 kPa and the second inlet of the spraying device. The sprayed cell laden-hydrogel is then coated with 50 µL trypan blue, diluted into 200 µL of PBS. The red arrows indicate the dead ells and the green arrows the live cells. Images were taken at 20x magnification. The experiment was repeated three times.

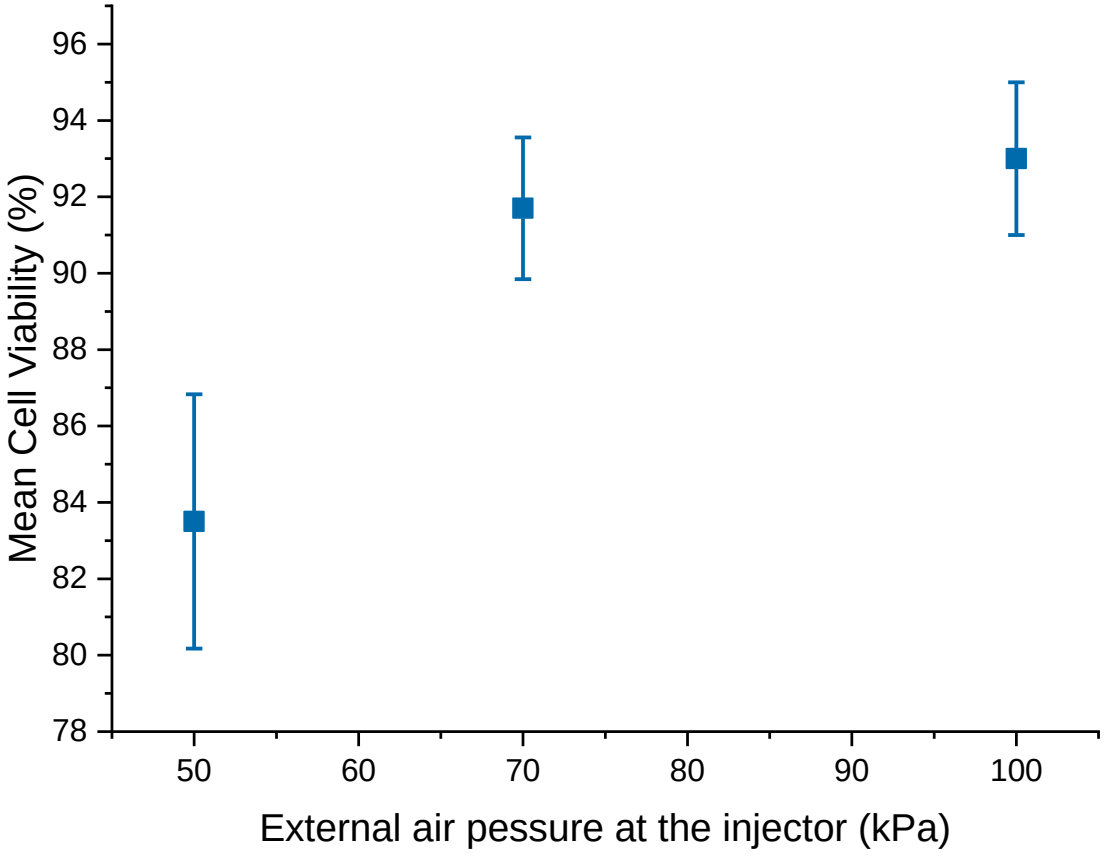

Figure 5.5 The mean cell viability of the sprayed Müller stem cell lines MIO-M1 (5 million cells) with the pressure at the injector (x-axis) sprayed at a volume flow rate of 400 µL/s on a 6-well plate with the fibrin-derived hydrogel, with constant fibrinogen concentration (0.5 mg/mL). Data points show the mean cell viability, with error bars representing the standard deviation based on n=3 repeats (p<0.38).

5.4. Discussion

This Chapter aimed to experimentally assess the influence of spraying parameters on outcomes of the spraying process. Data showed that cell viability post-aerosolization was achieved at good levels at all pressures tested of 50, 70 and 100 kPa. Despite the success achieved in cell viability, these figures are unable to predict cell survival after spraying, which will be required to confirm impact of the cell-based therapies in the distant future and confirm cell proliferation. As the external pressure at the injector nozzle decreased, cell viability also decreased; to the best of our knowledge it is currently challenging to identifying relationship between reduced pressure condition and cell death. Literature suggest aerodynamic forces as contributing factor; however, it could also be highlighted that linking reduced pressure at the injector, signifies reduced droplet speed for the cell-laden hydrogel droplets, increasing the chances for cell death. Yet, the cell viability achieved at the lowest pressure investigate (50kPa) could still be satisfactory to achieve cell proliferation and hopefully restoring functions for the diseased retinal tissue.

The shear stresses acting on cells are as result to pressure difference within the spraying system and jet formation may be causes of potential cell damage; together with other unknown factors. For example, if we assume a laminar flow of the cellular suspension flowing from the syringe through to the nozzle, the tension within the cells may resist the elongation stresses due to the aerosol spraying. It is difficult to determine a range of stress magnitude that may cause cell rapture, as lower stress exerted following changes in cell cycle and leakages of certain ions may also cause further damage to cells. Cell viability after aerosol spraying should therefore be considered together with cell proliferative capacities. Stem cells can be exposed to shear forces, which should be tightly controlled to promote cell survival post aerosolization (132). For example, shear forces can be controlled when using bioreactor systems and strictly control environmental conditions during bioprocesses.

If the hydrogel degrades too quickly, some of its properties could be lost; if it degrades too slowly, the degradation process could interfere with the cell proliferation.

Cells perception of mechanical forces is still poorly understood (130). Hemodynamic forces play an important role in regulating cell structure and function in the surrounding environment. The effect of fluid shear stress, can induce stem cell differentiation; various cell types possess the property of altering their shape and function as a response to mechanical forces acting on them (shear stress and stretching tension) (133). When subject to fluid shear stress, cells become elongated, with the axes aligned in the flow direction and secretion of vasodilation substances increases. When cells are suspended in cultured in medium, they are subject to hydrostatic, shear and elongation stresses (134). However, hydrostatic stresses are not enough to predict cell damage as cells may deform or rotate due to strain effects. Pressure difference in the spray system and jet formation, together with other unknown factors may contribute towards shear stresses exerted on the cells. Elongation stresses also occurring through a laminar flow, may stretch the cells and cause further damage.

6. Conclusion and Future Recommendations

The main contribution of the research described in this thesis is the use of mathematical modelling for deriving spraying parameters for stem cell delivery into the human retina. This thesis aims to ultimately inform the development of aerosol spraying systems to deliver retinal stem cells into the eye. This Chapter reviews the collective conclusions from each Chapter to evaluate whether the objectives have been addressed.

6.1. Review of objectives

The objectives of the first research Chapter (Chapter 3), involved characterising mechanical properties of several fibrin derived hydrogels, which could act as potential injectable material and cellular scaffold. The rheological properties of four fibrin-derived hydrogel mixtures (with varying thrombin concentrations and constant fibrinogen dilution) were successfully quantified using a rheometer. Perhaps, the hydrogel mixtures developed in this thesis could be implemented as benchmark scaffold for developing ideal cellular scaffold for stem-cell delivery. The rheological properties of the chosen hydrogels are incorporated into the computational model of the human eye developed in Chapter 4, to simulate aerosolization of the cellular scaffold and its delivery onto the retinal surface.

The objective of Chapter 4 was to develop spraying parameter relationships using a prescribed range of input parameters, namely volume flow rate of cell-laden hydrogel (100 to 400 μL/s) and external air pressure applied at the injector (10 to 100 kPa). This Chapter used mathematical modelling to describe the spraying process based on a 3D model of the human eye using realistic adult eye dimensions sought from the literature. Spraying outputs such as surface area of the inner retina covered, maximum film thickness at the wall, wall shear stress magnitude at the retinal wall and droplet speed were investigated at the different pressure conditions. Values for the pressure inlet were gathered from existing literature. A mesh convergence study was carried

out to determine an appropriate mesh element size to obtain accurate solutions. In defining the developed 3D eye model, associate mathematical theories were assigned for each fluid phase, and the material properties of fibrin derived hydrogel were inputting as parameters into the computational model.

The limitation of this technique led to further experimental assessment for the influence of spraying parameters (see Chapter 4); complimentary validation of the identified relationships is sought experimentally. The covered surface area of the inner retina is measured using the ImageJ software. Outputs such as droplet size at different pressure conditions were suggested for further analyses for future work. Chapter 5 employs experimental assessment as a tool to evaluate cell viability by imposing boundary conditions and parameters from the computational model; possibly quantifying and establishing a relationship between cell viability and wall shear stress magnitude previously calculated at the retinal wall.

6.2. Overall aim

The results from this thesis have shown that a combination between mathematical and experimental testing techniques can provide a clearer picture and guide for development of an aerosol spraying system for cell-based therapies to treat retinal degenerative diseases in humans, with the hope of scaling up such a procedure for larger organs around the human body. These techniques introduced can be employed to investigate several output parameters that could contribute toward successful spraying delivery of stem cells and promote cell viability and proliferation. However, validating output parameters experimentally could face limitations with practicality and how to specifically quantify cell viability against wall shear stress magnitude during a spraying event, rather than the quantified magnitude wall shear stress at the retinal wall- after a spraying event. This study was able to hypothesise wall

shear stress magnitude at the retinal wall through the mathematical model. It is highly challenging to evaluate shear stresses imparted to the therapeutic cells experimentally, although this is a necessary validation step for future work. Introducing mathematical modelling in this thesis along with the results obtained, has shown potential for future development of cell-based therapies to treat retinal degenerative diseases, by quantifying input and output parameters and developing operating equations to develop organ-specific spraying parameter for cell-based therapies and for the design of aerosol spraying equipment.

6.3. Summary of research achievements

In summary, this work used computational modelling as a tool to explore spraying parameters for cell-laden hydrogels for retinal damage repair. This thesis was able to successfully develop spraying parameters for spraying cell-laden hydrogel in the eye using a currently available commercial clinical spraying equipment. This was achieved through mathematical predictions using the LISA model. This was the first time that such model was implemented for cell spraying prediction for an ophthalmic application.

Computational models of hydrogel spraying were successfully used to explore the impact of varying spraying parameters (pressure and volume flow rate at the injector nozzle, outer cone angle for the spray) on key outputs of high priority, namely the spatial distribution of the delivered hydrogel on the retinal wall, the surface area of the retina covered, and droplet speed.

This is the first time that a computational model of its kind has been developed and applied to explore spraying parameters for cell-laden hydrogels into the eye. Hitherto, there are several opportunities for further extension and validation, and possible implementation of such model across other clinical settings. Although, the computational models applied here have been used

extensively in a range of applications (be int clinical and non-clinical), however they had not been validated for the current application. The experimental assessment as part of this work includes assessment of the rheological properties of the hydrogel and cell viability post spraying.

In addition, based on the results of this process, there is the opportunity to fine tune the parameters and relationships used in the computational spraying model. Computational modelling therefore also promoted development of empirical equations describing parameter relationships and controlling the surface area of a diseased retina needing treatment, which could potentially be used to determine patient-specific spraying requirements with the potential of further introducing automated systems to perform cell-based treatments for glaucoma.

To date, there has not been any approach in the literature that would combine computational modelling for spraying of cell-laden hydrogels into the human eye, followed by experimental assessment using the same spraying parameters developed computationally. The approach presented here provides a first step towards the use of computational models to inform the design of spray systems to deliver cell therapies to the retina; yet requiring further experimental validation, including in animal models. This thesis therefore provides an interdisciplinary approach to both gain insight into, and inform, spraying processes for cell delivery to treat retinal-degenerative diseases currently affecting millions of people worldwide.

6.4. Limitations

Despite the named research achievements, several limitations were identified. Firstly, in reference to the applied LISA model used to define the injector nozzle, although the application of the LISA model to these hydrogels and spraying process has not been tested, the physical process that it is describes

is appropriate, and it is a logical start point for building a computational model of the spraying process. It is therefore noted that these relationships could be updated in future in line with new experimental findings.

Secondly, normal stress on cells due to high velocity impact and pressure would contribute more to cell damage Both normal and tangential components of stress will be communicated to the cell population and impact on cell outcomes. Due to the direction of spraying, both components of the stress will have an impact. As this is the first time such computational model is developed and implemented to explore spraying parameter for cell-laden hydrogel into the human eye, this research has therefore opened opportunities for further extension. As such, although computational models have been applied on various applications, it the first time for these models to be implemented on the current application.

Similarly, another limitation in reference to effects of normal and tangential acting on cells, this research was only able to quantify shear stresses following post-spraying; however, it would be ideal to also quantify these stresses during a spraying event in order to have a better understating of impact on cells, which could potential lead to cell death post-spraying and hopefully evaluate cell-death occurrence when a cell-laden hydrogel is ejected from a nozzle, during a spraying event or post-aerosolization.

6.5. Research bottlenecks

As mentioned above, several primary objectives were met in this thesis. A series of secondary objectives have been identified for future work (see Figure 6.1). For example, although it was beneficial using average human eye dimensions, simulations using a variability of human eye dimensions and geometries could have been carried out to evaluate sensitivity analyses for the observed output parameters. Secondly, measuring the outer cone angle

during each spraying event carried out experimentally, would have supported closer comparisons with implemented aerosolization theories in the computational model and alternative comparisons for surface area covered. In addition, experimental assessment on 3D printed human eye models and selected animal models, would have enabled a more realistic exploration of the impact of real geometries and environments on the spraying process.

Next, we discuss 4 specific areas which could be explored in detail in future work:

1. Measuring droplet size,
2. Spraying of cell-laden hydrogel,
3. Validation of experimental outputs,
4. Spraying parameters relationships.

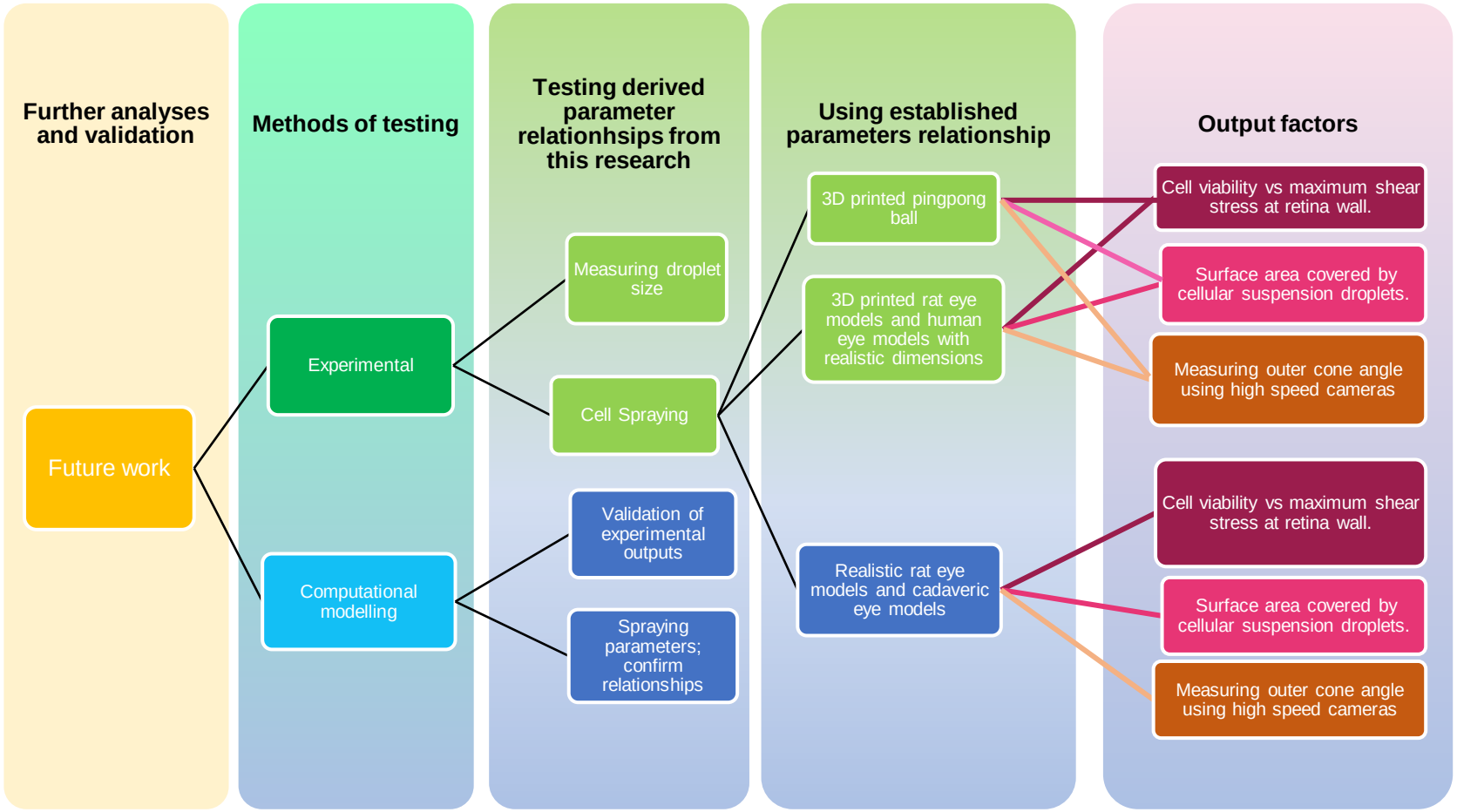

Figure 6.1Suggested future work planogram. Future studies will be conduct both mathematical modelling and experimental assessment. The experimental assessment will involve measuring droplet size of cell-laden hydrogel with a droplet sizer and measuring outer cone angle from spraying using high speed cameras. The parameters developed in this study will be implemented experimentally. Data gathered from the experimental data will be used and validated with dataset from computational modelling from this thesis. There will be an additional segment including aerosolization on 3D models of human eye and animal eyes, followed by in-vitro testing with animal models. Finally output parameters will also be evaluated. Operating relationships predicted from this thesis will be used to establish hypothesis on this future work.

6.5.1. Measuring droplets size

Following computational predictions for droplet dimensions (Section 4.8.3), further data could be obtain experimentally using droplet sizer equipment. A laser-based system will be used to measure the droplets size of the sprayed fibrin-derived hydrogel. Laser-based techniques are used for particle-size measurement in various research fields such as combustion, spray characterisation and pharmaceuticals production (135). Two important parameters from the data to be extracted are droplets size and density, both considered as critical parameters for experiments and modelling. Droplet size distribution gives important information; over the last three decades laser diffraction analysis has appeared to be effective in providing particle size distribution of observed fluids. A benefit of this technique is it requires little time to conduct the experiment and covers a wide surface area and small volume of fluid to be sprayed.

Generally, measurement methods can be carried out in situ or as external measurements. During in situ measurements, droplet dimensions can be measured at temperature and pressure of the operating conditions. This can further be distinguished into direct and indirect measurements; whereby image analysis and laser system techniques are applicable. However not all methods are able provide all these capabilities. Direct measurements include image analyses through particle video microscope, endoscope and stereomicroscope. Indirect measurement is taken through laser system, using light-back scattering or laser diffraction. Despite in-situ techniques, several researches analyse their samples using external measurements, which were one of the first methods introduced for droplet size characterisation (136). A recommended equipment meeting such technical features and that will allow droplet size measurements is the Malvern Instruments Spreytec System; a laser-based system commonly used in literature to measure droplets' size distribution for aerosol sprays and jets (137,138). This system can measure droplet sizes ranging between 0.5 and 1000 microns at rates of up to 2500 Hz.

The system works with a patent algorithm, which helps correct multi-scattering conditions taking place in high concentration sprays. The laser diffraction method measures droplets size by interpreting the angular distribution of the diffracted light by the droplets, using Fraunhofer theory, whereby the laser diffraction causes a portion of light to deflect (139). Droplets dimension are therefore determined by measuring the intensity of the laser beam travelling through the droplets.

The Malvern system operates using the Mie theory (140), whereby scattering by droplets with same size order as the wavelength takes place. Laser light-scattering detection can size liquid droplets by characterising the sprayed liquid. According to the literature (141), the technique must therefore have sufficient size-measuring resolution, broad range of sizes, provide droplet size distribution throughout the duration a spraying event and simultaneously measure droplet velocity. Measuring spray droplet size is critical to evaluate the performance on spraying technologies (142). As such there are several methods available to measure sprayed droplet size. The results can be affected by the type of measurement system, difference in sampling areas and different equipment. Depending on droplet specific velocity within a given spray, the derived data from implemented droplet sizer method can be produced spatially or temporally. Spatial data is generated when a single volume is observed over a short period of time, whereas temporal measurements observe the movement of individual droplets with different sizes. However, smaller droplet will decelerate faster compared to larger ones. Droplets breakup occurs because of mechanical forces exerted by the surrounding environment, which resist internal viscous forces. When the mechanical forces are bigger than the resisted forces, droplets deform into smaller ones. Viscous stresses due to velocity gradients in the surrounding phase act as disruptive forces during the spraying event.

As such, an accurate droplet size distribution will be measured and implemented as future work to enhance results obtained in this research.

Droplet imaging will be used as a method for further validating be computational data in Chapter 4. The cellular scaffold with properties derived in section 3.2.1 will be sprayed with cultured cells; the equipment will be set up as show in Figure 6.2 and Figure 6.3.

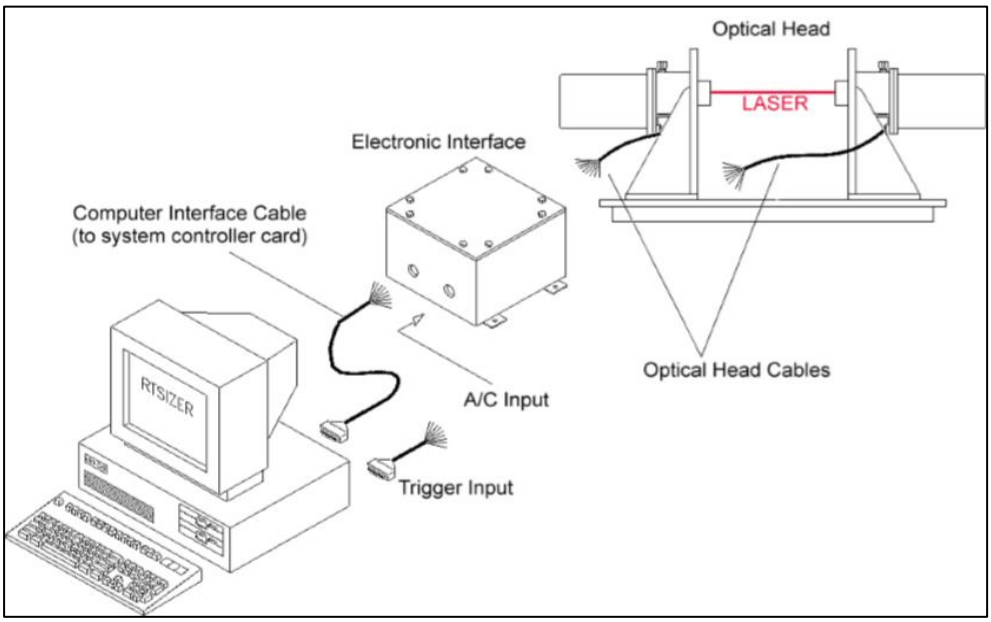

(a)

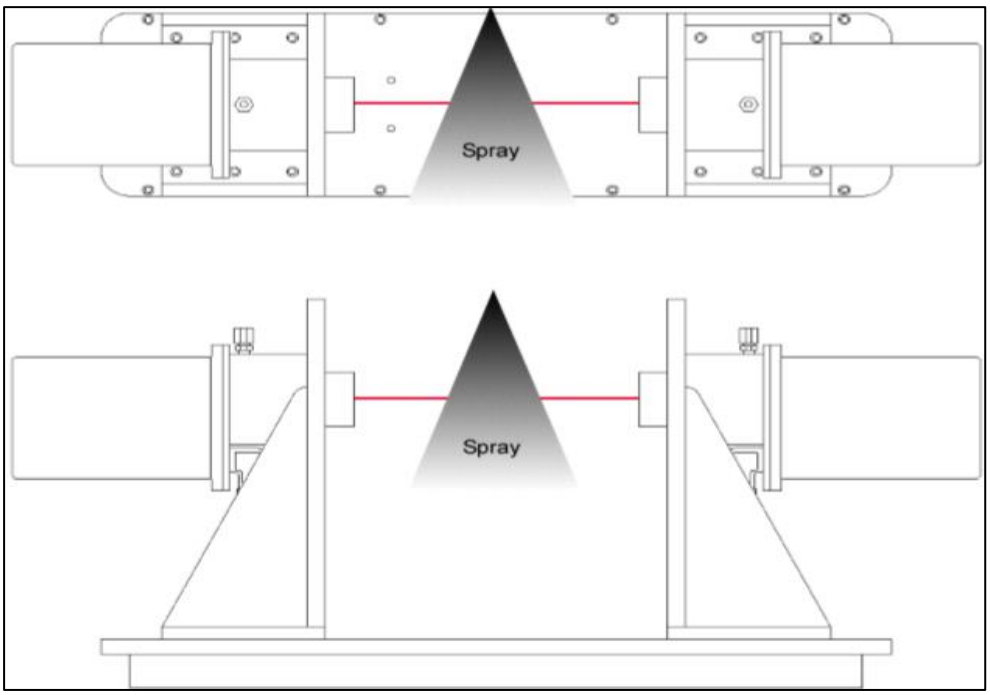

(b)

Figure 6.2 The illustrations show a 2D representation and overall set up of the Malvern Spraytec Instrument (a). The Spraytec and spray orientation (grey cone angle) are also illustrated (b). The optical head is adjusted in a controlled manner, as such that the laser measures the droplet size.

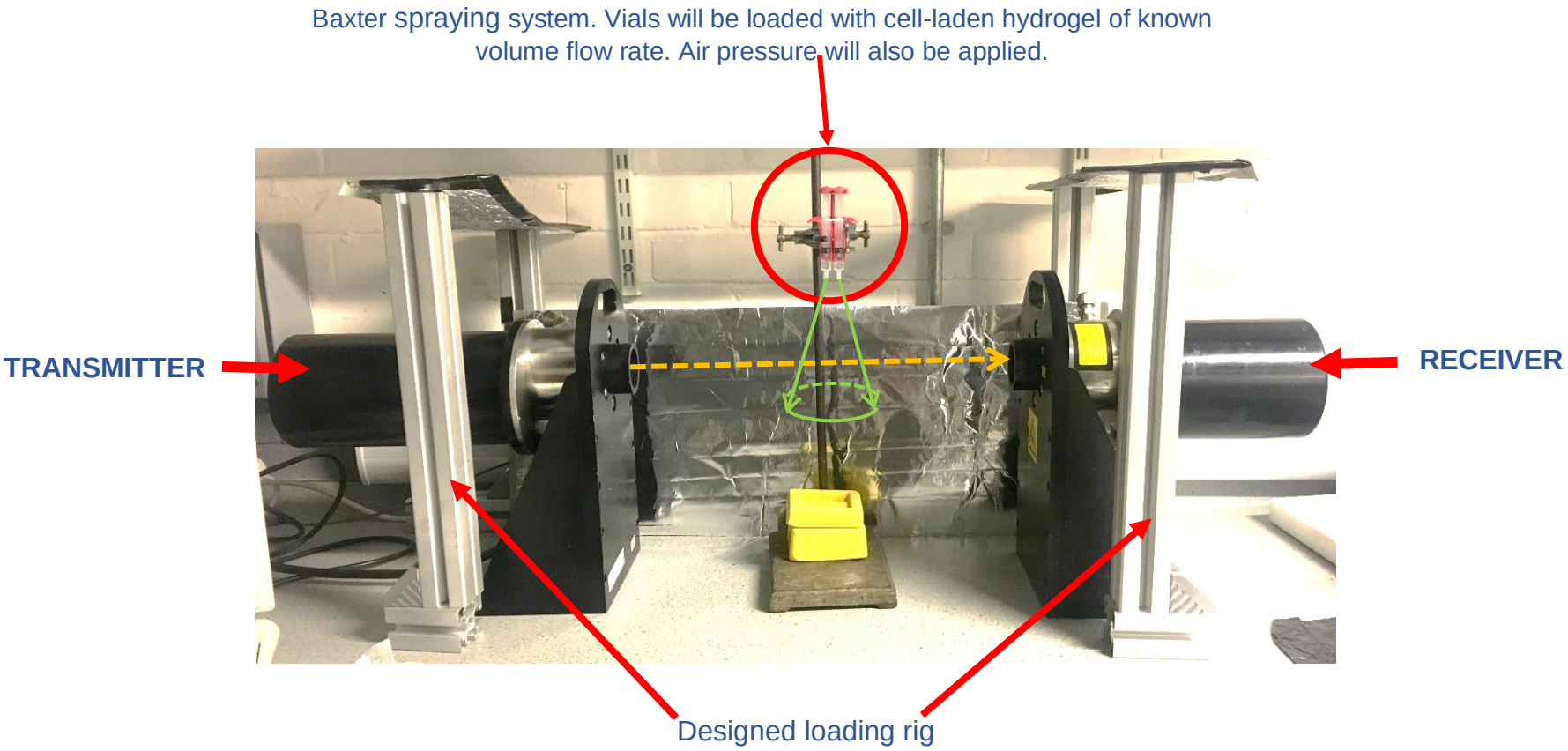

Figure 6.3 Malvern Spraytec setup, showing Baxter spraying system position on a clamp stand. The equipment will be spraying into 3D printer eye models prior to using animal eye models. This setup will be used to determine droplet dimensions and for measuring outer cone angle during each spraying event.

6.5.2. Spraying of cell-laden hydrogel on in vitro retina and 3D printed eye models

In this thesis, we have assumed the eye to be a perfect sphere with a known average diameter. Using the previously mentioned setup of the droplet sizer equipment, the proposed experimental procedure could proceed with spraying the fibrin-derived hydrogel onto 3D printed models of the human eye before proceeding with real animal eye models. Using a similar setup from Section 2.9, animal tests may be carried out on animal eye models such as rodents or pigs. This setup will help observe the behaviour of the cellular suspension once sprayed on the animal retina. Parameters relationship could then be observed through high speed cameras and validation from the developed mathematical model.

6.6. Conclusion

In conclusion, biopolymers such as fibrin-derived hydrogel offer effective sites for cell adhesion as protein-based biomaterials (116). Through cell adhesion, proliferation is set to take place onto the damaged region. The use of fibrin-derived gels has increased over the recent years due to their unique properties such as controlled degradation rate to match tissue regeneration, excellent biocompatibility and its mechanical properties which can be tuned to control ionic strength. Other properties include uniform and efficient cell distribution and its compatibility with minimal invasive delivery approaches. Literature studies support the use of fibrin-derived hydrogels to promote cell proliferation and tissue healing.

The use of fibrin gels as a cell carrier is continuously increasing, hence highlighting the need for a vehicle to facilitate cell delivery, in turn promoting cell proliferation and viability. This thesis uses fibrin-derived hydrogels protect

cells from hydrodynamic forces and other forces which may affect their survival rate post-injection, ultimately yielding good cell viability.

As research continues in this field, it should be noted that computational or mathematical modelling is yet to be employed as an alternative technique to derive organ-specific spraying parameters for prospective cell-based therapies. A number of strategies have been identified to optimise cell viability through mathematical modelling; employing a more economical process as well as a rapid technique that can be replicated for different subject and applied to different organs around the body are subject to be explored in the nearest future; notwithstanding the need to closely tuning these parameters to improve accuracy in cell delivery in a fast and controlled manner.

References

1. Forrester J., Dick AD, McMenamin PG, Roberts F, Pearlman E. Anatomy of the eye and orbit. In: The Eye: Basic Sciences in Practice. Fourth Edi. Elsevier; 2016.

2. Kaimbo D. Refractive Surgery for Myopia. In: Pacheco P, editor. Advances in Eye Surgery. InTech; 2016. p. 215–8.

3. Snell RS, Lemp MA. Development of the Eye and the Ocular Appendages. In: Clinical Anatomy of the Eye. 2nd ed. Oxford: Blackwell Science Ltd; 1998.

4. Dahlmann-noor A, Vijay S, G HJ, Limb A, Khaw PT. Current approaches and future prospects for stem cell rescue and regeneration of the retina and optic nerve. Can J Ophthalmol [Internet]. 2010;45(4):333–41. Available from: http://dx.doi.org/10.3129/i10-077

5. Jayaram H, Becker S, Eastlake K, Jones MF, Charteris DG, Limb GA. Optimized feline vitrectomy technique for therapeutic stem cell delivery to the inner retina. Vet Ophthalmol [Internet]. 2014;17(4):300–4. Available from: http://www.ncbi.nlm.nih.gov/pubmed/24661435

6. Lawrence JM, Singhal S, Bhatia B, Keegan DJ, Reh TA, Luthert PJ, et al. MIO-M1 Cells and Similar Müller Glial Cell Lines Derived from Adult Human Retina Exhibit Neural Stem Cell Characteristics. Stem Cells [Internet]. 2007;25(8):2033–43. Available from: http://doi.wiley.com/10.1634/stemcells.2006-0724

7. Koeppen B., Stanton BA. Section II: The Nervous System. In: Berne & Levy Physiology. Sixth Edit. Philadelphia: Elsevier; 2009. p. 126.

8. Macdonald RB, Randlett O, Oswald J, Yoshimatsu T, Franze K, Harris WA. Müller glia provide essential tensile strength to the developing retina. 2015;210(7).

9. Curcio A., Allen K. Topography of ganglion cells in human retina. J Comp Neurol. 1990;300:5–25.

10. Kiel J., Hollingsworth M, Rao R, Chen M, Reitsamer HA. Ciliary Blood Flow and Aqueous Humour Production. Natl Inst Heal Prog Retin Eye Res. 2011;30(1):1–17.

11. WHO. Chronic Diseases and Health Promotion [Internet]. World Health Organisation. 2017 [cited 2017 Oct 10]. Available from: http://www.who.int/chp/en/

12. Hamon A, Roger JE, Yang XJ, Perron M. Müller glial cell-dependent regeneration of the neural retina: An overview across vertebrate model systems. Dev Dyn. 2016;245(7):727–38.

13. Pezzullo L, Streatfeild J, Simkiss P, Shickle D. The economic impact of sight loss and blindness in the UK adult population. BMC Health Serv Res. 2018;18(1):1–13.

14. Johnson T V., Bull ND, Martin KR. Stem cell therapy for glaucoma: Possibilities and practicalities. Expert Rev Ophthalmol. 2011;6(2):165–74.

15. Daliri K, Ljubimov AV, Hekmatimoghaddam S. Glaucoma, stem cells, and gene therapy: Where are we now? Int J Stem Cells. 2017;10(2):119–28.

16. Viswanathan A, Spera C, Mullins A, Covert D, Banhazi J, McDwyer P, et al. Resource Utilization Among Glaucoma Patients in the UK Treated with Beta-Blocker and Non-Beta-Blocker Adjunctive Therapy: A Retrospective Cohort Analysis. Adv Ther. 2017;34(7):1695–706.

17. Velde S Van De, Groef L De, Stalmans I, Moons L, Hove I Van. Progress in Neurobiology Towards axonal regeneration and neuroprotection in glaucoma : Rho kinase inhibitors as promising therapeutics. Prog Neurobiol [Internet]. 2015;131:105–19. Available from: http://dx.doi.org/10.1016/j.pneurobio.2015.06.002

18. MoorfieldEyeHospital. Glaucoma [Internet]. 2017 [cited 2017 Sep 4]. Available from: http://www.moorfields.nhs.uk/condition/glaucoma

19. Chang E., Goldberg J. Glaucoma 2.0: Neuroprotection, Neuroregeneration, Neuroenhancement. Ophthalmology. 2012;119(5):979–86.

20. Maclaren RE, Pearson RA, Macneil A, Douglas RH, Salt TE, Akimoto M, et al. Retinal repair by transplantation of photoreceptor precursors. Nature. 2006;444(November):203–7.

21. Lasagni L, Sagrinati C, Ronconi E, Angelotti ML, Parente E, Ballerini L, et al. Novel strategies of regenerative medicine using chemical compounds. Curr Med Chem. 2010;17(34):4134–49.

22. Kwon YH, Fingert JH, Kuehn MH, Alward WL. Primary open-angle glaucoma. N Engl J Med. 2009;360(11):1113–24.

23. Leske MC, Wu SY, Hennis A, Honkanen R, Nemesure B. Risk Factors for Incident Open-angle Glaucoma. The Barbados Eye Studies. Ophthalmology. 2008;115(1):85–93.

24. Salim S, Shields MB. Glaucoma and Systemic Diseases. Surv Ophthalmol [Internet]. 2010;55(1):64–77. Available from: http://dx.doi.org/10.1016/j.survophthal.2009.03.006

25. Danesh-Meyer H V., Levin LA. Glaucoma as a neurodegenerative disease. J Neuro-Ophthalmology. 2015;35:S22–8.

26. Gupta D. Risk Factor for Glaucoma. In: Glaucoma Diagnosis and Manageement. Lippincott Williams & Wilkins; 2005. p. 5–7.

27. He Z, Vingrys AJ, Armitage JA, Bui B V. The role of blood pressure in glaucoma. Clin Exp Optom. 2011;94(2):133–49.

28. Lund RD, Kwan ASL, Keegan DJ, Sauvé Y, Coffey PJ, Lawrence JM. Cell transplantation as a treatment for retinal disease. Vol. 20, Progress in Retinal and Eye Research. 2001. 415–449 p.

29. Sun Y, Williams A, Waisbourd M, Iacovitti L, Katz LJ. Stem cell therapy for glaucoma: Science or snake oil? Surv Ophthalmol. 2015;60(2):93–105.

30. Meyer J., Katz M., Marunia JA, Kirk M. Embryonic Stem Cell-Derived Neural Progenitors Incorporate into Degenerating Retina and Enhance Survival of Host Photoreceptors. Stem Cells. 2006;24(2):274–83.

31. Hambright D, Park KY, Brooks M, McKay R, Swaroop A, Nasonkin IO. Long-term survival and differentiation of retinal neurons derived from human

embryonic stem cell lines in un-immunosuppressed mouse retina. Mol Vis. 2012;18(July 2011):920–36.

32. Kirsner RS, Marston WA, Snyder RJ, Lee TD, Cargill DI, Slade HB. Spray-applied cell therapy with human allogeneic fi broblasts and keratinocytes for the treatment of chronic venous leg ulcers: A phase 2, multicentre, double-blind, randomised, placebo-controlled trial. Lancet [Internet]. 2012;380(9846):977–85. Available from: http://www.embase.com/search/results?subaction=viewrecord&from=export&id=L52144973%5Cnhttp://dx.doi.org/10.1016/S0140-6736(12)60644-8

33. Chen M, Chen Q, Sun X, Shen W, Liu B, Zhong X, et al. Generation of retinal ganglion-like cells from reprogrammed mouse fibroblasts. Investig Ophthalmol Vis Sci. 2010;51(11):5970–8.

34. Dimos JT, Rodolfa KT, Niakan KK, Weisenthal LM, Mitsumoto H, Chung W, et al. Induced pluripotent stem cells generated from patients with ALS can be differentiated into motor neurons. Science (80-). 2008;321(5893):1218–21.

35. Das A V., Mallya KB, Zhao X, Ahmad F, Bhattacharya S, Thoreson WB, et al. Neural stem cell properties of Müller glia in the mammalian retina: Regulation by Notch and Wnt signaling. Dev Biol. 2006;299(1):283–302.

36. Limb G., Salt T., Munro PM., Moss S., Khaw P. In vitro characterization of a spontaneously immortalized human Muller cell line (MIO-M1). Invest Ophthalmol Vis Sci. 2002;43(3):864–9.

37. Johnson T V., Bull ND, Hunt DP, Marina N, Tomarev SI, Martin KR. Neuroprotective effects of intravitreal mesenchymal stem cell transplantation in experimental glaucoma. Investig Ophthalmol Vis Sci. 2010;51(4):2051–9.

38. Arnhold S, Absenger Y, Klein H, Addicks K, Schraermeyer U. Transplantation of bone marrow-derived mesenchymal stem cells rescue photoreceptor cells in the dystrophic retina of the rhodopsin knockout mouse. Graefe's Arch Clin Exp Ophthalmol. 2007;245(3):414–22.

39. Bibel M, Richter J, Schrenk K, Tucker K., Staiger V, Korte M, et al. Differentiation of Mouse Embryonic Stem Cells into a Defined Neuronal Lineage. Nat Neurosci. 2004;7:1003–9.

40. Hira1. Hirano M, Yamamoto A, Yoshimura N, Tokunaga T, Motohashi T, Ishizaki K, et al. Generation of Structures Formed by Lens and Retinal Cells Differentiating from Embryonic Stem Cells. Dev Dyn. 2003;228:664–71. no M, Yamamoto A, Yoshimura N, Tokunaga T, Motohashi T, Ishizaki K, et al. Generation of Structures Formed by Lens and Retinal Cells Differentiating from Embryonic Stem Cells. Dev Dyn. 2003;228:664–71.

41. Wright L., Phillips M., Hei D, D.M G. Induced Pluripotent Stem Cells as Custom Therapeutics for Retinal Repair: Progress and Rationale. Exp Eye Res. 2014;123:167–72.

42. Lamba DA, Karl MO, Ware CB, Reh TA. Efficient generation of retinal progenitor cells from human embryonic stem cells. 2006;103(34).

43. Pearson RA, Barber AC, Rizzi M, Hippert C, Xue T, West EL, et al. Restoration of Vision After Transplantation of Photoreceptors. 2014;485(7396):99–103.

44. Hentze H, Graichen R, Colman A. Cell therapy and the safety of embryonic

stem cell-derived grafts. Trends Biotechnol. 2007;25(1):24–32.

45. Chen C, Ouyang W, Grigura V, Zhou Q, Carnes K, Lim H, et al. ERM is required for Transplantation Control of the Spermatogonial Stem Cell Niche. Nature. 2005;436(7053):1030–4.

46. Inoue Y, Iriyama A, Ueno S, Takahashi H, Kondo M, Tamaki Y. Subretinal Transplantation of Bone Marrow Mesenchymal Stem Cells Delays Retinal Degeneration in the RCS Rat Model of Retinal Degeneration. Exp Eye Res. 2007;85(2):234–41.

47. Johnson T., DeKorver N., Levasseur V., Osbourne A, Tassoni A, Lorber B, et al. Identification of Retinal Ganglion Cell Neuroprotection Conferred by Platelet-Derived Growth Factor through Analysis of Mesenchymal Stem Cell Secretome. Brain. 2014;137:503–19.

48. Joe AW, Gregory-Evans K. Mesenchymal stem cells and potential applications in treating ocular disease. Curr Eye Res. 2010;35(11):941–52.

49. Jayaram H, Khaw PT, Maclaren RE, Limb GA. Focus on Molecules: Neural Retina Leucine Zipper (NRL). Exp Eye Res. 2012;104:99–100.

50. Tibbetts MD, Samuel MA, Chang TS, Ho AC. Stem cell therapy for retinal disease. Curr Opin Ophthalmol. 2012;23(3):226–34.

51. Okita K, Yamakawa T, Matsumura Y, Sao Y, Amano N, Watanabe A. Embryonic Stem Cells, Induced Pluripotent Stem Cells: An Efficient Nonviral Method to Generate Integration-Free Human- Induced Pluripotent Stem Cells from Cord Blood and Peripheral blood Cells. Stem Cells. 2013;31:458–66.

52. Bhutani K, Nazor KL, Williams R, Tran H, Dai H, Dzakula Z, et al. Whole-genome mutational burden analysis of three pluripotency induction methods. Nat Commun. 2016;7:1–8.

53. Yan H, Shi YB, Huang J. iPSCs are safe! Cell Biosci. 2017;7(1):1–2.

54. Winkler B., Arnold MJ, Brassell M., Puro DG. Energy Metabolism in Human Retinal Müller Cells. Invest Ophthalmol Vis Sci. 2000;41(10):735–45.

55. Poitry-Yamate CL, Poitry S, Tsacopoulos M. Lactate released by Müller glial cells is metabolized by photoreceptors from mammalian retina. J Neurosci [Internet]. 1995;15(7 Pt 2):5179–91. Available from: http://www.ncbi.nlm.nih.gov/pubmed/7623144

56. Kofuji P, Biedermann B, Siddharthan V, Raap M, Iandiev I, Milenkovic I, et al. Kir potassium channel subunit expression in retinal glial cells: Implications for spatial potassium buffering. Glia. 2002;39(3):292–303.

57. Newman E, Reichenbach A. The Muller cell: A functional element of the retina. Trends Neurosci. 1996;19(8):307–12.

58. Bringmann A, Pannicke T, Grosche J, Francke M, Wiedemann P, Skatchkov SN, et al. Müller cells in the healthy and diseased retina. Prog Retin Eye Res. 2006;25(4):397–424.

59. Paulson OB, Newman EA. Does the release of potassium from astrocyte endfeet regulate cerebral blood flow? Science (80-). 1987;237(4817):896–8.

60. Tout et al. The role of Müller cells in the formation of the blood-retina1 barrier. J Neurosci. 1993;55(1):291–301.

61. Lu Y, Kirchhoff F, Wolburg H, Franze K, Seifert G, Steinha C, et al. Viscoelastic properties of individual glial cells and neurons in the CNS. 2006;103(47):17759–64.

62. Raymond PA, Barthel LK, Bernardos RL, Perkowski JJ. Molecular characterization of retinal stem cells and their niches in adult zebrafish. 2006;17:1–17.

63. Singhal S, Bhatia B, Jayaram H, Becker S, Jones MF, Cottrill PB, et al. Human Muller Glia with Stem Cell Characteristics Differentiate into Retinal Ganglion Cell (RGC) Precursors In Vitro and Partially Restore RGC Function In Vivo Following Transplantation. Stem Cells Transl Med. 2012;1(3):188–99.

64. Limb G., Jones M., Eastlake K, Becker S. Biomaterials for Repair and Regeneration of the neural retina. In: Chirila T, Harkin D, editors. Biomaterials and Regenerative Medicine in Ophthalmology [Internet]. 2nd ed. London: Elsevier Science; 2016. p. 243–60. (Woodhead Publishing Series in Biomaterials). Available from: https://books.google.co.uk/books?id=rdmoBAAAQBAJ

65. Lefebvre AH, McDonell VG. Atomization and Sprays. Second Edi. Chigier N, editor. Boca Raton: Taylor & Francis Group; 2017. 1–13 p.

66. Roberts A, Wyslouzil BE, Bonassar L. Aerosol delivery of mammalian cells for tissue engineering. Biotechnol Bioeng. 2005;91(7):801–7.

67. Thiebes AL, Albers S, Klopsch C, Jockenhoevel S, Cornelissen CG. Spraying Respiratory Epithelial Cells to Coat Tissue-Engineered Constructs. 2015;4:278–87.

68. Janmey PA, Winer JP, Weisel JW. Fibrin gels and their clinical and bioengineering applications. J R Soc Interface [Internet]. 2009;6(30):1–10. Available from: http://www.pubmedcentral.nih.gov/articlerender.fcgi?artid=2575398&tool=pmcentrez&rendertype=abstract

69. Jaffe G., Ashton P, Pearson P. Intravitreal Antimicrobials. In: Intraocular Drug Delivery [Internet]. New York: Taylor & Francis; 2006. p. 89. Available from: https://books.google.co.uk/books?id=C-k1wNP6nMgC&pg=PA89&dq=vitreous+volume+human+eye&hl=en&sa=X#v=onepage&q=vitreous volume human eye&f=false

70. Chaurasia SS, Champakalakshmi R, Angunawela RI, Tan DT, Mehta JS. Optimization of Fibrin Glue Spray Systems for Ophthalmic Surgery. Transl Vis Sci Technol. 2012;1(2):2.

71. Singh K, Moyer H, Williams JK, Schwartz Z. Fibrin Glue. 2011;66(3).

72. Rajendra AU, Eddie Ng YK, Jasjit SS. The Human Eye. In: Image Modeling of the Human Eye. Boston: Artech House;

73. Chen F-M, Liu X, Polym P, Author S. Advancing biomaterials of human origin for tissue engineering HHS Public Access Author manuscript. Prog Polym Sci [Internet]. 2016;53:86–168. Available from: https://www.ncbi.nlm.nih.gov/pmc/articles/PMC4808059/pdf/nihms680686.pdf

74. Annabi N, Yue K, Tamayol A, Khademhosseini A. Elastic sealants for surgical applications. Eur J Pharm Biopharm. 2015;96:27–39.

75. Chan BP, Leong KW. Scaffolding in tissue engineering: General approaches

and tissue-specific considerations. Eur Spine J. 2008;17(SUPPL. 4).

76. Dzobo K, Thomford NE, Senthebane DA, Shipanga H, Rowe A, Dandara C, et al. Advances in regenerative medicine and tissue engineering: Innovation and transformation of medicine. Stem Cells Int. 2018;2018.

77. Kundu J, Michaelson A, Baranov P, Young MJ, Carrier L. Approaches to Cell Delivery : Substrates and Scaffolds for Cell Therapy. 2014;53:143–54.

78. Bahoric A, Harrop AR, Clarke HM, Zuker RM. Aerosol vehicle for delivery of epidermal cells – An in vitro study. 1997;5(3):153–6.

79. Bahoric A, Aitken K, Smith CR, Khoury AE. Reconstruction Aerosol Transfer of Bladder Urothelial and Smooth Muscle Cells onto Demucosalized Colonic Segments for Porcine Bladder Augmentation In Vivo: a 6 Week Experimental Study. 2005;174(October):1663–8.

80. Marx G. Evolution of fibrin glue applicators. Transfus Med Rev [Internet]. 2003;17(4):287–98. Available from: http://www.sciencedirect.com/science/article/pii/S0887796303000415

81. Yoon SS, Heister SD. Categorizing linear theories for atomizing round jets. At Sprays. 2003;13:499–516.

82. Johnson HG, Yonkers NY. Method of and Apparatus for Effecting Medicinal Treatment. US2112160, 1938. p. 1–7.

83. Redl H, Kriwetz G. Apparatus for Applying a Tissue Adhesive on the Basis of Human or Animal Proteins. US4359049, 1982. p. 23–6.

84. Eibl J, Seelich T, Redl H, Habison G. Arrangement for Applying a Tissue Adhesive. US4735616, 1988. p. 2–6.

85. Pizzino JL. Dual Syringe for Either Simultaneous or Sequential Injection of Liquids. US4609371, 1986.

86. Redl H, Habison G. Apparatud for Applying a Tissue Adhesive. US4631055, 1986.

87. Miller CH, Kaufman Arenberg I, Altshuler JH. Fibrin Glue Delivery System. US4874368, 1989.

88. Zimmermann J. Spray Head for the Administration of a Multi-Component Material by Meaans of Gas. US4925108, 1990.

89. Capozzi EE, Cookston SH. Biological Syringe System. 1990.

90. Wolf SJ, Mart RK. Two Component Syringe Delivery System. US4979942, 1990.

91. Holm NE. Dispensing Device For Dispensing at Least Two Fluids. US5376079, 1994.

92. Avoy DR. Fibrinogen Dispensing Kit. US4902281, 1990.

93. Collins R, van der Werff T. Introduction. In: Mathematical Models of the Dynamis of the Human Eye. 2013. p. 1–3.

94. Edwards TL, Xue K, Meenink HCM, Beelen MJ, Naus GJL. First-in-human study of the safety and viability of intraocular robotic surgery. Nat Biomed Eng. 2018;2:649–56.

95. BaxterHealthcare. TISSEEL Lyo Two-Component Fibrin Sealant [Internet]. EMC. 2015. Available from: https://www.medicines.org.uk/emc/medicine/30148

96. Baxter. DUPLOTIP Applicators [Internet]. Baxter Healthcare Corporation. 2017. Available from: http://www.tisseel.com/us/devices_duplotip.html

97. Rahimy E, Wilson J, Tsao T, Schwartz S. Robot-assisted intraocular surgery : development of the IRISS and feasibility studies in an animal model. Eye [Internet]. 2013;27(8):972–8. Available from: http://dx.doi.org/10.1038/eye.2013.105

98. Üneri A, Balicki MA, Handa J, Gehlbach P, Taylor RH. New Steady-Hand Eye Robot with Micro-Force Sensing for Vitreoretinal Surgery. Natl Inst Heal. 2011;814–9.

99. Jensen PS, Grace KW, Attariwala R, Glucksberg MR. Toward robot-assisted vascular microsurgery in the retina. 1997;696–701.

100. Knobbe CA. Vitrectomy and Vitroretinal Eye Surgery [Internet]. All About Vision. 2016 [cited 2017 Feb 17]. Available from: http://www.allaboutvision.com/conditions/vitreoretinal-procedures.htm

101. 123rf. Eye Anatomy [Internet]. [cited 2016 Nov 4]. Available from: http://www.123rf.com/photo_19902297_anatomy-of-eye.html

102. Gross H, Blechinger F, Achnter B. Human Eye. In: Gross H, editor. Handbook of Optical Systems [Internet]. Wiley-Vch; 2008. p. 3–20. Available from: https://application.wiley-vch.de/books/sample/3527403809_c01.pdf

103. Bekerman I, Gottlieb P, Vaiman M. Variations in Eyeball Diameters of the Healthy Adults. J Ophthalmol [Internet]. 2014;2014:1–5. Available from: http://dx.doi.org/10.1155/2014/503645

104. Baptist I. Modeling Multiphase Flow. In: STAR CCM+ User Guide: Version 906. 2014.

105. Schmidt D, Nouar I, Senecal P, Rutland C., Martin J, Reitz RD. Pressure-Swirl Atomization in the Near Field Pressure-Swirl Atomization in the Near Field. SAE Teh Pap Ser. 1999;1:1–14.

106. Rosiak JM, Yoshii F. Hydrogels and their medical applications. Nucl Instruments Methods Phys Res Sect B Beam Interact with Mater Atoms. 1999;151(1–4):56–64.

107. Bowman J. Tissie Adesives for Growth Factor Drug Delviery. In: Lee DL, editor. Biomaterials and Bioengineering Handbook. New York: Taylor and Francis Group; 2000. p. 261–88.

108. Allan B. Closer to nature : new biomaterials and tissue engineering in ophthalmology Closer to nature : new biomaterials and tissue engineering in ophthalmology. Br J Ophthalmol. 1999;(February 2007):1235–40.

109. Tomita M, Lavik E, Klassen H, Zahir T, Langer R, Young M. O riginal A rticle and Differentiation of Retinal Progenitor Cells. Stem Cells. 2005;23(10):1579–88.

110. Duan X, McLaughlin C, Griffith M, Sheardown H. Biofunctionalization of collagen for improved biological response: Scaffolds for corneal tissue engineering. Biomaterials. 2007;28(1):78–88.

111. Engler AJ, Sen S, Sweeney HL, Discher DE. Matrix Elasticity Directs Stem Cell Lineage Specification. Cell. 2006;126(4):677–89.

112. Guvendiren M, D.Lu H, Burdick J. Shear-thinning hydrogels for biomedical applications. R Soc Chem. 2012;8:260–72.

113. Radosevich M, Goubran HI, Burnouf T. Fibrin sealant: scientific rationale, production methods, properties, and current clinical use. Vox Sang. 1997;72:133–43.

114. Sierra DH. Fibrin Sealant Adhesive Systems: A Review of Their Chemistry, Material Properties and Clinical Applications. J Biomater Appl [Internet]. 1993;7(4):309–52. Available from: http://jba.sagepub.com/content/7/4/309.abstract

115. Panda A, Kumar S, Kumar A, Bansal R, Bhartiya S. Fibrin glue in ophthalmology. 2015;57(5):371–9.

116. Li Y, Meng H, Liu Y, Lee BP. Fibrin Gel as an Injectable Biodegradable Scaffold and Cell Carrier for Tissue Engineering. 2015;2015.

117. Balakrishnan B, Jayakrishnan A. Injectable Hydrogels for Biomedical Applications. In: Nair L., editor. Injectable Hydrogels for Regenerative Engineering. Imperial College Press; 2016. p. 68–75.

118. Morris PD, Narracott A, Von Tengg-Kobligk H, Soto DAS, Hsiao S, Lungu A, et al. Computational fluid dynamics modelling in cardiovascular medicine. Heart. 2016;102(1):18–28.

119. Freed LE, Guilak F, Guo XE, Gray ML, Tranquillo R, Holmes JW, et al. Advanced tools for tissue engineering: Scaffolds, bioreactors, and signaling. Tissue Eng. 2006;12(12):3285–305.

120. Akalp U, Bryant SJ, Vernerey FJ, Engineering B. Sensitive Hydrogels : a Mathematical Model. 2017;12(36):7505–20.

121. Lemon G, King JR, Byrne HM, Jensen OE, Shakesheff KM. Digital Object Identifier Mathematical Biology Mathematical modelling of engineered tissue growth using a multiphase porous flow mixture theory. J Math Biol [Internet]. 2006;52:571–94. Available from: https://link.springer.com/content/pdf/10.1007%2Fs00285-005-0363-1.pdf

122. Whittaker RJ, Booth R, Dyson R, Bailey C, Parsons Chini L, Naire S, et al. Mathematical modelling of fibre-enhanced perfusion inside a tissue-engineering bioreactor. J Theor Biol. 2009;256(4):533–46.

123. Zhang Z, Chen Q. Comparison of the Eulerian and Lagrangian methods for predicting particle transport in enclosed spaces. Atmos Environ. 2007;41(25):5236–48.

124. Peric M, Ferguson S. The Advantage of Polyhedral Mesh [Internet]. CD-adapco. Available from: http://www.plmmarketplace.com/upload/Temp/The_Advantage_of_polyhedral_1.pdf

125. Beirao da Veiga L, Lipnikov K, Manzini G. Model Eliptic Problems. In: The mimetic Finite Difference Method for Elliptic Problems: Modeling, Simulation and applications. Springer Internstional Publishing; 2014. p. 3–5.

126. Geijssen HC. Studies on Normal Pressure Glaucoma [Internet]. Kugler

Publications; 1991. Available from: https://books.google.co.uk/books?id=5xerl6ZdY6IC

127. Dijkstra K, Hendriks J, Karperien M, Vonk LA, Saris DBF. Arthroscopic Airbrush-Assisted Cell Spraying for Cartilage Repair: Design, Development, and Characterization of Custom-Made Arthroscopic Spray Nozzles. Tissue Eng - Part C Methods [Internet]. 2017;23(9):505–15. Available from: https://www.scopus.com/inward/record.uri?eid=2-s2.0-85029149684&doi=10.1089%2Ften.tec.2017.0228&partnerID=40&md5=992eb5a841a60a59bd89c1dd81b3c24d

128. Flammer J, Orgül S. Optic nerve blood-flow abnormalities in glaucoma. Prog Retin Eye Res [Internet]. 1998;17(2):267–89. Available from: http://www.ncbi.nlm.nih.gov/pubmed/9695795

129. Han Z, Parrish S, Farrell P., Reitz R. Modeling atomization.pdf. At Sprays. 1997;7:663–84.

130. Malek AM, Izumo S, Alevriadou BR, Eskin SG, McIntire S V., Schilling WP, et al. Mechanism of endothelial cell shape change and cytoskeletal remodeling in response to fluid shear stress. J Cell Sci [Internet]. 1996;726(4):713–26. Available from: http://www.ncbi.nlm.nih.gov/pubmed/8718663

131. Abu-Reesh I, Kargi F. Biological responses of hybridoma cells to defined hydrodynamic shear stress. J Biotechnol [Internet]. 1989;9(3):167–78. Available from: http://www.sciencedirect.com/science/article/pii/0168165689901065

132. Jenkins MM, Farid, Suzanne S. Human pluripotent stem cell-derived products: advances towards robust, scalable and cost-effective manufacturing strategies. Biotochnology J. 2015;10:83–95.

133. Yamamoto K. Fluid shear stress induces differentiation of Flk-1-positive embryonic stem cells into vascular endothelial cells in vitro. AJP Hear Circ Physiol [Internet]. 2004;288(4):H1915–24. Available from: http://ajpheart.physiology.org/cgi/doi/10.1152/ajpheart.00956.2004

134. Duncan CO, Shelton RM, Navsaria H, Balderson DS, Papini RPG, Barralet JE. In vitro transfer of keratinocytes: Comparison of transfer from fibrin membrane and delivery by aerosol spray. J Biomed Mater Res - Part B Appl Biomater. 2005;73(2):221–8.

135. Black DL, McQuay MQ, Bonin MP. Laser-based techniques for particle-size measurement: A review of sizing methods and their industrial applications. Prog Energy Combust Sci. 1996;22(3):267–306.

136. Dodge LG, Rhodes DJ, Reitz RD. Drop-size measurement techniques for sprays : comparison of Malvern laser-diffraction and Aerometrics phase / Doppler.

137. Malvern Instruments. Spraytec Installation Manual. 1999.

138. Izzudin M, Zainal I, Aziz A, Raman A, Iskandr M, Nor M. Review on Measurement Techniques for Drop Size Distribution in a Stirred Vessel. Ind Eng Chem. 2013;52(October):16085–16084.

139. Fritsch. Particle sizing: the Fraunhoffer theory [Internet]. Fritsch International. 2019 [cited 2019 Jan 15]. Available from: https://www.fritsch-international.com/particle-sizing/fritsch-knowledge/fraunhofer-theory/

140. Saidi IS, Jacques SL, Tittel FK. Mie and Rayleigh modeling of visible-light scattering in neonatal skin. Appl Opt. 1995;34(31):7410–8.

141. Bachalo WD. Methos for measuring the size and velocity of spheres by dual-beam light scatter interferometry. Appl Opt. 1980;19(3):363–70.

142. Fritz BK, Hoffmann W., Bagley W., Kruger G., Czaczyk Z, Henry R. measurement distance and airspeed effects MEASURING DROPLET SIZE OF AGRICULTURAL SPRAY NOZZLES — MEASUREMENT DISTANCE AND AIRSPEED EFFECTS. At Sprays. 2014;24(9):747–60.

143. Miller CH, McLevish B. FLuid Separation Control Attachment for Physiological Glue Applicator. Micromedics, Inc.,; US5474540, 1995.